Investigating the Effect of Tow-Drop Gaps in AFP Produced Laminates

A Theoretical and Numerical Study

Master's Thesis

Athanasios Giotas

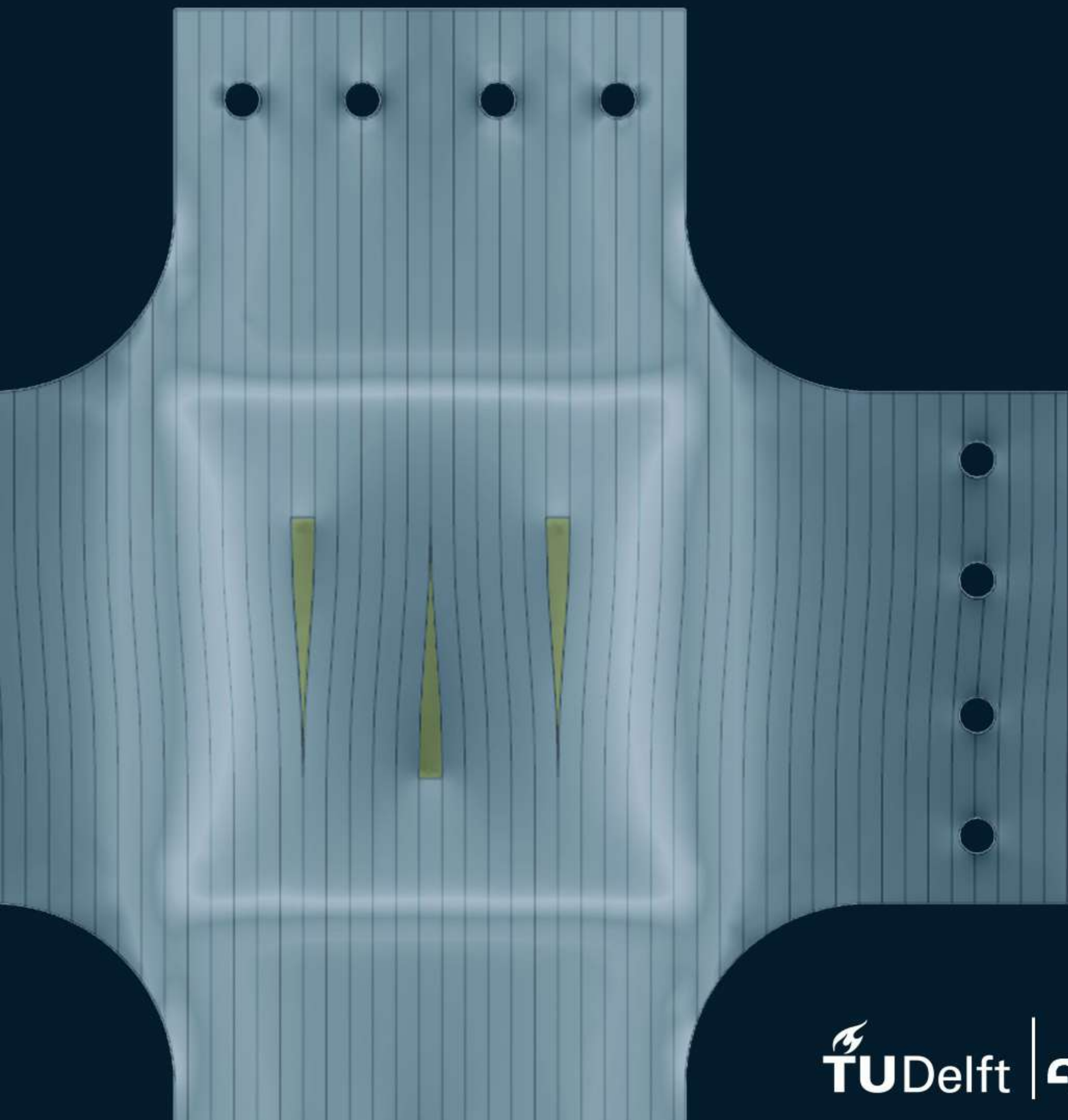

Investigating the Effect of Tow-Drop Gaps in AFP Produced Laminates

A Theoretical and Numerical Study

by

Athanasios Giotas

Supervisors:	Dr. Daniël M.J. Peeters
	Dr.-Ing. Saullo G.P. Castro
	Jaap Dekker (on behalf of Airborne Aerospace)
Project Duration:	May, 2024 - January 2025
Faculty:	Faculty of Aerospace Engineering, TU Delft

Abstract

This thesis investigates the effects of tow-drop gaps, a common defect in composite laminates manufactured using Automated Fiber Placement (AFP), on the tensile strength and failure behaviour of composite materials. Tow-drop gaps occur when a tow in a composite ply is terminated upon encountering the boundary of an adjacent tow oriented in a different direction. The thesis was carried out in close collaboration with Airborne Aerospace, a company specializing in manufacturing composite structures for aerospace applications with a specific interest in this topic. The study focuses on accurately modelling these manufacturing defects, incorporating post-curing deformations such as fiber waviness and resin pockets, and understanding their implications for practical applications like pressure vessels.

To achieve this, three specimen designs were developed and analyzed using Finite Element Modelling (FEM). These models were used to assess tensile strength reductions and failure behaviours by comparing baseline specimens to those containing tow-drop gaps. Initial results showed strength reductions of 16–21.6% across the three designs. However, updated results incorporating the (assumed) post-cured laminate geometry revealed even greater strength reductions, though the exact increase is hard to be accurately estimated. Predictions about failure based on the Hashin failure criterion highlighted mainly a tensile matrix failure mode, with assumed failure mechanisms involving predominantly matrix cracking, delaminations and fiber fracture.

The findings emphasize the critical impact of tow-drop gaps on composite performance, highlighting the necessity of incorporating defect-induced behaviours in design and analysis processes. Recommendations for future research include validating results through physical testing, refining FE models and possibly expanding the research to analyze overlaps as well, in order to obtain a clearer view about the effect of AFP-induced manufacturing defects.

Acknowledgements

This thesis marks the culmination of a significant phase in my academic (and personal) journey, and it would not have been possible without the guidance, support, and encouragement of many people. I take this opportunity to express my deepest gratitude to all those who have made this journey a bit easier.

First and foremost, I would like to express my sincere appreciation to my supervisors: Dr. ir. Daniël Peeters and Dr.-Ing. Saullo Castro (from TU Delft) and Jaap Dekker from Airborne Aerospace. Their guidance and feedback throughout the whole period of this research proved to be valuable, and I deeply appreciate the time they dedicated to our weekly discussions despite their busy schedules.

I would also like to thank all the employees of Airborne Aerospace that I spent time with, for creating a very welcoming, friendly and supporting environment in the office.

Finally, above all, I want to express my gratitude towards my parents Kostas and Evi, my sister Maria, as well as my girlfriend Agathi, who supported me in any way they could along the whole duration of this project, and whose encouragement, patience and understanding helped me push through every challenge along the way.

Contents

List of Figures

List of Tables

1
Introduction

As is probably already known to the reader of this thesis, a composite material is created by assembling two or more different materials to create a new material that combines the best characteristics of each, or introduce a new set of features that none of the individual components could achieve alone [1]. Therefore, the created composite material displays superior properties than those of its individual constituents [2]. More specifically, a typical category of composite materials are the so-called fiber reinforced composite materials, which consist of high-strength, high-modulus fibers embedded within or bonded to a matrix, with clear interfaces separating them. The role of the fibers is to transfer the loads effectively within the material and typically, in most applications they are glass, carbon or Kevlar fibers (with some limited use of also boron, silicon carbide and aluminum oxide fibers), which come in either short, long or continuous form. On the other hand, the matrix maintains the fibers' position and orientation, facilitates load transfer between them, and protects them from environmental damage, such as high temperatures and humidity. Usually, the matrix is a polymer, metal or ceramic and in the case of a polymer matrix, two different categories can be distinguished: thermoset (which are the most common) and thermoplastic matrices [3].

Composite materials and especially carbon fiber reinforced polymers (CFRP) are well-known for their exceptionally high strength-to-weight ratio compared to metals [3]. This characteristic is the main reason of the widespread use of composite materials today, in several sectors (automotive, sports equipment, renewable energy etc.) that demand structures with excellent strength but also as low weight as possible. One of the main fields that composite materials gain more and more use over traditional materials such as steel, aluminium and titanium (as can be seen in Figure 1.1) is the aerospace sector. To give a relevant example, around 53% of the total airframe weight of Airbus A350 is made of composite materials (Figure 1.2).

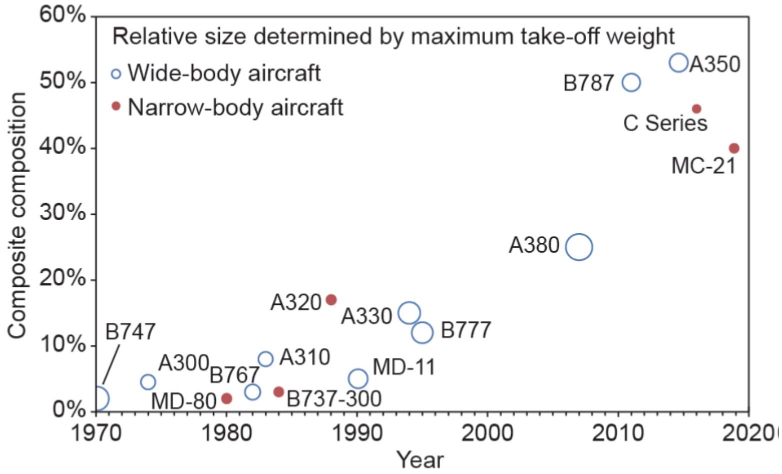

Figure 1.1: Evolution of composite material use in aircraft over the years [4]

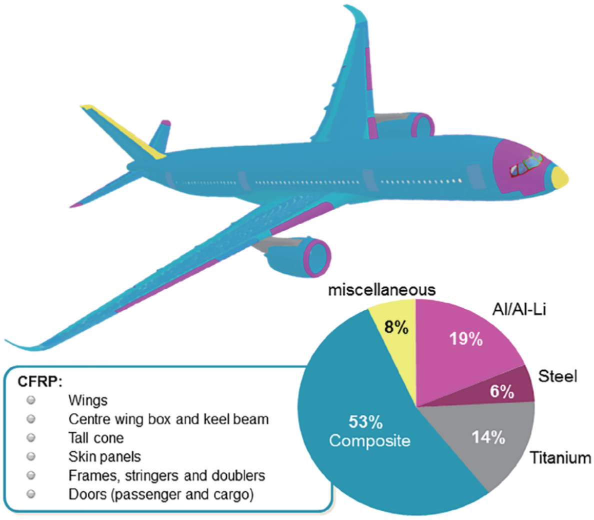

Figure 1.2: Material distribution on Airbus A350 [5]

As aforementioned, the increased percentage of composite materials in modern aircrafts (such as the Airbus A350), drives the need for improvements in the rate and economy of composite manufacture. For this reason, many manufacturing processes with high degree of automation are becoming increasingly popular. One of these processes is the so-called Automated Fiber Placement process (AFP), whose increased use over the years is evident in Figure 1.3.

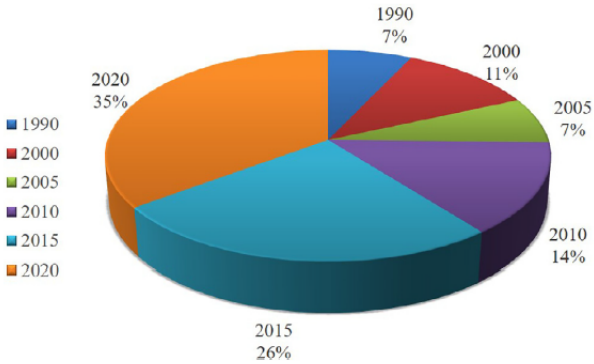

Figure 1.3: Adaptation of AFP over traditional manufacturing processes for composites [6]

During AFP, a gantry or robotic system with a fiber placement head is used to lay multiple strips of composite material, known as tows, onto a tool surface. The tows are pre-impregnated with resin (hence the name prepreg) and their typical width ranges from 1/8" to 1" (3.175 mm to 25.4 mm) [7]. To ensure adhesion between the incoming tows and the substrate, appropriate process conditions such as heating, compaction, and tensioning are used. The fiber tows are organized into courses, which are then combined to form a ply, and multiple plies are layered together to create a laminate [8] [9].

To better understand the details of the AFP process, it is essential to examine its operational principles. The AFP process begins with the material supply unit (Figure 1.4), where spools of prepreg tows are loaded. The feeding system then pulls the tows from these spools and guides them to the compaction roller. As the AFP head moves along the tool path, the tows are cut to the required length by an integrated cutting mechanism. The compaction roller presses the tows onto the mould surface, something that ensures proper adhesion and minimizes air pockets. The tows are then guided accurately onto the mold surface by a guiding unit, and in some systems, a heating element (as aforementioned) may be used to soften the resin, improving adhesion and compaction. To finish the course, the tows are cut perpendicularly to the travel direction and the AFP machine head is repositioned for the next course [10] [11]. A schematic view of the AFP process, as well as a real-life AFP system can be seen in Figures 1.4 and 1.5 below.

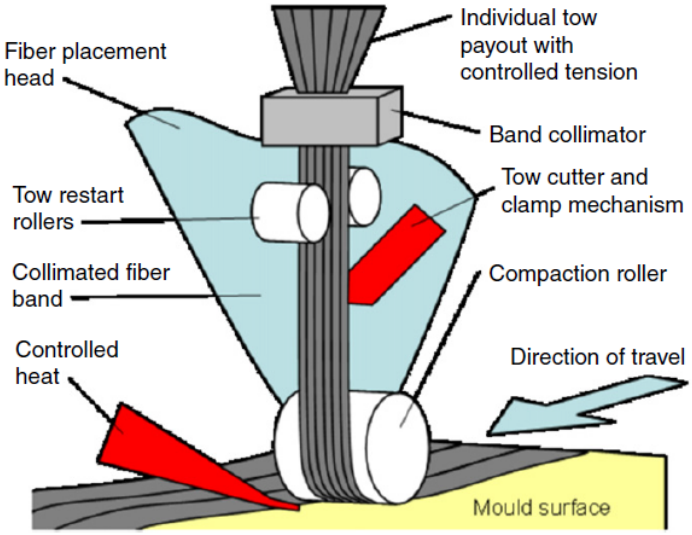

Figure 1.4: AFP machine head with basic parts [12]

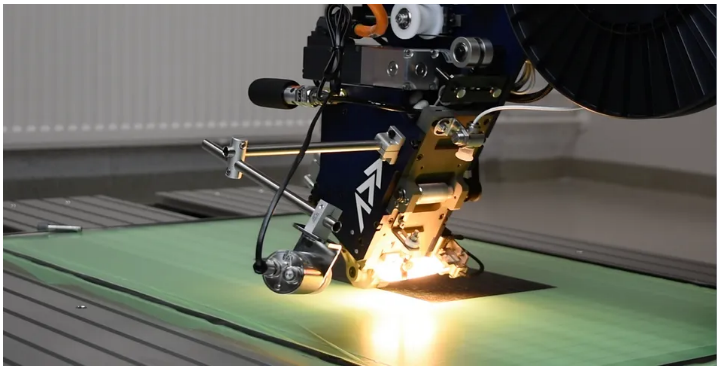

Figure 1.5: AFP system [13]

It is clear that when applied on flat moulds, the AFP process is relatively straightforward and can produce laminates with high reliability and accuracy, especially when laying down courses that are composed of straight tows. However, during AFP, there is also an option to lay down courses with tows that are steered according to specific guidelines. This process is called tow steering (or fiber steering, since a tow consists of multiple fibers). A good example of flat panels with extensive implementation of fiber steering are the so-called Variable Stiffness Panels (VSP) or Variable Stiffness Laminates (VSL), which are AFP-produced laminates with fiber paths that are not straight, but curvilinear (Figure 1.6 right). The main reason for constructing panels with steered tows is to combine the stiffness and strength properties of the laminate with specific load requirements. By steering tows along curvilinear paths, the fiber orientation can be optimized to align with the principal stress directions, improving performance under complex loading conditions.

Apart from flat surfaces, fiber steering can be implemented on curved surfaces as well. This feature is particularly common in the manufacturing of CFRP-based pressure vessels, such as those used for storing pressurized gases, such as fuels or oxidants, in aerospace (or other) applications. These structures often feature complex curved geometries, including domed cap ends and cylindrical sections, where maintaining optimal fiber alignment is essential to withstand internal pressures efficiently. AFP allows for precise placement of fibers along curvilinear paths, ensuring the laminate meets the strength and stiffness requirements for both axial and hoop loading (details about stress states in pressure vessels can be found in Chapter 4). Due to specifications and requirements, it is crucial that each layer of the laminate that composes a pressure vessel has the correct fiber orientation, according to the nominal design. In the case of complex curved geometries (such as the cylindrical or dome-shaped

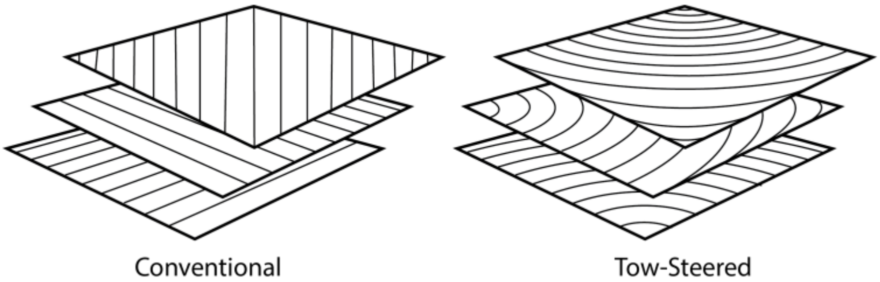

Figure 1.6: Panels with conventional straight tows and steered tows [14]

sections of the vessel), this is harder to achieve, and it is possible that a deviation between the nominal (desired) and actual fiber orientation angle occurs. Specifically, as the fiber tows are laid onto the curved surfaces, they must conform to the shape, which causes stretching, compression, or distortion of fibers to accommodate the surface curvature. Hence, it is essential to steer the tows appropriately, guiding them through a non-linear path, to meet the specific requirements [15].

Fiber steering is beneficial in terms of accuracy of the final product, but can cause defects in the laminate, including tow misalignment, tow waviness, tow wrinkling and upfolding [10]. However, one of the most significant and common type of imperfections during AFP, largely due to fiber steering (as will be explained in the following chapters) are gaps and overlaps. In a general context, gaps, as the name suggests, are regions in the laminate (on the surface or internally) where a spacing between adjacent fiber tows occurs (Figure 1.7 left). This spacing is typically filled with resin after curing, resulting in the so-called ”resin (or matrix) pockets”. On the other hand, overlaps occur when fiber tows are placed too closely together, causing them to overlap each other and thus creating regions of increased thickness (Figure 1.7 right). A categorization of these manufacturing defects, according to the way they are created, will be made in Chapter 2, where more details will be given. As discussed in the same chapter, this thesis will focus on evaluating the impact of gaps on composite structures, particularly those with curved geometries, such as pressure vessels.

The present thesis has been carried out in close collaboration with Airborne Aerospace, a company that manufactures composite structures for aerospace applications. Given this partnership, it was both logical and advantageous to align the research on AFP-induced manufacturing defects with Airborne’s existing projects, thereby addressing areas of mutual interest. The following chapters will present, discuss and analyze all the relevant details taken into consideration in the context of this work.

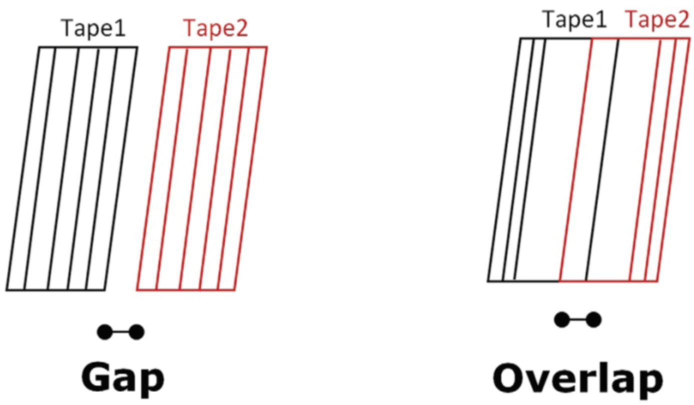

Figure 1.7: Gaps and overlaps schematic [16]

2

Literature Review

2.1. Gaps and overlaps as defects induced by AFP

AFP is a process that offers plenty of advantages in the manufacturing of composite structures, including and not limited to increased efficiency, complex geometry manufacturing, material optimization and weight reduction. Nevertheless, these advantages rarely come without any cost. There are several categories of imperfections (or defects) induced by AFP and most of them are well summarized in the works of Harik et al. (2018) [17] and Heinecke and Willberg (2019) [10]. Among all these manufacturing induced defects, as mentioned, perhaps the greatest importance can be found in the so-called gaps and overlaps.

With the incorporation of fiber steering in AFP, two categories of gaps and overlaps can be distinguished: the ones due to tow misalignment and the ones due to the cutting (or dropping) of tows. From here on, the former type of gaps and overlaps will be referred to as tow-to-tow gaps/overlaps and the latter type as tow-drop gaps/overlaps. Tow-to-tow gaps and overlaps are created when the shifted method is used to lay down the courses during AFP (Figure 2.1). Specifically, during the shifted method, each new course that is laid down is identical in shape to the reference path (which is represented by the tow-path centerline) but shifted by a specified distance s perpendicular to the direction of variation (along the y' coordinate) [18] [19]. Thus, because with the shifted method the tows cannot be placed perfectly next to each other so that the separate tow boundaries are merging (tow misalignment), tow-to-tow gaps and/or overlaps are formed.

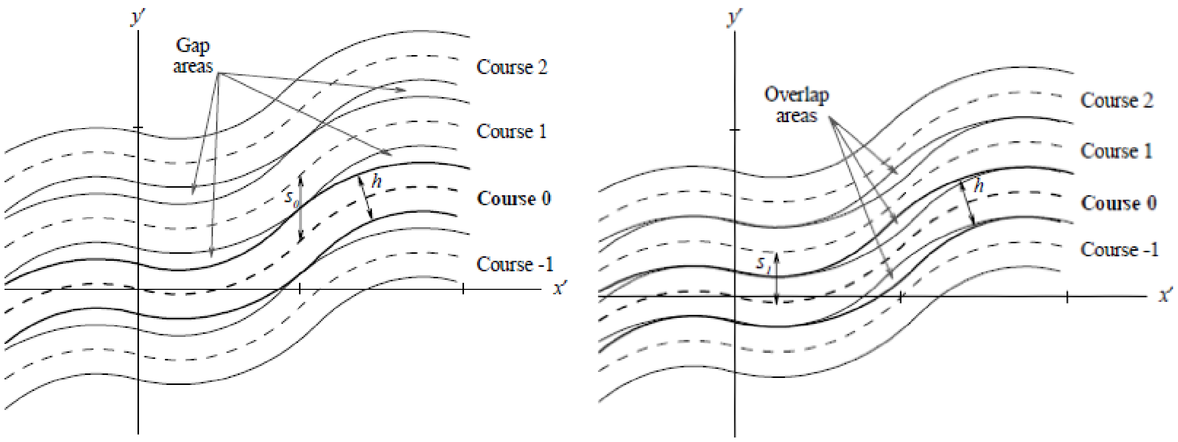

Figure 2.1: Schematic view of tow-to-tow gaps (left) and overlaps (right) [18]

The tow-drop method involves cutting a tow perpendicularly to the fiber direction at specific intervals, with the drop positions determined by a chosen coverage strategy (0%, 100% or any other percentage in between). In the 0% coverage case, the tow is dropped when one edge aligns with the adjacent course edge, creating a fiber-free gap. In the 100% coverage case, the tow is cut after both edges pass the adjacent course, causing an overlap. A 50% coverage combines these two approaches (Figure 2.2). Thus, if no overlaps are desired, the 0% coverage is used, while if no gaps are desired, the 100% coverage is selected [20].

AFP is widely used in manufacturing structures with doubly-curved surfaces. Due to the geometric complexity of these surfaces, the finite width of the fiber tapes prevents perfect alignment without overlaps. To avoid overlaps, modern AFP systems use a technique called 'tow-dropping,' which creates the characteristic triangular gaps in the lay-up (hence the naming tow-drop for this type of gaps - Figures 2.2, 2.3) [7]. Such doubly-curved structures are prevalent in the aerospace industry, appearing in components like aircraft and rocket fuselage panels, nose cones, and fuel tanks. Consequently, understanding the effects of these tow-drop gaps is critical for ensuring the production of high-quality composite laminates in aerospace applications.

In the production of composite laminates, ensuring structural integrity requires careful management of gaps and overlaps introduced by the AFP process. One technique used to address these challenges is "staggering", where plies of the same orientation are intentionally shifted relative to one another. Staggering prevents the alignment of course boundaries, overlaps, and tow-drop gaps across successive plies, reducing the likelihood of stress concentrations and weak points in the laminate and is a method that is very often used to mitigate the effects of accumulated AFP-induced manufacturing defects.

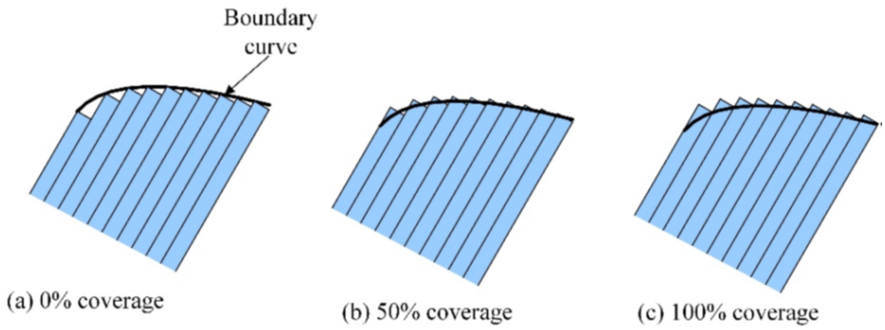

Figure 2.2: Coverage strategies using tow drops in AFP [20]

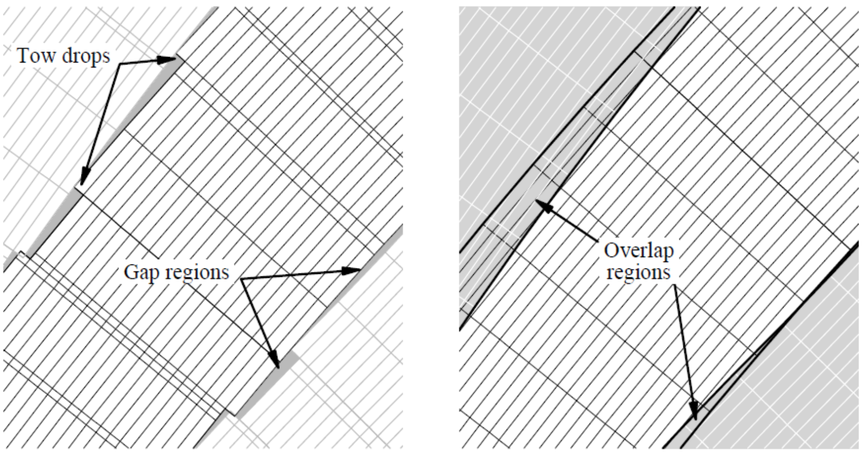

Figure 2.3: Schematic view of tow-drop gaps (left) and overlaps (right) [18]

2.2. Failure criteria for composites

In order to estimate and quantify damage initiation, progression and failure in composite materials, numerous failure criteria have been developed. These failure criteria are mathematical models or frameworks designed to predict the initiation and evolution of damage in composite materials under various loading conditions. They account for the unique anisotropic and heterogeneous properties of composites, addressing mechanisms such as fiber breakage, matrix cracking, fiber-matrix debonding, and delamination. In this section, some of the most widely used failure materia will be presented, along with the failure criterion that was ultimately selected to be used for failure assessment in this thesis.

2.2.1. Maximum Stress Failure Criterion

This is one of the simplest failure criteria, in which the strength parameters are compared against the stresses parallel and perpendicular to the fiber direction within each ply. If these stresses are smaller than the respective strength parameters, no failure occurs. In a mathematical sense, the Maximum Stress Failure Criterion is described as follows [21]:

$$\begin{aligned} &\sigma_{11} < X_T \quad \text{(if } \sigma_{11} \text{ is tensile)} \quad \text{or} \quad \sigma_{11} < X_C \quad \text{(if } \sigma_{11} \text{ is compressive)}, \\ &\sigma_{22} < Y_T \quad \text{(if } \sigma_{22} \text{ is tensile)} \quad \text{or} \quad \sigma_{22} < Y_C \quad \text{(if } \sigma_{22} \text{ is compressive)}, \\ &|\tau_{12}| < S. \end{aligned} \tag{2.1}$$

where:

- σ_{11}, σ_{22}: ply stresses in the ply coordinate system (11 parallel to fibers, 22 perpendicular to fibers),
- τ_{12}: shear stress in the ply plane,
- X_T, X_C: tensile and compressive strengths in the fiber direction,
- Y_T, Y_C: tensile and compressive strengths in the transverse direction,
- S: shear strength in the ply plane.

As long as Equations 2.1 hold, there is no failure. The Maximum Stress Failure Criterion, while quite straightforward, presents significant drawbacks that reduce its accuracy and applicability in complex stress scenarios. One such disadvantage is the fact that it does not account for the interaction between different stress components, such as normal and shear stresses. Ignoring this interaction can lead to inaccurate predictions of failure, particularly in cases involving multidirectional loading. To solve this issue, other failure criteria that do take into account this combined effect of different stress components were developed.

2.2.2. Tsai-Hill Failure Criterion

As discussed, in general, stresses can interact and cause failure, even if each stress component, when compared individually to its allowable limit, indicates no failure. One of the most significant failure criteria that account for this interaction is the Tsai-Hill criterion. This criterion calculates a so-called Failure Index (F.I.), based on the different stress components in a ply and compares this index to unity. If F.I < 1, no failure occurs. To express it mathematically [21]:

$$F.I. = \frac{\sigma_{11}^2}{X^2} - \frac{\sigma_{11}\sigma_{22}}{X^2} + \frac{\sigma_{22}^2}{Y^2} + \frac{\tau_{12}^2}{S^2} < 1 \tag{2.2}$$

where:

- X: Corresponds to the strength in the fiber direction when only σ_x acts on a ply.
- Y: Corresponds to the strength in the transverse direction when only σ_y acts on a ply.

Although the Tsai-Hill criterion does not ignore the interplay among different stress components like the Maximum Stress criterion, it still doesn't accurately implement the different strengths composites have in tension and compression. In order to tackle this issue, further developments in failure criteria had to be made.

2.2.3. Tsai-Wu Failure Criterion

The Tsai-Wu failure criterion, which is a generalized version of the Tsai-Hill criterion improves upon the Tsai-Hill criterion by incorporating stress interactions, as well as the ability to account for the different strengths of composites in tension and compression, providing a more comprehensive approach to predicting failure. It is expressed as follows [21]:

$$F.I. = \frac{\sigma_{11}^2}{X_T X_C} + \frac{\sigma_{22}^2}{Y_T Y_C} - \frac{\sigma_{11}\sigma_{22}}{\sqrt{X_T X_C Y_T Y_C}} + \left(\frac{1}{X_T} - \frac{1}{X_C}\right)\sigma_{11} + \left(\frac{1}{Y_T} - \frac{1}{Y_C}\right)\sigma_{22} + \frac{\tau_{12}^2}{S^2} < 1 \tag{2.3}$$

As before, if F.I. becomes equal to (or higher than) 1, failure occurs.

2.2.4. Hashin Failure Criterion

As can be concluded from the short discussion above, the failure criteria presented so far become progressively more complex, taking into account more and more parameters and details that improve accuracy in failure predictions. However, they all still calculate a single Failure Index, which does not differentiate between the various failure modes in a composite laminate. In essence, they can estimate *if* failure occurs, but not *what type* of failure occurs. The Hashin criterion addresses this limitation by distinguishing between different failure modes, such as fiber failure (tensile or compressive) and matrix failure (tensile or compressive). For this reason, this is the selected failure criterion in the context of this thesis, to evaluate composite failure. In a mathematical form [22], [23]:

Tensile Fiber Failure Mode (if $\sigma_{11} > 0$):

$$F.I. = \frac{\sigma_{11}^2}{X_T^2} + \frac{\tau_{12}^2 + \tau_{13}^2}{S_{12}^2} < 1 \tag{2.4}$$

Compressive Fiber Failure Mode (if $\sigma_{11} < 0$):

$$F.I. = -\frac{\sigma_{11}}{X_C} < 1 \tag{2.5}$$

Tensile Matrix Failure Mode (if $\sigma_{22} + \sigma_{33} > 0$):

$$F.I. = \frac{(\sigma_{22} + \sigma_{33})^2}{Y_T^2} + \frac{\tau_{23}^2 - \sigma_{22}\sigma_{33}}{S_{23}^2} + \frac{\tau_{12}^2 + \tau_{13}^2}{S_{12}^2} < 1 \tag{2.6}$$

Compressive Matrix Failure Mode (if $\sigma_{22} + \sigma_{33} < 0$):

$$F.I. = \left(\frac{\sigma_{22}}{2S_{23}}\right)^2 + \left[\left(\frac{Y_C}{2S_{23}}\right)^2 - 1\right]\frac{\sigma_{22}}{Y_C} + \left(\frac{\tau_{12}}{S_{12}}\right)^2 < 1 \tag{2.7}$$

2.3. Summary and discussion of relevant research

To fully answer the questions posed in this thesis, it is crucial to build on the foundational knowledge established by previous studies. The following research works have significantly contributed to understanding the impact of the AFP-induced manufacturing defects, and were thus the backbone of this research. Note that these studies address both tow-to-tow and tow-drop gaps and overlaps. However, during the literature study phase of this thesis, a greater focus was given on studies covering tow-drop defects, as these are the primary concern of the present research.

2.3.1. Impact on mechanical strength

The following research studies focus on the effects of AFP-induced manufacturing defects on the mechanical (tensile and compressive) strength of composite structures. Some address the issue experimentally through mechanical testing, others through modelling, and some combine both approaches.

Experimental studies

This section presents and discusses studies that evaluate the impact of gaps and overlaps following an experimental approach.

One of the first studies that tried to examine the impact of defects induced by AFP on the mechanical performance of composite laminates was the one carried out by Croft et al. (2011) [24]. It was an experimental study, focused on four primary defect types: gap, overlap, half gap/overlap, and twisted tow. These defects were evaluated under various mechanical tests. Specifically, un-notched specimens were tested in tension, compression and in-plane shear, and notched specimens containing a central open hole were tested in tension and compression. The defects investigated are tow-to-tow defects and their width is equal to the width of one tow. The authors do not mention specific material details, therefore it is unknown what the exact width of the tow is. However, in other studies that will be analyzed later on, a typical tow width is 1/4" (6.35 mm), so it can be assumed that this is also the case in this work. For all tests, 16-ply thick specimens were used according to relevant testing standards. Regarding the results, un-notched panels with pure gaps were noted to have a 2.12% reduction in tensile strength and a negligible 0.81% reduction in compressive strength. On the other hand, un-notched panels with pure overlaps showed a very small increase in tensile strength (0.97%), but a much larger increase in compressive strength, at 7.17%. The un-notched panels are the main point of interest of this paper in the context of the present thesis, since in the open hole tests performed, the results are likely dominated by the stress concentration imposed by the presence of the hole, so it is challenging to deduce any definite conclusion for the impact of the defects alone on mechanical performance. It is worth noting that the defects were manually inserted during specimen manufacture and were not the result of a real tow-drop procedure in an AFP machine. For example, to create the gap configurations, the researchers removed two tows one on top of the other. Therefore, the validity of the findings for AFP induced defects cannot be assured.

In the same context, the research paper by Falcó et al. (2014) [25] investigated the mechanical performance and defect tolerance of Variable Stiffness composite panels manufactured using the AFP process, under in-plane tensile loading. The paper's objective was to quantify the effects of tow-drop defects and evaluate different manufacturing parameters to mitigate their influence. Three configurations were tested: one with 0% gap coverage (generating triangular fiber gaps), one with 100% gap coverage (allowing small overlaps), and one with 0% gap coverage but with ply staggering to avoid co-located gaps through the laminate thickness.

As in [24], specimens for un-notched tensile (UNT) and open-hole tensile (OHT) tests were designed, manufactured and tested. The specimens were designed to represent the ply discontinuities at the edges of adjacent courses in Variable Stiffness Panel (VSP) configurations. Each specimen represents a sub-domain of a larger panel, with the maximum tow-angle mismatch determined by panel dimensions, course width, and fiber angles. The study considered a worst-case scenario with a tow-angle mismatch of 12 degrees, which is a reasonable approximation given practical constraints. The test specimens consisted of straight-fiber layers, simulating the small dimensions of actual curved trajectories in a real VSP. To replicate the tow-angle discontinuities, some layers had fiber orientations of 51 degrees and 39 degrees, creating a discontinuity at the specimen's mid-length (Figure 2.4). These plies were balanced with layers oriented at ±45 degrees to maintain structural integrity. The defects are triangular, with a width of 6.35 mm (one tow width) and a length of 29.9 mm.

Digital Image Correlation (DIC) was used to analyze the strain fields and observe the influence of defects, particularly in damage-prone zones, prior to structural failure. High-resolution photography further aided in understanding the failure mechanisms. Regarding the results, in general the 0% coverage (only gaps, no staggering) resulted in strength reductions of 22% in the un-notched specimens. In addition, specimens containing only overlaps also seem to reduce the tensile strength in the un-notched specimens by up to 9%. This comes in contrast with the results in [24], where overlaps showed a marginal tensile strength increase, but it is questionable to what extent these two studies can be compared, as there are key differences in the defects geometry and introduction.

Another key aspect of this study is that the defects in the tested specimens extended to the specimen edges, making them subject to the so-called "free-edge effects". These are the effects of free edges in composite laminates with varying ply orientations, and are a result of the discontinuity in mechanical constraints at the free edge, leading to complex stress states, including interlaminar normal and shear stresses [26]. These complex stress states near the free edges can significantly influence the mechanical behavior of the laminate, particularly under tensile or shear loading conditions. The stress concentrations at the edges often act as initiation sites for damage mechanisms such as delamination, matrix cracking, or fiber-matrix debonding, which can propagate and compromise the structural integrity of the laminate. Indeed, in the un-notched specimens of this study, delaminations that were uniformly distributed along the specimen edges were observed. These delaminations are thought to have a major impact on the final failure of the specimens. Therefore, it cannot be concluded with absolute certainty whether the strength knockdown that was observed was mainly due to the defects themselves, or due to the free-edge effects.

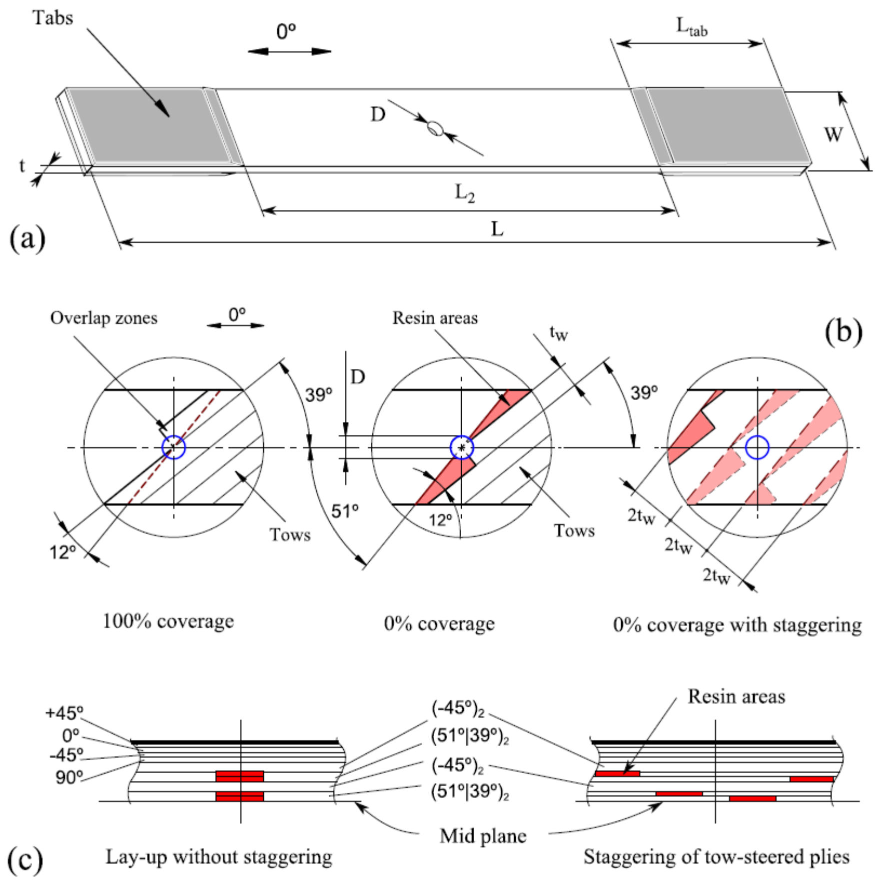

Figure 2.4: The design of specimens used in Falcó et al. (2014) [25]

Nguyen et al. (2019) [27] also dealt with the effect of manufacturing defects induced by AFP on the mechanical properties of composite structures from an experimental point of view. In this study, specimens with controlled gap and overlap defects of varying widths (from 1/32" or about 0.8 mm to 1/2" or 12.7 mm) were manufactured and tested. The pre-test microscopy quantified changes in geometry due to compaction, namely reduced gap size and increased overlap length due to consolidation and autoclave pressure, gap filling with resin (resin-rich pocket) and bent plies (fiber undulation) - Figure 2.7. Results showed that gaps significantly reduced mechanical properties. The detailed failure analysis using digital image correlation (DIC) and microscopy revealed that gaps primarily initiated failure modes that propagated rapidly, while overlaps tended to distribute stress more evenly, delaying the onset of failure.

All specimens containing defects featured 16 plies, with 8 of them (only the 0° and 90° ones) containing defects. The way the gaps were introduced was by using two cut lines within the desired ply parallel to the fiber orientation. Then, after aligning and attaching the ply to its adjacent plies, these cut lines were removed, therefore leaving a gap between tows (Figure 2.6). It is important to note that this method of manually introducing gaps into the specimens has limitations in accuracy and realism.

Additionally, two distinct categories of specimens were established: those with defects only in the 90° plies (designated as "minus" (-) specimens) and those with defects in both the 0° and 90° plies (designated as "plus" (+) specimens). This is important, as the orientation of the defects plays an important role in strength knockdown, as demonstrated by the results.

Specifically, the (-) specimens exhibited a strength reduction of up to 26%, while the (+) specimens experienced a significantly greater strength reduction of approximately 55%. This difference can be attributed to the fact that the 0° plies are responsible for carrying the majority of the load and thus, gaps (or to put it simply, loss of material) in the 0° plies result in a substantial loss of strength. Tensile strength reduction is also directly related to gap size (as also demonstrated by Blom et al. (2009) [28] which will be discussed later); the maximum reduction is observed for a 1/2" wide gap (the largest gap size examined) in the (-) configuration (26%), while smaller gaps (1/32") still caused a noticeable 10% reduction in the same configuration. The tensile strength reduction in this case can be well approximated by a linear fit (Figure 2.5).

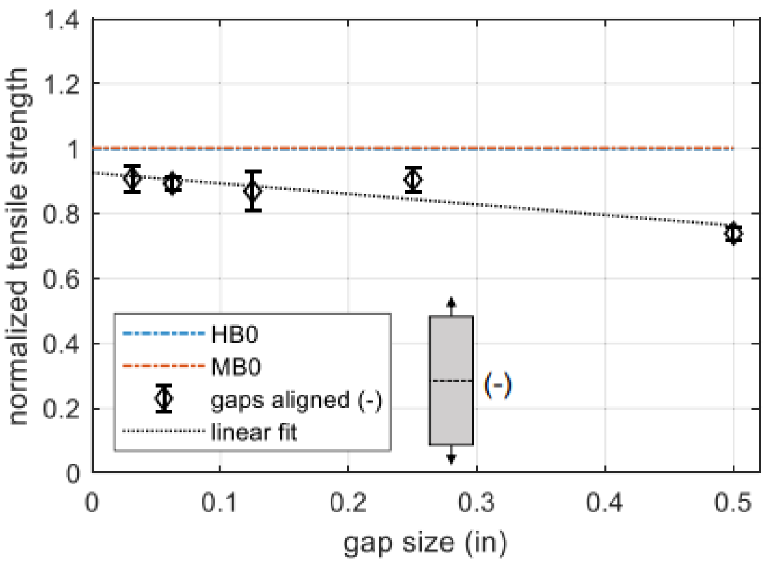

Figure 2.5: Tensile strength reduction for different gap sizes [27]

As for the compressive strength, the maximum strength knockdown due to gaps was observed to be again close to 55% for the (+) configuration. These results suggest that the presence of gaps in plies with different orientations significantly worsens strength reduction. On the other hand, in the same research, overlap specimens showed a different trend. Overlaps in the (+) configuration and up to 1/2" in size, resulted in a 20% improvement in tensile strength. The view in compressive strength is more complicated, with the (-) specimens dropping the strength by as much as 20%, but the (+) specimens increasing it by around 10%. This further highlights that the impact of overlaps is more complex than that of gaps and is influenced by multiple factors.

All comparisons were made against baseline panels containing no gaps or overlaps. However, the validity of these comparisons for the tensile properties can be challenged, since as stated in [27]: *For each layup method, two benchmark panels without controlled defects were manufactured: An 8-ply laminate for benchmark tensile tests and a 16-ply laminate for benchmark compressive tests. All the defect panels were made of 16 plies.* (Nguyen et al. (2019) [27], p.3). It is reasonable to assume that a panel with double thickness is expected to exhibit a higher maximum tensile load than the baseline. However, defects in these panels reduce their failure load, making it unclear how much of the reduction is solely due to the gaps. For a more accurate comparison, both types of panels should have the same laminate thickness.

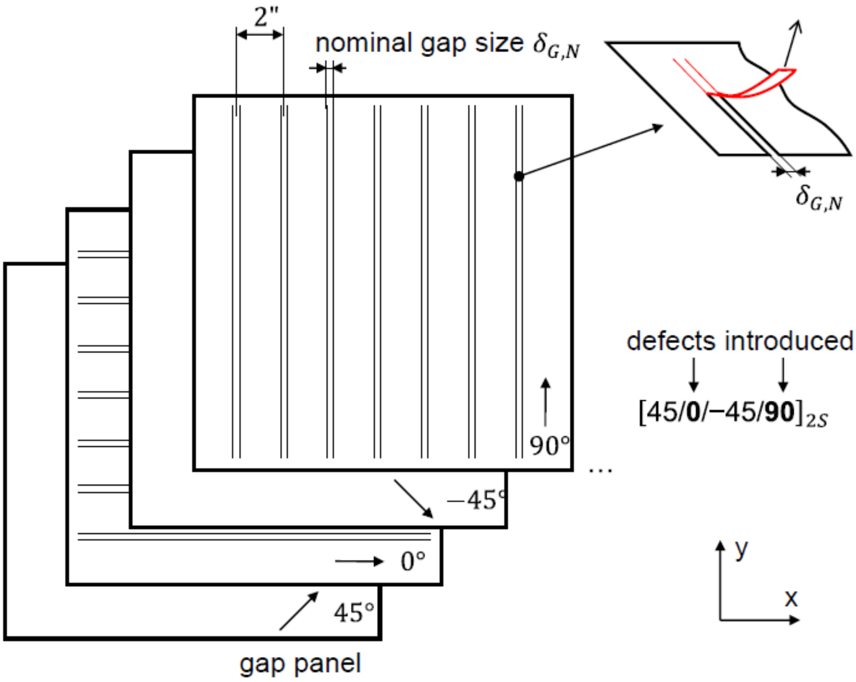

Figure 2.6: Schematic of gaps and overlaps formation during panel manufacturing [27]

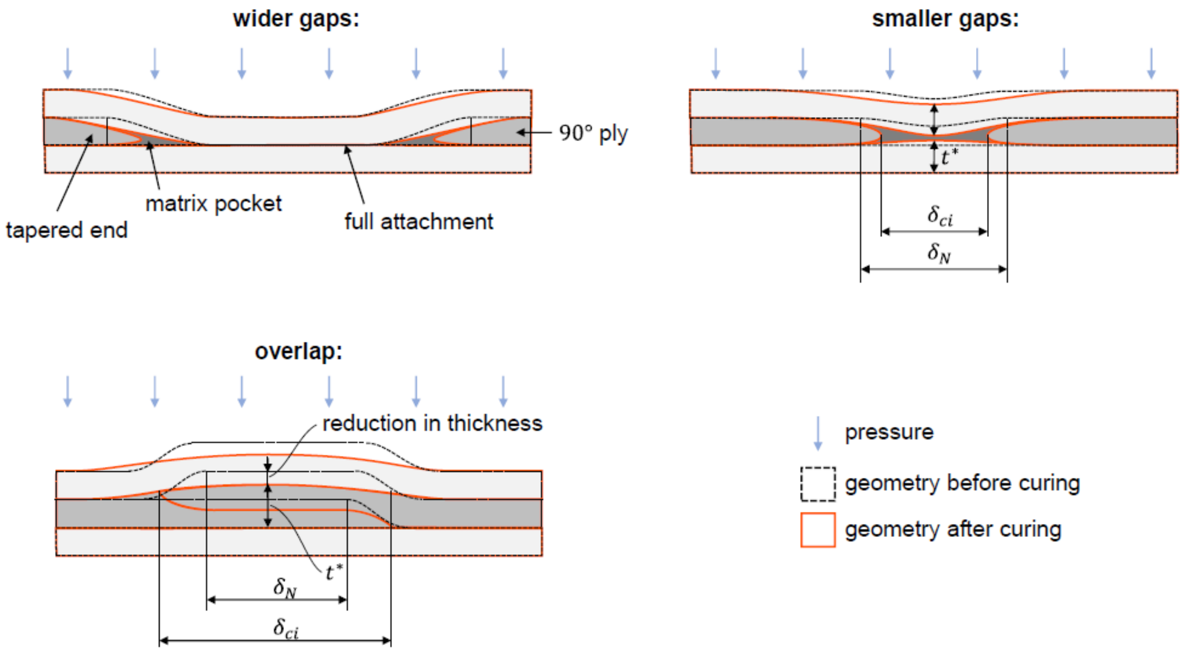

Figure 2.7: Consolidation effects on gaps and overlaps [27]

Numerical studies

The following section presents studies that primarily use Finite Element Method simulations to assess the effects of AFP-induced manufacturing defects.

One study that really stands out and can be considered one of the most influential works in this field, is the one conducted by Blom et al. (2009) [28], who investigated the influence of tow-drop areas on the strength of Variable Stiffness Laminates (VSL) using Finite Element (FE) simulations. The study aimed to understand how the resin-rich, fiberless areas that result from cutting tows at course boundaries during AFP, affect laminate performance.

In Blom et al. (2009) [28], virtual tests were carried out, simulating a compressive testing on a 300 x 300 mm composite panel. Fiber steering was used in the construction of the panel, with each ply in the panel having a specific fiber orientation, which follows a path defined by a reference angle (ϕ) with fibers curving outward based on a constant curvature (Figure 2.8). At the edges of the panel, the reference angle reaches its minimum value, T_0, and maximum value, T_1, respectively. A schematic of the (reduced) plate model that was used is presented in Figure 2.9, with the characteristic triangular-shaped gaps due to tow-dropping being clearly marked.

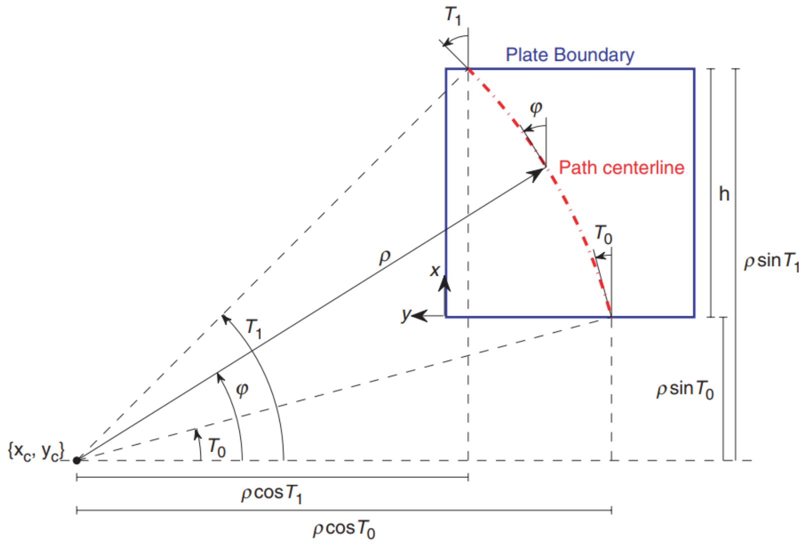

Figure 2.8: Course centerline geometry [28]

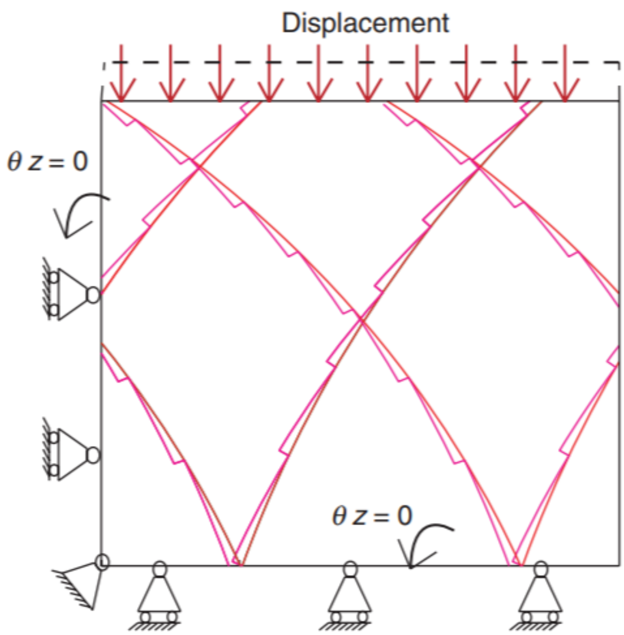

Figure 2.9: Reduced plate model (symmetric) in Blom et al. (2009) [28], with relevant boundary conditions. The triangular-shaped tow-drop gaps are visible.

The FE analyses were conducted using ABAQUS software and the LaRC03 and LaRC04 failure criteria for progressive failure analysis were implemented. These criteria focus on accurately identifying the initiation of damage under complex stress states by considering both matrix and fiber failure modes. More specifically, the LaRC04 failure criterion, which is basically a more detailed and improved version of LaRC03, distinguishes between fiber and matrix failure mechanisms, recognizing that the two materials have different responses to loading. Each failure mechanism can be further divided into longitudinal and transverse modes, resulting in the following four distinct failure modes:

- *Longitudinal tensile fracture*
  This criterion is based on a maximum allowable strain in the fiber direction, assuming no interaction with other stresses. Failure occurs if the strain along the fiber direction exceeds a threshold based on the longitudinal tensile strength.
- *Longitudinal compressive fracture*
  This mode, often seen as fiber kinking, involves compression-induced failure in fibers misaligned due to initial imperfections. The criterion depends on a combination of shear and longitudinal compression, influenced by the material's longitudinal friction coefficient and fiber misalignment angle.
- *Transverse fracture perpendicular to the laminate mid-plane ($\alpha_0 = 0°$)*
  This matrix-dominated failure mode is triggered by in-plane shear and transverse tensile stresses or in-plane shear combined with slight transverse compression.
- *Transverse fracture with $\alpha_0 = 53°$*
  Under high transverse compressive stresses, the matrix can fail along an oblique plane (around 53° to the mid-plane), something that is taken into account in this failure mode.

The four failure modes of the LaRC04 failure criterion can be visualized in Figure 2.10. The mathematical formulations regarding the LaRC03 and LaRC04 failure criteria involve a number of parameters and theoretical notions that would take too long to analyze in the present thesis. For further information, the reader is advised to read the work of Blom et al. (2009) [28], or even the relevant papers that first proposed these criteria ([29], [30]), where all the details are discussed.

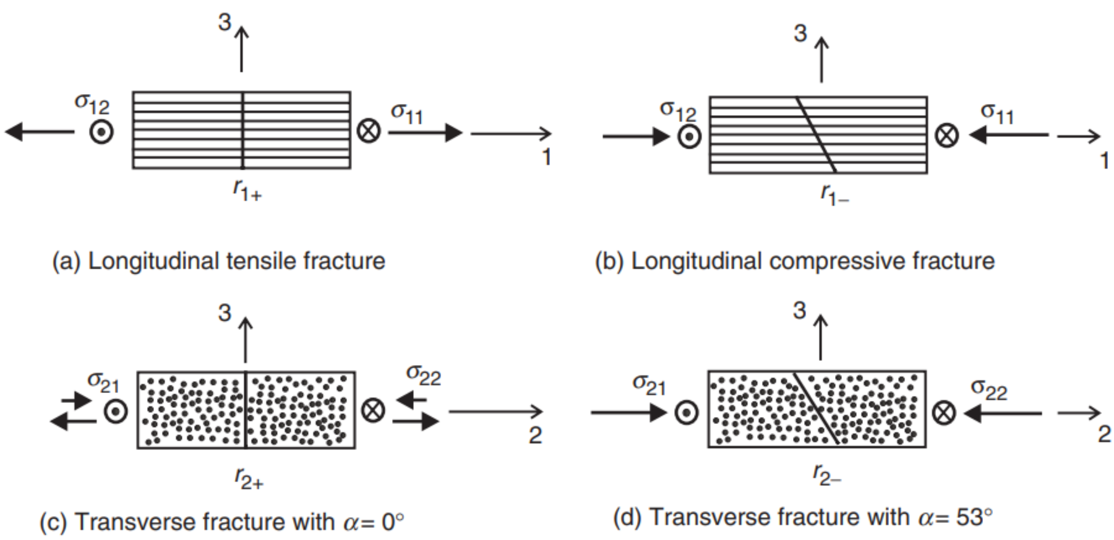

Figure 2.10: Failure modes predicted in the LaRC04 failure criterion [28]

The results in the study of Blom et al. (2009) [28] showed that wider tows reduced the laminate compressive strength (due to larger tow-drop areas and thus larger gaps) and failure predominantly occurred at tow-drop locations in both surface and underlying plies. More specifically, the strength reduction varies from 3-15% for the smallest tow width, 5-24% for intermediate tow width, and 15-29% for the largest tow width. Note that a larger tow width corresponds to a larger gap, allowing for a correlation between gap size and compressive strength reduction to be drawn from this study's results. Generally, a larger gap results in a greater compressive strength reduction. For reference, the maximum gap area observed was 12% of the ply area, found in the panel with the largest tow width, which showed the greatest compressive strength reduction of 29%.

Based on the above, a reasonable question might be: How could a small tow width (meaning a small gap) have a strength reduction of 10% (within the 3-15% range), while an intermediate tow width (meaning a larger gap than previously) could have a lower strength reduction of 5% (within the 5-24% range), given that strength reduction generally increases with gap size? The answer here lies in the fact that other parameters also play a role in the compressive strength knockdown. The strength reduction ranges reflect more than just gap size, as other factors like fiber orientation and staggering significantly influence the results. Higher ϕ values introduce more matrix-dominated failures, as the matrix must bear greater transverse stress, while lower ϕ values (fibers more aligned with the load) lead to fiber-dominated failures like kinking in compression. Therefore, a small tow width (small gap) with a high fiber orientation angle (ϕ) and no staggering could lead to a higher strength reduction, as this combination increases matrix damage and stress concentrations. Conversely, an intermediate tow width (intermediate gap) with a favorable fiber angle and staggered gaps might yield a lower strength reduction because the staggering helps distribute stresses and reduces the impact of the larger gaps. Thus, while gap size generally correlates with strength reduction, fiber orientation and staggering can also impact the exact knockdown range. A more detailed discussion on the effect of staggering follows later in this chapter.

Li et al. (2015) [16] also investigated the impact of manufacturing defects in AFP processes on the mechanical strength of composite laminates. Their research was based on Finite Element Modelling (FEM) and it concerned tow-to-tow gaps and overlaps. They developed 3D meshing tools to model ply-by-ply structures incorporating intra-ply and inter-ply cohesive elements. The former elements were placed parallel to the fiber orientation, at the interfaces between different areas and were used to account for potential splitting, while the latter ones were inserted between all plies to account for potential delamination. The authors explicitly simulated out-of-plane waviness and ply thickness variations caused by the defects (Figure 2.11), something that had not been done for example in [28]. The defects measured 30 mm in length in 90 degree plies (matching the specimen's width), or around 21 mm in +/- 45° plies (again running through the whole specimen). However, the defect widths varied between 1, 2, 3, and 4 mm. Findings reveal that gaps and overlaps cause larger strength reductions in compression than in tension, with defects in 45° or -45° plies having a more pronounced effect than those in 90° plies. In 45° and -45° plies, gaps induce greater strength reductions than overlaps, while in 90° plies, overlaps lead to larger reductions, a counterintuitive observation requiring further validation. To provide some relevant values regarding strength knockdowns, it was found that gaps in +/- 45° plies reduce the tensile strength by 14% and the compressive strength by 30%. Similar knockdowns were observed for overlaps as well, this time however with the maximum strength reductions being observed for overlaps in the 90° plies (-15 % in tension and -24 % in compression). Experimental validation aligns well with FEM results, with a maximum difference of 2.95% between tests and theoretical models.

Continuing the quest for evaluating the impact of tow-drop defects in mechanical strength, in their 2017 study, Falcó et al. [31] developed a virtual testing methodology for analyzing these defects, essentially validating numerically their previous research in 2014 ([25]). The defect size and geometry was the same as discussed previously: triangular-shaped defects with a base width of 6.35 mm and a length of 29.9 mm. Using three-dimensional numerical models that incorporated different constitutive behaviours for fibre-reinforced materials, resin-rich zones, and ply interfaces, the researchers performed simulations on un-notched and open-hole coupons. Their findings indicated that tow-drop defects created significant stress concentrations, initiating damage such as matrix cracks, fiber breakage, and delaminations, which matched experimental observations at a great extent. In notched specimens, stress concentrations and crack initiation were influenced by tow-drop defects around the hole edges, with predicted damage mechanisms and failure loads aligning closely with experimental results (maximum failure load percentage difference between experiments and simulations was 8.1%). They concluded that tow-drop defects, particularly gaps and mismatches at adjacent course boundaries, acted as stress concentrators, reducing mechanical strength by promoting matrix cracking and fiber breakage. The virtual testing approach effectively simulated these effects, offering realistic predictions of damage ini-

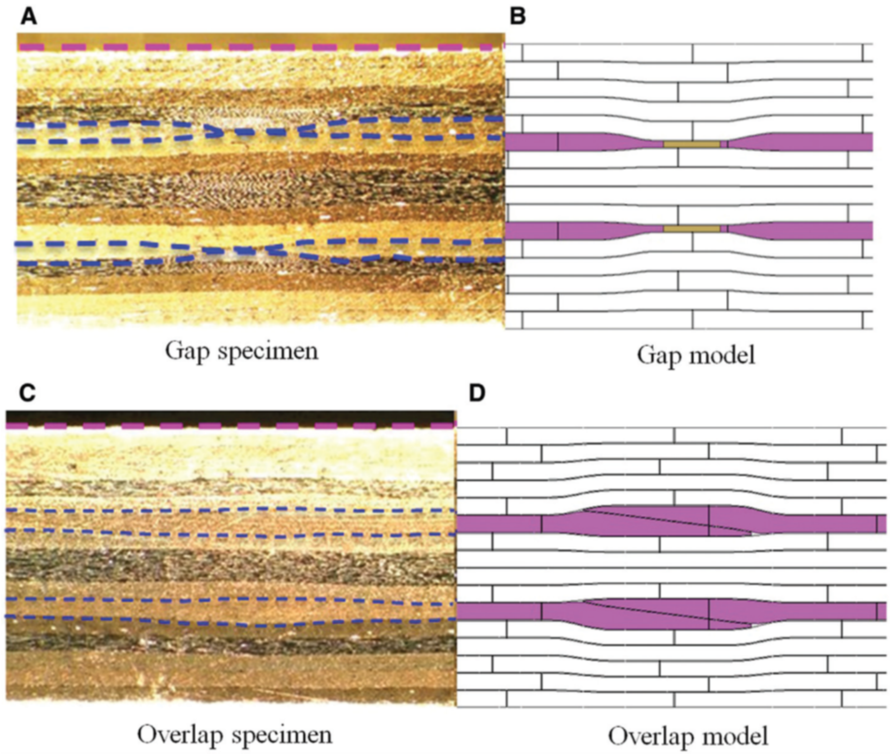

Figure 2.11: Translation of cured geometry into FEM [16]

tiation and progression. The results of simulations showed that in the un-notched configuration, gaps reduce the strength by 12.5%, while in the open-hole coupons, the impact of gaps seems to be lower (reduction of 9.1%), probably due to the higher impact of the open hole. However, the analysis of the impact of tow-drops on laminate behavior has certain limitations, as narrower specimens (such as the ones analyzed in this research) exhibit free edge effects that are not present in real laminates. These effects influence damage mechanisms, particularly delamination, making it challenging to completely isolate the influence of the defects. Therefore, again as previously mentioned, free-edge effects should be avoided to obtain a more accurate result regarding the impact of gaps and overlaps on the failure mechanisms of the laminate.

Studies with both experimental and numerical approaches

Apart from the studies discussed above, which only take one (experimental) or the other (numerical) route, there have been a few studies that combine both of these two methods and will be presented in the following section.

First of all, a research that investigated the impact of gaps and overlaps on the mechanical performance of composite laminates performing both experiments and simulations was the one by Woigk et al. (2018) [32]. The study focused on understanding how these defects affect the tensile and compressive strengths of the composites. The defect width was 2 mm, equal to one-third of the total tow width of 6 mm, and all defects ran through the whole specimen. This defect size is similar to the one investigated in Li et al. (2015) [16]. Four defect configurations were developed: ”Gaps” (containing only stacked gaps), ”Overlaps” (containing only stacked overlaps), ”Staggered Gaps” (containing only staggered gaps with a stagger distance of 2 mm), and ”Gaps & Overlaps” (containing a combination of staggered gaps and overlaps).

These four configurations were subjected to tensile and compressive tests to evaluate their effects. The ”Gaps & Overlaps” specimens were the ones that exhibited more expected strength reductions, with 7.4% in tension and 14.7% in compression. However, since these specimens contain both gaps and overlaps, isolating the impact of each defect type is challenging. Thus, it is better to more closely examine the results for the ”Gaps” and ”Overlaps” specimens.

Specimens containing only gaps presented a mixed view on the impact of these defects, as their strength was reduced under tension (although the percentage is a mere 1.3%), but increased under compression (by as much as 7.6% for unstaggered configurations). This is the first instance in the literature reviewed for this thesis where gaps have shown a positive effect on strength. The authors do not provide a clear explanation on that matter, and the fact that all other studies report the opposite conclusion for the impact of gaps on the compressive strength poses some serious doubts on the validity of this observation.

On the other hand, this time a positive influence of pure overlaps was observed: strength was increased by 3% in tension and 9.5% in compression. The observed failure behaviours were consistent with the level of ply waviness caused by the defects (Figure 2.12), suggesting that ply waviness is a key factor driving the reductions in material strength and reinforcing the idea that it should be included in FEM analyses to have an accurate comparison with experimental results.

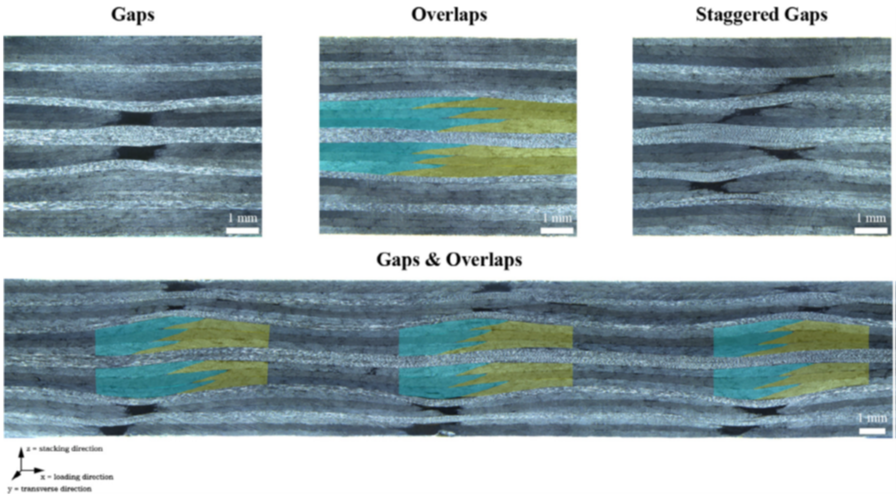

Figure 2.12: Microscopy images of specimens with visual ply waviness due to defects. Gaps are marked with black (resin-rich areas) and overlaps are marked with blue/yellow [32]

Apart from their 2019 research [27] which featured only experimental methods, Nguyen et al. (2021) [33] carried out one more study of interest about the effects of AFP-induced defects on the mechanical strength of composite laminates, this time implementing numerical approaches as well. They analyzed the same specimens as in their previous work [27]; quasi-isotropic laminates with controlled gap and overlap defects embedded within the 0° and/or 90° plies. The defects varied in size from 1/16" to 1/2". Experimental observations highlighted the progressive nature of failure mechanisms, including transverse cracks and intra-laminar splitting. Finite element models, created using Abaqus CAE with a Python script, incorporated a multiscale continuum progressive damage and failure model (MCDM) to predict the mechanical response accurately. The approach of translating the cured geometry of the laminate (with obvious fiber waviness) into FEM seems very interesting and promising (Figure 2.13). The FEM results showed relatively good agreement with experimental data for the most cases, capturing the stress concentrations and failure modes induced by the defects. The only cases with slightly larger deviations between FEM and experimental results were the 1/2" gaps and 1/8" overlaps, at 13% and 11% respectively. This means that the authors' FE model still has some limitations and indicates the high difficulty of accurately predicting such complicated phenomena. Specifically, this deviation could be attributed to the FEM model's inability to fully account for the out-of-plane fiber waviness and its impact on stress redistribution and failure mechanisms.

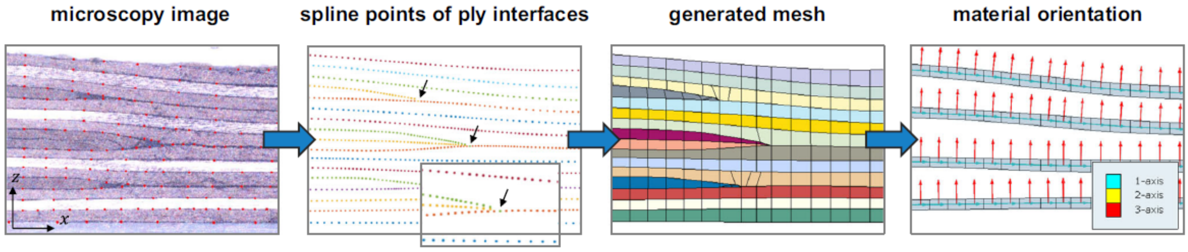

Figure 2.13: Translation of cured geometry into FEM from microscopy imaging [33]

Discussion

To summarize the above, research on the impact of AFP-induced defects, such as gaps and overlaps (either tow-to-tow ones or tow-drop ones), highlights significant effects on the tensile and compressive strength of composite laminates. Gaps were consistently found to weaken tensile strength across multiple studies due to the inherent discontinuities they introduce in the load-bearing paths of composite laminates. The resin-rich, fiberless regions created by gaps disrupt the continuity of fiber paths and reduce the effective load-carrying capacity of the laminate under tensile loading. The primary question concerns the extent to which gaps affect strength, specifically in terms of the percentage reduction in strength. As discussed in the above paragraphs, different values for strength knockdown were estimated by different researchers. For instance, Croft et al. (2011) [24] noted a 2.12% tensile strength reduction in panels with pure gaps, which aligns closely with findings from Woigk et al. (2018) [32], where gaps led to a reduction of 1.3% in tensile strength. However, other authors reported larger values for tensile strength reduction. Falcó et al. (2014) [25] observed a higher tensile strength reduction of 22% in un-notched specimens with gaps, and Li et al. (2015) [16] noted a 14% reduction in specimens with gaps in ±45° plies. A later numerical validation study of their previous work, led Falcó et al. (2017) [31] to estimate a 12.5% tensile strength knockdown, while Nguyen et al. (2019) observed that additional gaps in 0° plies (apart from gaps inserted in 90° plies) — critical for axial load-bearing — resulted in even higher tensile strength reductions, up to 55%.

With respect to compressive strength, the impact of gaps seems to be negative, as supported by most studies with strength reductions up to 0.81% (Croft et al. (2011) [24] - negligible compared to the rest), 30% (Li et al. (2015) [16]) and even 55% (Nguyen et al. (2019) [27]). However, Woigk et al. (2018) [32] reported a compressive strength increase of 7.6% due to pure gaps. However, since they do not offer an explanation for this result, this study can be considered an outlier. Hence, it can generally be said that even in compression, gaps have a detrimental effect on strength of composite structures.

Overlaps, however, have a more complex influence; some studies, like Croft et al. (2011) [24] and Woigk et al. (2018) [32], noted that overlaps could even improve tensile strength under certain conditions (by around 1% and 3% respectively). Nguyen et al. (2019) [27] estimated an even larger increase in tensile strength (20%). On the contrary, Falcó et al. (2014) showed that overlaps deteriorate strength in tension (9% reduction), an argument that is strengthened by Li et al. (2015) [34], who reported a 15% decrease. The effects of overlaps on compressive strength are equally ambiguous. Croft et al. (2011) [24] and Woigk et al. (2018) [32] observed improvements of 7.17% and 9.5% in compressive strength due to overlaps. In contrast, Li et al. (2015) [16] and Nguyen et al. (2019) [27] reported maximum decreases of 24% and 20%, respectively. Notably, Nguyen et al. also documented a compressive strength increase of approximately 10% due to overlaps (in a specimen with different overlap configuration), highlighting the inconsistency of overlap effects even within a single study.

The values discussed above about mechanical strength degradations or improvements are presented in Table 2.1. Note that these values concern un-notched specimens with stacked (not staggered) defects. Wherever there is no value (denoted by (-)) means that this specific test or defect was not examined.

Thus, the two main conclusions based on the literature review on the impact of manufacturing defects on the tensile and compressive strength of composite structures are:

1. Gaps in general deteriorate the tensile and compressive strength.
2. It is unclear what the actual impact of overlaps on the mechanical strength is.

	Max. Tensile Strength Difference %		Max. Compressive Strength Difference %	
Study	*Gaps*	*Overlaps*	*Gaps*	*Overlaps*
Blom et al. (2009) [28]	-	-	-29	-
Croft et al. (2011) [24]	-2.12	+0.97	-0.81	+7.17
Falcó et al. (2014) [25]	-22	-9	-	-
Li et al. (2015) [16]	-14	-15	-30	-24
Falcó et al. (2017) [31]	-12.5	-	-	-
Woigk et al. (2018) [32]	-1.3	+3	+7.6	+9.5
Nguyen et al. (2019) [27]	-55	+20	-55	-20

Table 2.1: Comparison of results from different studies about gaps and overlaps effect on tensile and compressive strength

However, even though a general conclusion about the negative impact of gaps has been drawn, comparing exact strength knockdown values across these studies is challenging due to varied experimental setups, including differences in defect size, distribution, and configuration within the laminates. For example, Blom et al. (2009) [28] focused on tow-drop gaps in panels produced by AFP, while Croft et al. (2011) [24] manually inserted defects, limiting the real-life replication of AFP-induced defects. Falcó et al. (2014) [25] explored ply staggering and gap coverage configurations, further differentiating their results from other studies. Additionally, Nguyen's (2019) [27] baseline comparisons are complicated by thickness variations, while Woigk et al. (2018) [32] examined both stacked and staggered configurations with unique stress distributions due to ply waviness. Therefore, although trends like strength reductions due to gaps are clear, accurately quantifying knockdown values across studies is limited. Standardized defect sizes and configurations, as well as ply orientations would be essential for reliable cross-study comparisons.

Apart from the strength knockdown caused by manufacturing defects during AFP, it is also important to compare the failure modes reported in the aforementioned studies. More specifically, Blom et al. (2009) [28] predicted fiber kinking (less relevant in the context of this thesis as it is a compression-driven failure mode) and matrix cracking triggered by transverse and shear stresses. Croft et al. (2011) [24] identified matrix cracking and delaminations, which were also predominantly noted by Falcó et al. [25] [31], along with fiber pull-out and fiber fracture. Comparable failure modes were documented to varying degrees in the studies by Li et al. (2015) [16], Woigk et al. (2018) [32], and Nguyen et al. (2019) [27]. This indicates that the primary failure modes likely to occur in the specimens analyzed in this thesis are matrix cracking, delaminations, and fiber fracture.

2.3.2. Impact on in-plane stiffness and buckling load

Apart from the scientific works presented in section 2.3.1, other studies shifted their focus to the impact of AFP-induced manufacturing defects on additional structural properties, namely the in-plane stiffness and the buckling load of composite structures. More specifically, in-plane stiffness is the ability of a (composite) material to withstand deformation when experiencing loads that act within its plane. In terms of AFP-produced composites, the manufacturing defects that are induced can significantly impact the in-plane stiffness, as the fiber undulation that occurs due to gaps and overlaps can change the distribution and orientation of fibers, leading to localized changes in stiffness. Such changes may result in an overall change (either positive or negative) in load-bearing efficiency, making it essential to estimate as accurately as possible the impact of the manufacturing defects on the in-plane stiffness. Additionally, in general the buckling load represents the critical (compressive) force at which a structural component, particularly one with a slender or thin geometry (such as a beam or a thin plate), undergoes sudden and catastrophic deformation. Regarding composites, it can be said that maintaining a high buckling load capacity is crucial, since there are a lot of applications (especially in aerospace), where lightweight materials are required to withstand compressive loads. AFP-induced defects can reduce buckling load capacity by introducing weak spots or stress concentrations that serve as initiation points for buckling under lower-than-expected loads, therefore their effect on the buckling load of structures should also not be overlooked.

As before, the studies can be categorized into numerical, experimental, or combined approaches. The following section discusses four studies that used one or both of these methods.

Fayazbakhsh et al. (2013) [35] presented a numerical study, where they introduced a novel "defect layer" method to precisely capture the geometry and location of manufacturing defects, also helping to reduce computational burdens in finite element analyses (FEA) of such phenomena. Specifically, the defect layer method modifies the finite element model by treating laminate layers with defects, such as gaps or overlaps, as distinct ”defect layers” with adjusted properties. For gap-modified defect layers, the elastic properties (e.g., stiffness and shear modulus) are reduced in proportion to the gap area percentage, while the thickness remains unchanged. In contrast, overlap-modified defect layers maintain the elastic properties of regular composite materials but have increased thickness proportional to the overlap area percentage. The defect area percentage for each element layer is determined using MATLAB subroutines, which account for the geometry and distribution of defects. These adjustments are integrated into FE models through parameterized inputs, allowing for precise and efficient analyses without the need for excessively fine meshes to capture the defect geometry explicitly, thus cutting down on computational time significantly.

The research focused on two laminate designs optimized for in-plane stiffness and buckling load, using a surrogate-based optimization algorithm. These two designs were chosen in the following manner: Design (A), which provides the highest achievable buckling load, was selected to evaluate the actual improvement in buckling performance when accounting for the influence of gaps or overlaps. Design (B), which demonstrates a higher buckling load while maintaining the same in-plane stiffness as the baseline, was chosen to assess the effect of gaps or overlaps on both design objectives. Results indicated that gaps significantly reduced both in-plane stiffness and buckling load, with a 15.1% reduction in stiffness and a 12.4% reduction in buckling load for Design (A). Conversely, overlaps were found to improve these properties, enhancing stiffness by 9.6% and buckling load by 29.9% in the same design. Regarding Design (B), the behaviour is similar, with a decrease of 14% in stiffness and 12.2% in buckling load in the gap configuration, and a respective increase of 11% and 30.5% in the overlap configuration. Note that both the baseline and the defect specimens have the same thickness, and the defect percentage area is almost identical for both Designs (A) and (B), so the comparison with the same baseline can be considered valid.

Another group of scientists that studied the impact of tow-drop defects from AFP on the stiffness and buckling behaviour of variable stiffness laminates (VSL) using simulation methods was that of Mishra et al. (2019) [36]. A novel smearing method was proposed to estimate the influence of these defects with reduced computational cost compared to existing methods (such as the ”defect layer” method presented by Fayazbakhsh et al. (2013) [35]). The research involved parameterizing the defect geometry based on design and manufacturing parameters, then using a homogenization approach to develop correlations between defect geometry and ply properties. The findings showed that the method provided conservative estimates for stiffness within 5% accuracy but unconservative results for buckling load. The study demonstrated that the proposed method is 45 times less computationally intensive than previous methods. Concerning the impact of gaps, an almost negligible reduction in stiffness was estimated (around 1%), while the decrease in buckling load was found to be higher (up to 8.3%).

While the previous studies achieved accurate numerical results, experimental work remains a valuable alternative for drawing conclusions. This is an approach that Arian Nik et al. (2014) [37] followed, by conducting an optimization study on AFP-manufactured variable stiffness composites containing tow-drop defects, in order to understand how these manufacturing-induced defects influence the two aforementioned properties. The study involved a multi-objective optimization approach to simultaneously maximize these properties. The AFP machine that was used had the capability of laying down multiple tows simultaneously, with each tow being able to be cut and restarted independently of the others. Therefore, in the context of this study, a course is composed of multiple tows, laid parallel to each other with one continuous movement of the AFP machine. It was found that increasing the number of tows within a course, while keeping the tow width constant (thus increasing the course width), reduced the defect areas (Figure 2.14 left), something that was also discussed in [28]. Conversely, increasing the tow width while keeping the course width constant (thus decreasing the number of tows) decreased the total defect area (Figure 2.14 right) but increased deviations from the designed fiber path and reduced the number of manufacturable designs. The results indicated that a complete gap strategy lowered the in-plane stiffness and buckling load by up to 14.5% and 12% respectively, while a complete overlap strategy enhanced only the buckling load by as much as 19%.

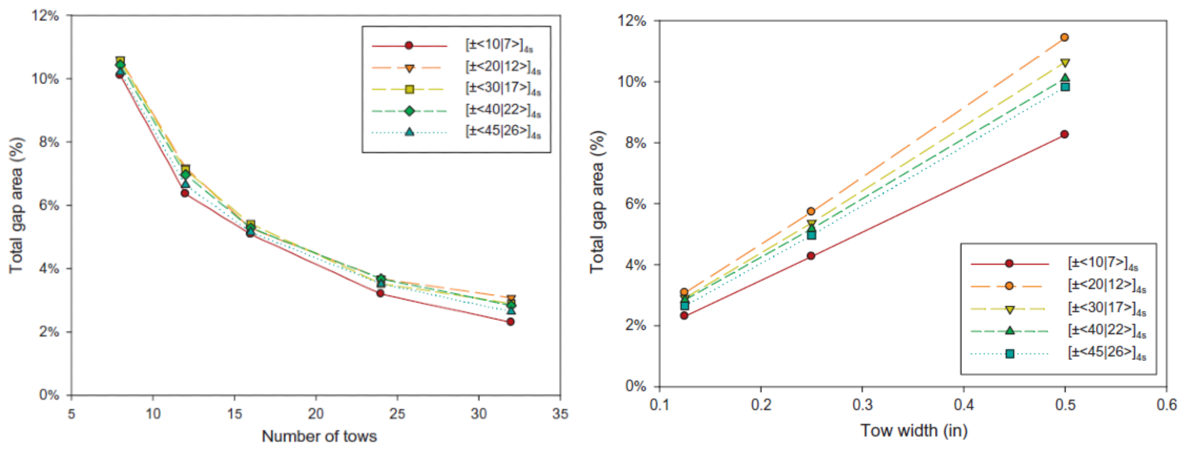

Figure 2.14: Left: Effect of number of tows on the gap area percentage (tow width constant at 3.125 mm (1/8 ")). Right: Effect of tow width on the gap area percentage (course width constant at 101.6 mm (4"). Five different laminate layups were examined [37].

Marouene et al. (2016) [38] also examined the impact of tow-drop gaps and overlaps on the buckling behaviour of optimally designed variable-stiffness composite laminates, this time through both experimental and numerical studies. In the experimental phase, panels with constant-curvature fiber paths were manufactured using two strategies: complete overlaps and complete gaps. These panels were tested under uniaxial compression until failure. The aim was to evaluate how each type of defect affects the panels' in-plane stiffness and buckling load. The numerical analysis involved a two-dimensional finite element model built in Abaqus and supplemented with a MATLAB routine to localize gaps and overlaps. Linear and nonlinear buckling analyses were conducted to predict pre-buckling strength and critical buckling loads. The results showed a good correlation between experimental and numerical findings. The study did not conclusively demonstrate a purely negative impact of gaps. For panels with gaps, in terms of effective axial stiffness (or pre-buckling in-plane stiffness), there was a reduction that was limited to 2.6%. However, the same panels showed an increase in buckling load by up to 7%. In contrast, panels with complete overlaps exhibited significantly enhanced performance in both categories, with increases of 40% in axial stiffness and 80% in buckling load. Note that the additional panel mass due to the increased thickness induced by the overlaps was not taken into account, therefore the positive effect of overlaps might be overestimated.

The general trend observed across these studies is that AFP-induced gaps usually result in a reduction in both in-plane stiffness and buckling load, with a notable exception found in [38]. On the other hand, overlaps seem to enhance both these properties. Regarding overlaps, the general trend in their impact can be attributed to the increased local fiber density. Overlaps add material where fiber tows stack, enhancing load-bearing capacity in those areas. This additional material improves stiffness by increasing the effective cross-sectional area for in-plane loads and raises the buckling load by strengthening resistance to compressive instability. In cases like those reported by [35] and [37], the significant improvements in stiffness and buckling load in overlap configurations likely reflect these local material reinforcements.

Gaps, conversely, reduce stiffness and buckling load because they create localized regions with reduced fiber content, diminishing the material's ability to carry loads effectively. This results in lower stiffness and can initiate stress concentrations, which make the laminate more susceptible to early buckling under compressive loads, as observed by [35] and [37]. However, the unexpected finding from [38], where gaps had a minor impact on stiffness but improved buckling load, may be due to redistribution effects; localized gaps could create small stiffness variations that change load paths, occasionally increasing overall buckling capacity. This indicates that the impact of gaps on buckling load could depend on specific defect distributions and load configurations.

The results regarding the impact of AFP-induced defects on in-plane stiffness and buckling load are presented in Table 2.2. As previously, these are results about un-notched panels with non-staggered defects. Again, empty cells on the table mean that the relevant test or defect was not investigated.

Apart from the scientific papers listed and discussed above, a significant influence for the path that

	Max. In-plane Stiffness Difference %		Max. Buckling Load Difference %	
Study	*Gaps*	*Overlaps*	*Gaps*	*Overlaps*
Fayazbakhsh et al. (2013) [35]	-15.1	+11	-12.4	+30.5
Arian Nik et al. (2014) [37]	-14.5	-	-12	+19
Marouene et al. (2016) [38]	-2.6	+40	+7	+80
Mishra et al. (2019) [36]	-1	-	-8.3	-

Table 2.2: Comparison of results from different studies about gaps and overlaps effect on in-plane stiffness and buckling load

this thesis took was the Master's Thesis by László Czél (2024) [39]. This thesis focused on the enhanced characterization of tow-to-tow gaps in fiber steered laminates produced by Automated Fiber Placement (AFP) methods. The research involved both numerical and experimental considerations, with element-level specimens containing tow-to-tow gaps being tensile tested. The study hypothesized that gaps negatively affect off-axis tows (meaning tows that have an orientation different than 0 degrees), leading to strength reductions and localized matrix failures.

As in the present thesis, specimen design was also a key part of Czél's work, involving an iterative process using FEM to simplify geometries and focus on key aspects of the defects. The specimen was designed for tensile testing and featured 8 plies in total (called backing plies) with layup: [0/-15/+15/0/0/+15/-15/0]. Two additional (external) plies were laid down on the front and the back of the specimen, oriented at +45° and -45° respectively. These plies only covered a portion of the whole specimen surface (the so-called gauge area) and were composed of unidirectional tows with gaps in between them. The gap size was set to be 3 mm. The specimen design is presented in Figure 2.15 below. Initial FEM results showed that the external plies (containing gaps) exhibited matrix failure at locations where gaps exist in the opposite ply, resembling a grid (Figure 2.16).

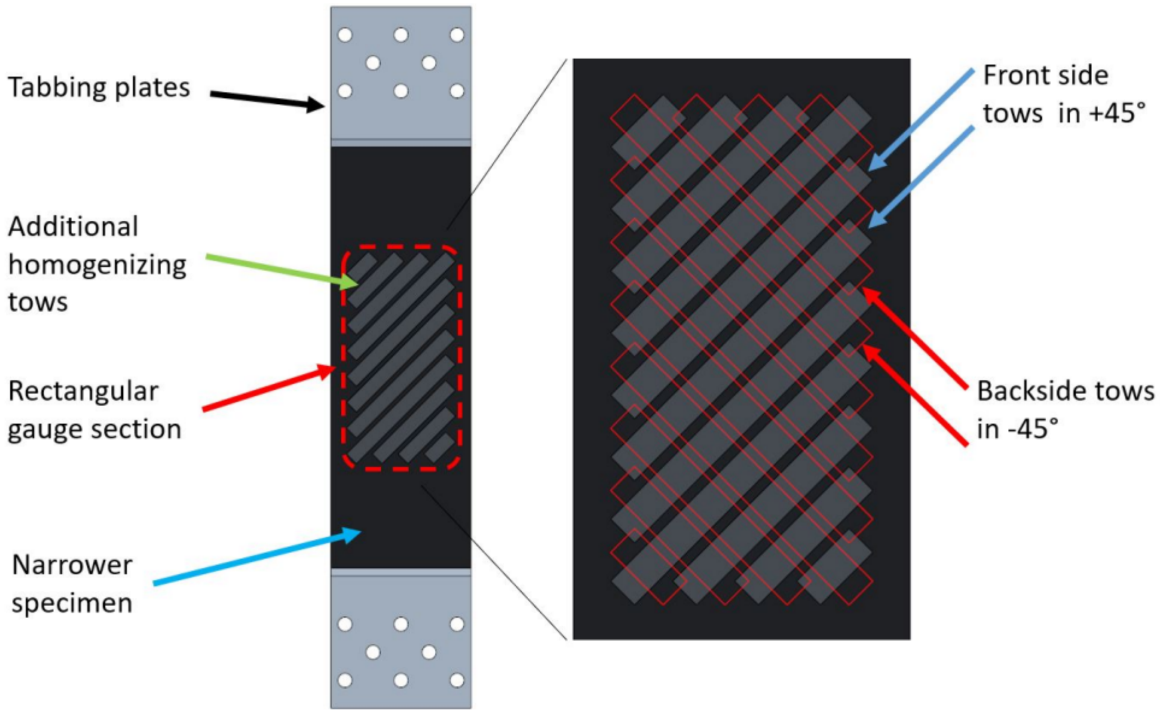

Figure 2.15: Specimen design in Czél (2024) [39]

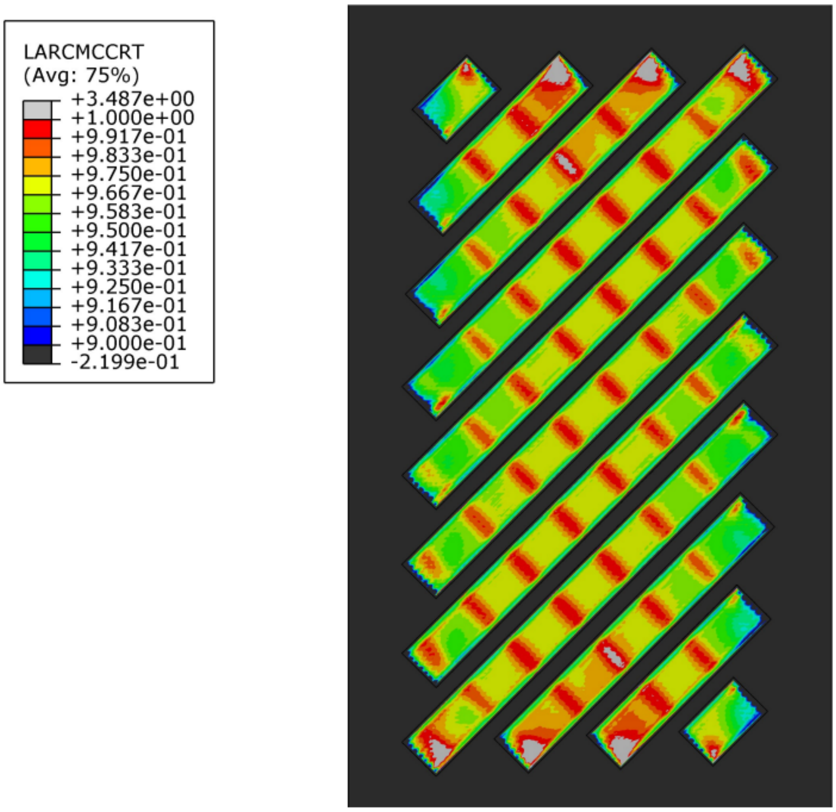

Figure 2.16: Matrix failure of front ply containing tow-to-tow gaps. Failure is observed at backside gap locations [39]

Except for the simulation process, manufacturing and tensile experiments of the specimen were carried out. The manufacturing process combined hand lamination and AFP. The experimental results revealed several key findings about the effects of tow-to-tow gaps in composite laminates. Digital Image Correlation (DIC) demonstrated that gaps caused localized strain concentration, with deformation peaks forming either at the gaps themselves or in regions bounded by gaps, something that in general agrees with the rest of the literature discussed so far. Microscopical analysis highlighted void formation and confirmed ply deformation (waviness) near the gaps. While matrix cracking and microcracks were observed in the specimens, they did not consistently align with the anticipated failure locations predicted by simulations. As can be observed in Figure 2.17, the peaks in shear strains that are visible in the FE model's front tows (left), and which are located in gap areas of the back tows, are absent in the tested specimen (right). This is most probably due to the absence of fiber waviness in the FE models. However, the results confirmed that gaps influence laminate behaviour by introducing local stress concentrations, which can weaken the structure.

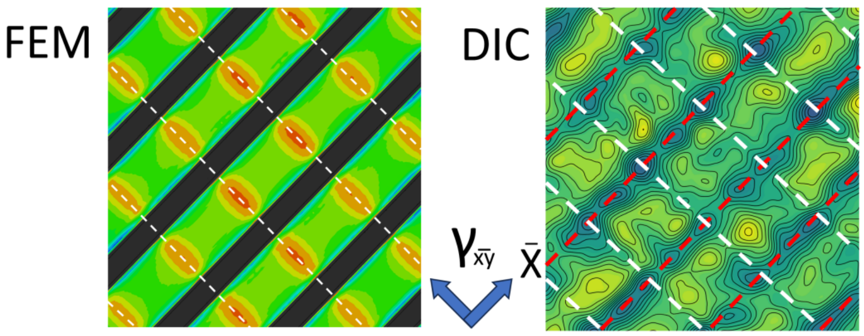

Figure 2.17: Comparison of shear strains between FEM and experiment [39]

2.3.3. Other relevant considerations

In addition to their effects on mechanical strength, in-plane stiffness, and buckling load of composite structures, the literature review also highlighted some other important aspects of the behaviour of AFP-induced manufacturing defects.

Staggering

First and foremost, in some of the aforementioned studies, the impact of staggering was also investigated. As mentioned before, staggering refers to the intentional offsetting of plies with the same orientation relative to each other. This method is used to prevent the alignment of gaps and overlaps across adjacent plies in the same plane, and as will be discussed in the next paragraphs, it can mitigate the negative impact of these manufacturing defects up to a certain extent.

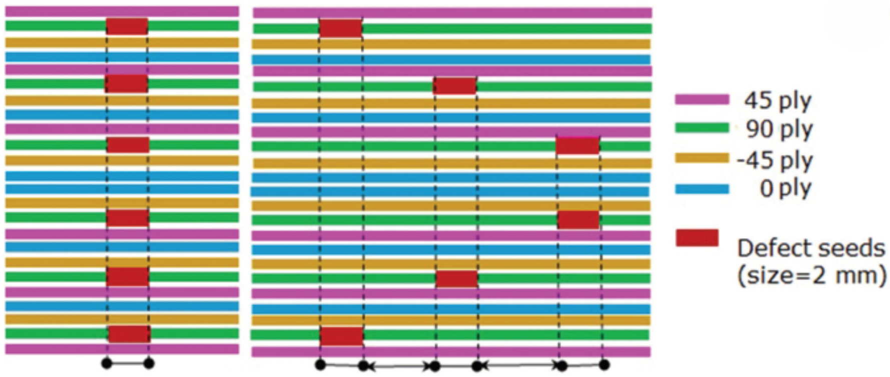

Figure 2.18: Non-staggered (left) and staggered (right) gap distribution [16]

More specifically, an important conclusion from the study of Blom et al. (2009) [28] was that staggering the plies positively influenced strength by inducing a better stress distribution and thus delaying final failure. In 2014, Falcó et al. [25] also investigated specimens with staggered gaps, finding out that applying staggering reduced the negative impact of the gaps, with un-notched specimens showing a strength decrease of 9% (while the respective specimens with non-staggered gaps reduced the strength by 22% - Table 2.1). The results also indicated that the configuration with 0% gap coverage (thus full overlaps in the context of this study) and ply staggering effectively minimized the impact of defects, improving load transfer, delaying damage propagation compared to other configurations and proving the beneficial properties of staggering. Moreover, Li et al (2015) [16] concluded as well that defects without staggering cause more significant strength reductions than staggered defects, although the authors did not provide relevant values for the difference. Last but not least, Woigk et al. (2018) [32] proved that their ”Staggered Gaps” configuration (see above for definitions in this study) resulted in a strength change of -0.2% in tension compared to -1.3% for non-staggered gaps. Two important comments should be made here however. First of all, the minimal change in strength reduction could indeed be a sign of the beneficial properties of staggering, but could also be a sign of experimental scatter or statistical error. Variability in specimen preparation or measurement methods might contribute to the observed results. Moreover, the stagger distance was chosen to be 2 mm, which is equal to the gap size, meaning each gap begins at the end of the adjacent gap (at the ply above or below). This quite small stagger distance contrasts with other studies. For example, Blom et al. (2009) [28] used stagger distances of 19 mm or 38 mm, depending on the number of repeating plies in a laminate with a 76.2 mm course width. Similarly, Li et al. (2015) [16] used a 10 mm stagger distance with a 2 mm gap size. The minimal stagger distance used by Woigk et al. raises questions about its effectiveness compared to more widely spaced gaps, and could also be the main reason for such a small effect on strength difference with non-staggered specimens.

Gap-filling mechanisms

To better understand the effects of Automated Fiber Placement (AFP)-induced manufacturing defects, it is essential to consider changes occurring during the curing process, particularly regarding gaps. Prior to curing, gaps—either between tows or due to tow-drops—are essentially voids. However, during curing, elevated temperature and pressure alter these regions, transforming them into resin-rich areas. The forces driving these changes, and the resulting impact on laminate properties, will be discussed in detail below.

Niknafs Kermani et al. (2021) [40] explored the mechanisms of gap filling during the Automated Tape Placement (ATP) process for thin ply composites. Automated Tape Placement, or Automated Tape Laying (ATL) is a process similar to AFP, only using wider prepreg tapes (width range from 76.2 mm to 304.8 mm) [41]. The research introduced a numerical model to simulate the gap-filling process by coupling the squeeze flow behaviour of resin within the tapes with the deformation of the top layers into the gaps (Figure 2.19). It should be mentioned that a third mechanism also takes place during the gap-filling process, namely resin percolation. During this phenomenon, the resin within the fiber bed permeates into the gap, as opposed to resin squeeze flow, in which the resin and the fibers move as one and fill (part of) the gap. However, for simplicity's sake, resin percolation was not taken into account in this study. The model's predictions were validated against experimental observations using micrographs of the manufactured samples. Key findings included that lower viscosity resins filled gaps more quickly, reducing the time for cross-ply deformation, while higher viscosity resins slowed the squeeze flow, making deformation more significant. The stiffness of the cross-ply layer also influenced the extent of deformation into the gaps, affecting the fiber waviness and the overall quality of the composite. The model accurately predicted the deformation behaviour of the cross-ply into the gaps, although discrepancies in thickness predictions indicated the need to account for resin percolation in future models.

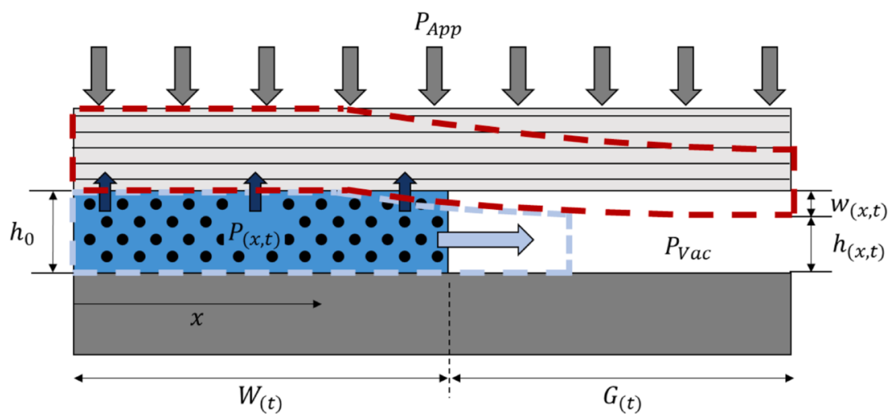

Figure 2.19: Schematic view of gap filling mechanisms (squeeze resin flow and ply deformation into the gap) [40]

As a follow-up on their previous work, the same group of researchers led by Simacek (2022) [42] investigated the role of resin percolation in gap filling mechanisms during the ATL process for thin ply thermosetting composites. The study focused on understanding how gaps between adjacent tapes, which can introduce defects such as porosity and fiber waviness, are filled during the manufacturing process. The research extended existing models that primarily considered the squeeze flow of fiber and resin suspension by introducing resin percolation as a significant secondary mechanism (Figure 2.20). This comprehensive model integrates both squeeze flow and resin percolation to simulate the gap-filling process more accurately. Experiments using thin prepreg tapes provided visual evidence of resin-rich zones, validating the model's predictions. Numerical simulations and parametric studies were conducted to assess the impact of various parameters on gap filling, highlighting the importance of resin percolation, especially with thinner tapes. The findings demonstrated that resin percolation is a critical mechanism in gap filling, influencing the formation of resin-rich zones and the overall quality of the composite part. Especially in the case of tow-drop gaps, considering their geometry one can easily understand the high importance of resin percolation. Because the tows are not parallel, in the case of squeeze flow, the fibers encounter the boundary of the adjacent tow, which does not allow them to "squeeze" into the gap effectively, facilitating the activation of pure resin percolation (Figure 2.2).

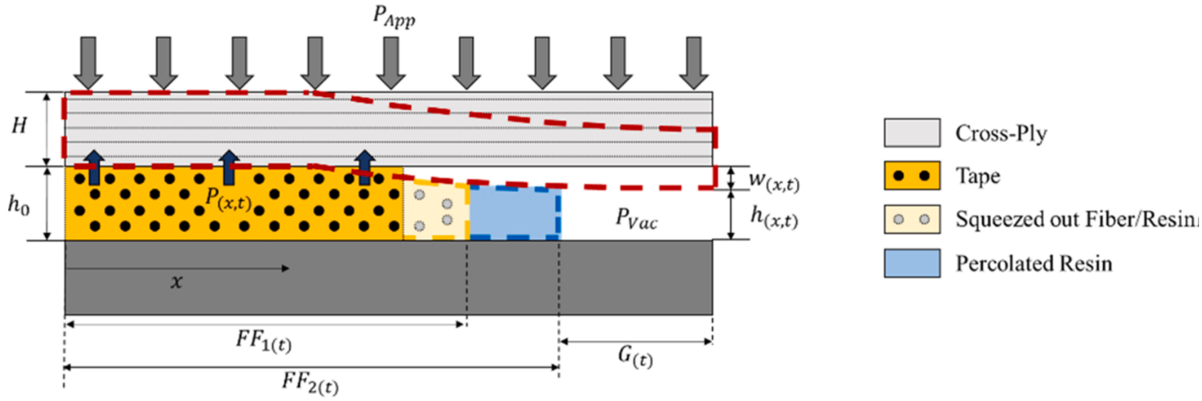

Figure 2.20: Schematic view of gap filling mechanisms (including resin percolation) [42]

2.4. Research Questions

Considering the existing body of research in this domain, it is evident that gaps detrimentally affect the strength and mechanical properties of composite laminates. Conversely, the impact of overlaps remains inconclusively evaluated, with some studies indicating a positive effect and others a negative one. It is also well-established that the staggering of plies provides beneficial properties, mitigating the adverse effects of gaps. Given that analyzing both types of defects —gaps and overlaps— would be a quite tedious and time-consuming task, this thesis will concentrate exclusively on the study of gaps. This focus is justified by the more predictable behaviour of gaps and their generally more severe impact compared to overlaps. Regarding the types of gaps to be investigated, the decision has been made to focus on tow-drop gaps rather than tow-to-tow gaps. This decision is primarily based on the fact that numerous studies have already extensively addressed the impact of tow-to-tow gaps [24], [16], [32], [27], [33], [35]. In contrast, tow-drop gaps present a few research gaps that need further investigation.

More specifically, although most publicly available studies examine the impact of tow-drop gaps in considerable detail, in all of them ([28], [24], [25], [16], [31], [32], [27], [35], [37], [38], [36]), free-edge effects are present, as the defects run all the way to the edges of the specimens. This is something not very representative of reality, as usually, defects (such as gaps and overlaps) are contained in the interior of wider laminates. These free-edge effects influence failure behaviour primarily by inducing delaminations at the laminate's edge. This phenomenon must be avoided to obtain a clearer understanding of the deformed state of the laminate and, consequently, the actual impact of the tow-drop gaps. In fact, Falcó et al. stated in their 2017 study (which is one of the main influences of the present thesis): *"the physical/virtual coupon testing approach show limitations in the analysis of the influence of the tow-drops on laminate response, despite the fact that the coupons are representative of a subdomain of a large variable-stiffness plate. This is because the specimens free-edges also influence the damage mechanisms, mainly delamination, and the influence of the defects is not isolated completely. Hence, future analyses on VSP should take into account the occurrence of delamination without the influence of outside conditions."* (Falcó et al. (2017) [31], p.70).

In addition, several of the research works presented above do not take into account the deformed internal geometry of the laminate after curing, when creating their finite element models. As aforementioned by Niknafs Kermani et al. (2021) [40] and Simacek et al. (2022) [42], the cured architecture of the laminate is governed by ply bending and resin squeezing into gaps. These effects (and especially the one of ply bending) are often neglected in literature and therefore, considering the deformed waviness would produce more accurate results. To quote Falcó et al. once more: *"More realistic physical and virtual coupons, including curved fibres, should be designed taking into account the out-of-plane waviness and the ply thickness variation..."* (Falcó et al (2017 [31], p.70). This was also a major outcome in the Master's Thesis of Laszlo Czél (2024) [39], which greatly influenced this work.

Hence, the two main research gaps that will be addressed in this thesis are:

1. Investigating the impact of tow-drop gaps without the interference of free-edge effects
2. Including the deformed geometry (such as tow bending/waviness) into the FE models that will be used to validate future experimental results.

As aforementioned, due to the collaboration with Airborne Aerospace, the work done in this thesis should align up to a certain point with the interests of the company. Airborne Aerospace is a leader in the industry of manufacturing composite structures for aerospace applications, often using AFP in their manufacturing methods. Laminates produced with AFP often contain gaps and overlaps, which is why the company is keen on the better understanding of the implications of such defects. The inspiration about the topic of this thesis came from a composite structure that Airborne has already produced and is known to exhibit tow-drop gaps. The structure in question is a pressure vessel, featuring a cylindrical body and two dome-shaped end caps, predominantly manufactured using AFP. While the cylindrical section of the pressure vessel is well-characterized and extensively analyzed, the dome-shaped areas pose some uncertainties, particularly regarding the presence of defects such as gaps and overlaps in the fiber layup. These regions are of significant interest, as they represent a critical area where manufacturing imperfections, including tow-drop gaps, are more likely to occur and could potentially compromise structural integrity.

Therefore, developing the right research question (and subquestions) is essential to effectively address the tow-drop gaps and their impact, particularly in composite pressure vessel applications. Taking everything into account, the main research question and subquestions of this thesis are the following:

Main Research Question

How do gaps resulting from tow drops during the Automated Fiber Placement (AFP) process, and which are isolated from free-edge effects, affect the tensile strength (in terms of First-Ply Failure) of a composite laminate?

Subquestions:

1. What is a suitable specimen design, in terms of specimen geometry and layup, gap geometry and size, gap configuration, method of gap introduction, and type of loading, to accurately evaluate the effects of tow-drop gaps in the composite laminate, relevant to pressure vessel applications?
2. How does the implementation of the cured geometry of the laminate (including fiber waviness and resin-rich areas) affect the results about tensile strength, as well as the failure modes predicted initially?

The studies presented and discussed in this chapter featured gaps embedded in laminates intended for uniaxial testing (usually tensile, but sometimes also compressive, such as in the case of Blom et al. (2009) [28]). However, it will be shown in the next chapters (especially in Chapters 3 and 4), that in order to answer these research (sub)questions accurately, a uniaxial tensile specimen might not suffice, and instead a specimen loaded in biaxial tension might be needed. A standard uniaxial tensile specimen could of course still be used as an alternative. More details about the reasoning behind this will be presented later on.

This distinction in loading types raises the question of how the laminate's failure behaviour might differ between these two loading conditions. Studies have shown that the strength and deformation characteristics of composite laminates under biaxial loads can differ from those under uniaxial loading. For instance, the study of Zhu et al. (2020) [43] has shown that biaxial loading can lead to earlier onset of damage and different progression patterns compared to uniaxial loading. Also, the research of Hinton et al. (1996) [44] on filament-wound composite tubes under biaxial loading conditions indicated that traditional failure criteria may not adequately predict failure in biaxial stress states. Lastly, the paper of Welsh et al. (2007) [45] on quasi-isotropic carbon composite laminates also showed that biaxial loading can lead to complex stress distributions, resulting in failure modes that differ significantly from those observed under uniaxial tension.

To sum up, this chapter reviewed established knowledge and identified research gaps that this study aims to address. The following chapters will explore the research questions in detail and provide answers.

3 Representative Specimen Requirements

In order to address the research questions with the highest degree of accuracy, it is essential to design and analyze a specimen that contains well-characterized defects. This specimen will serve as the primary vehicle for evaluating the true impact of these defects on the performance of composite structures. In the context of this thesis, as aforementioned, the defects have the form of tow-drop gaps. The precision and reliability of the specimen design are critical to ensuring that the results obtained from testing are both accurate and predictive of real-world behaviour. Apart from that, since this thesis was conducted in partnership with Airborne Aerospace, an essential aspect is to eventually come up with a specimen design that is representative (as much as possible) of a real-life case of a composite structure containing tow-drop gaps, in order to correlate the theoretical level of academic research to a practical application that is of interest to the company.

As mentioned in Chapter 2, the representativeness of the specimen design is derived from its correlation to a demonstrator of a pressure vessel that was manufactured by Airborne. The specimen design should balance between being highly representative of the dome areas of the pressure vessel, while also being similar to well-established testing specimens. This approach allows the research to take advantage of proven experimental methods, procedures and known material behaviours. In order to achieve the above, the specimen should meet certain requirements, divided in the following categories:

1. Gaps geometry and size
2. Load cases
3. Specimen layup

In the present chapter, each of the above requirements will be analyzed and justified. Due to confidentiality, details about the pressure vessel manufactured by Airborne cannot be disclosed. However the following case study deals with a very similar topic, and is thus presented in order to give the reader a better understanding of the details of AFP-manufactured composite pressure vessels and their induced defects.

3.1. Case study: AFP-manufactured pressure vessel containing defects

The study of Oromiehie et al. (2024) [46] explored the use of Automated Fiber Placement (AFP) to manufacture a composite overwrapped pressure vessel (COPV) (presented in Figure 3.1), aiming to improve fuel efficiency in hydrogen storage applications. AFP was used for the construction of both the inner composite liner and outer overwrap, which was used to also fully cover the internal aluminium domes. The material used for the liner and overwrap was unidirectional carbon/epoxy prepreg, and a total of 75 plies were laid in optimized orientations to resist axial and hoop stresses. AFP applied heat and pressure to the fibers through a compaction roller and hot gas torch, maintaining a temperature of 200°C and a consolidation force of 180 N. The resulting laminate structure achieved 17.74% weight reduction compared to traditional metallic liners, proving the benefits of using composite materials in such applications.

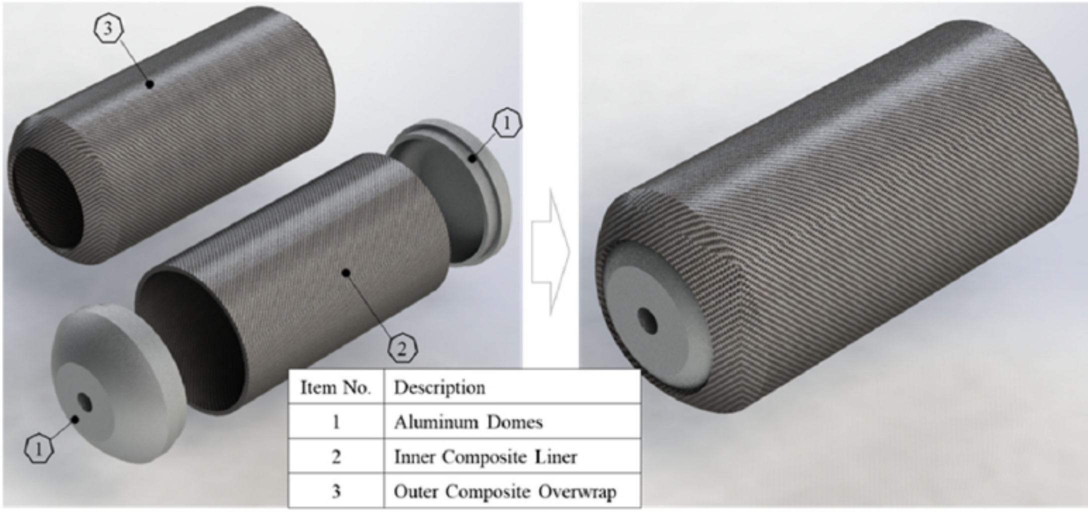

Figure 3.1: Concept design of a composite pressure vessel using AFP [46]

However, manufacturing complex geometries like the COPV's dome areas presented challenges. The AFP process struggled with tow steering and maintaining fiber orientation on these highly curved surfaces. While fiber paths with fixed orientations (such as ±30°, ±45°, ±60° or 90°) were laid down more or less without problems in the cylindrical section of the vessel, deviations between the nominal and actual fiber angles arose as the AFP machine head moved into the dome sections, where double curvature becomes a factor. To address this, the fiber tows needed to be steered along the path so that the initial set fiber angle remains constant throughout each course, compensating for deviations in the dome area. Nonetheless, the decreasing radius in the dome area of the tank will generally lead to ply thickness build-up if a constant and continuous course is maintained. To prevent this, the fiber tows were stopped and restarted, leading to defects such as gaps and overlaps. The dome regions exhibited unavoidable stress risers due to these AFP-induced defects, which could potentially be the failure points under the high-pressure conditions in the tank, proving once more the detrimental effect of these defects.

It is clear that in the context of the present thesis, the gaps contained in the specimens to be designed must relate to the gaps found in structures such as the pressure vessel discussed above. A closer look at the geometry and size of these defects is thus deemed necessary. In Figure 3.3, a zoomed-in view of the gaps found in the dome areas of the pressure vessel is presented. As can be seen, the gaps (which resulted from tow-dropping - marked in red) have the characteristic triangular shape which has been discussed so far. The authors of this paper do not provide specific values for the size (width and length) of the gaps, but it can be observed in Figure 3.3 that at their base, the gaps have a width equal to one tow width. The tow width of the material used in this study was 6.35 mm, therefore following the same reasoning as Falcó et al. (2014) [25], it can be assumed that the gap length is around 30 mm.

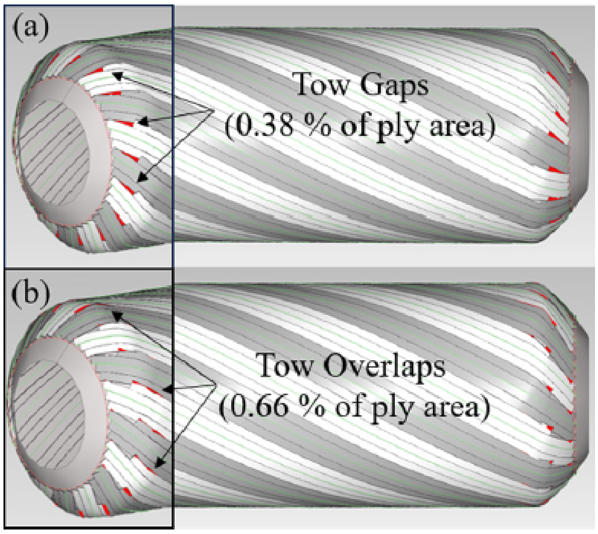

Figure 3.2: Gaps and overlaps distribution in dome areas of the pressure vessel (30° ply) [46]

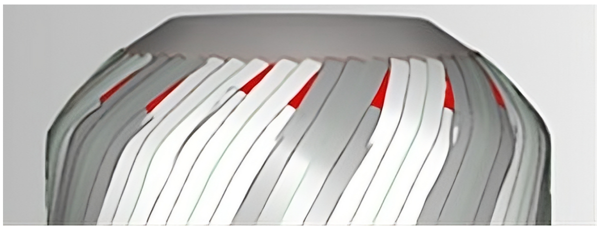

Figure 3.3: Gaps in dome area (zoomed in) [46]

3.2. Requirements

In the next section, the requirements that the specimen must meet in order to be as representative as possible of the domes of an AFP-produced pressure vessel are discussed.

3.2.1. Gaps geometry and size

As discussed in Section 3.1, to accurately assess the impact of these tow-drop gaps on the mechanical strength of the specimen, it is essential to design a specimen that includes gaps that closely mimic real-world conditions. These gaps must not only be realistic in their geometry and size but also in the way they are introduced during the manufacturing process. Given the objective of accurately replicating real-life defects, it is crucial that the gaps in the specimen reflect the characteristic triangular-like shape of tow-drop gaps typically induced by AFP. This triangular geometry arises due to the nature of the AFP process, where the discontinuation of fiber tows in certain areas creates a gap that tapers off, forming a distinct, wedge-like shape. This gap geometry holds for both curved surfaces (as the one found in the dome area of pressure vessels - Figure 3.3) and flat laminates (as the one seen for example in the study of Blom et al. (2009) [28] - Figure 2.9). Replicating this specific geometry in the specimen is essential for ensuring that the mechanical behaviour observed during testing accurately mirrors that of actual AFP-manufactured components.

Furthermore, the dimensions of these gaps — both in terms of width and length — should (as closely as possible) match those found in real composite structures. The size of the gaps directly influences how stress is distributed within the material, as larger gaps may lead to more pronounced stress concentrations, which can significantly affect the strength and failure mechanisms of the structure. Designing a specimen with unreasonably large or small gaps could lead to inaccurate results and conclusions.

Regarding the gaps width, it is reasonable to assume that the base of each gap should be equal to the full width of a single tow. This assumption is based on the nature of the AFP process, where a tow is dropped, creating a gap that spans the width of the tow. Since the tow-drop is typically initiated at the base of the gap, the width at this point should correspond to the actual width of the tow, ensuring that the defect is as realistic as possible (refer to figure of tow-drop gaps). Of course, a tow-drop gap with a triangular shape means that the gap width is not constant, but is decreasing along its length.

Concerning the gaps length, it mostly depends on the gaps' base width (therefore the tow width) and the angle between the two tows that create the gap (called discontinuity angle). Falcó et al (2014) [25] has stated that a discontinuity angle of 12° is generally a worst-case scenario for the tow-angle mismatch between tows, therefore following simple trigonometry, this would result in a gap length of 29.9 mm. This is derived from the assumption that the gap has a shape of a right triangle, with a 90° angle between the its base and its height. Of course, in the research of Falcó et al (2014) [25], fiber steering was not used and instead straight tows were placed next to each other, being cut at the boundaries of the adjacent tow. In reality, the discontinuity angle would not be created by a discrete step, but rather a continuous increase in angle, as described in Blom et al. (2009) [28]. The length of 29.9 (or 30 mm for simplicity) mm can be regarded as the lowest limit for the gap length, as with a smaller discontinuity angle between the tows (which can often be the case), the gap length increases. For example, for an angle of 6°, the gap length becomes double, at around 60 mm. If we assume a bottom limit for the discontinuity angle at 5°, the top limit for the gap length is at around 72.5 mm. This assumption comes from the minimum steering radius achievable in fiber steering for prepregs with a tow width of 1/4" (6.35 mm), which is usually 400 mm [39]. Therefore, a valid range of lengths for the gaps in this thesis is between 30 mm and 72.5 mm.

3.2.2. Load cases

As previously mentioned, the ultimate goal of designing a representative specimen is to perform mechanical testing on it, after manufacturing, to validate any simulations performed regarding the impact of tow-drop gaps on its strength and failure mechanisms. Of course, the main question here is: What would be the most suitable test for this kind of specimen? The most obvious answer to this question would be performing a uniaxial tension test, a widely accepted and standard mechanical test, which is used to assess material strength. This testing method is advantageous due to its straightforward manufacturing and execution processes, as well as the availability of appropriate testing machines within the DASML (Delft Aerospace Structures & Materials Laboratory). Uniaxial tension would provide reliable data on the tensile strength and failure behaviour of the composite specimen in question, making it a suitable choice for initial assessments. The maximum loading capability of the mechanical testing machine in the DASML is 250 kN, therefore the specimen should be designed to have a failure load (quite) lower than this value.

However, to have a case that is as representative as possible of the dome areas of the pressure vessel presented above, it is important to consider the actual load case that such a structure experiences. To give a definition of pressure vessels, they typically take the shape of spheres, cylinders, cones, ellipsoids, tori, or combinations of these geometries. When the thickness of the vessel is small in relation to its other dimensions (with the ratio of radius to thickness, R/t, greater than or equal to 10), these vessels are classified as membranes, and the stresses generated from the pressure are referred to as membrane stresses. These stresses are characterized as average tension (or compression) stresses, which are assumed to be uniform across the vessel wall and act tangentially to its surface. In the case of internal pressure, the stress state in the pressure vessel is triaxial, defined by three principal stresses. More specifically, for the main body of a pressure vessel, which is usually in the shape of a cylinder, the three principal stresses are as presented below [47], [48]: (Figure 3.4):

- σ_L : longitudinal stress
- σ_H : circumferential (or hoop) stress
- σ_r : radial stress

Additionally, there may be bending and shear stresses present. The radial stress is a direct stress resulting from the pressure exerted on the wall, producing a compressive stress equal to the pressure on the surface it acts upon. In thin-walled vessels, this radial stress is negligible compared to the circumferential and longitudinal stresses, and is therefore often disregarded in analysis [47].

Apart from the cylindrical section of pressure vessels, the same stress state holds for the dome areas of the structure (which are of especial interest in the context of this thesis). As can be seen in Figure

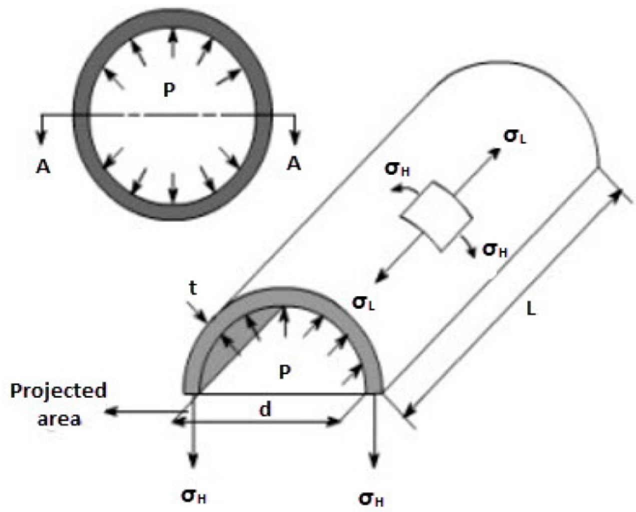

Figure 3.4: Stresses acting on cylindrical section of pressure vessel (citation)

3.5, if we closely examine a single, isolated element of the dome area, both the longitudinal stress (in this figure denoted by σ_θ) and the hoop stress (denoted by σ_ϕ) are present. The only difference lies in the double-curved geometry of the dome area, as opposed to the single-curved one of the cylindrical body. Consequently, it can be concluded that the stress state of an element in the skin of the pressure vessel (as a result of the internal pressure that is exerted on it) is tension in two perpendicular directions (namely biaxial tension). Therefore, it is reasonable to assume that the most representative case for the dome area of a pressure vessel containing gaps would be a flat specimen loaded in biaxial tension.

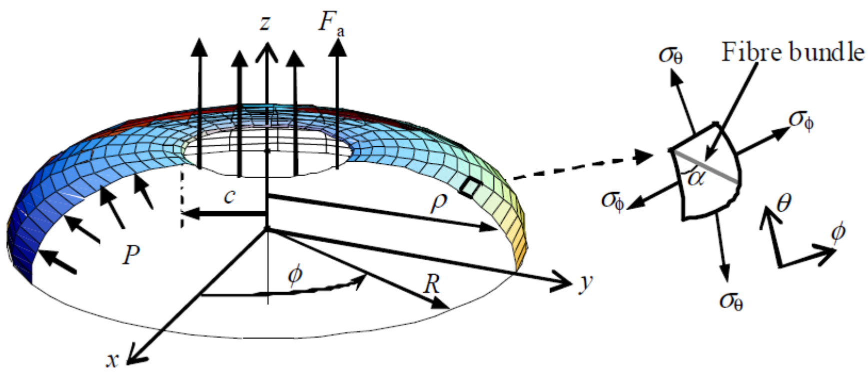

Figure 3.5: Pressure vessel dome area stress state [49]

On a mathematical level, in general, the equations that describe the longitudinal (σ_L) and hoop (σ_H) stresses on a cylindrical thin wall are the following [50]:

$$\sigma_L = \frac{P \cdot r}{2t} \tag{3.1}$$

$$\sigma_H = \frac{P \cdot r}{t} \tag{3.2}$$

,where P is the internal pressure, r is the cylinder radius and t is the wall thickness.

However, as aforementioned, the load case for the specimen should accurately represent the loading conditions on the dome area of a pressure vessel, which is typically spherical, ellipsoidal, or toroidal in shape. In the case of a spherical dome, the longitudinal stress is defined by the same equation as for the cylindrical wall. However, the hoop stress is twice that of the cylindrical wall, resulting in the hoop stress being equal to the longitudinal stress. Thus, it can be stated that for spherical domes:

$$\sigma_L = \sigma_H = \frac{P \cdot r}{2t} \tag{3.3}$$

Therefore, the stress state for a spherical dome section can be translated into a flat specimen, loaded in biaxial tension, with a loading ratio of 1:1, meaning that the loading in both (perpendicular) directions will be equal. An example of the biaxial tensile testing fixture (with equal loading in x- and y-axes), along with the cruciform-shaped specimen to be tested on it are presented in Figure 3.6.

Note that for non-spherical domes, the stress state is more complex and the longitudinal and hoop stresses are not necessarily equal. This means that in order to cover all possible cases, the biaxial tension test fixture should have the capability of adjusting the loading ratio to other values apart from 1:1. More specifically, as is presented in the paper of Koussios (2009) [49], for a zero in-plane shear stress condition the two primary stress components in the dome area of a CFRP pressure vessel are related with the following ratio:

$$\frac{\sigma_\phi}{\sigma_\theta} = \frac{\sin^2\alpha + k_e \cos^2\alpha}{\cos^2\alpha + k_e \sin^2\alpha} \tag{3.4}$$

where α is the winding angle of the fibers (the angle between the fiber direction and the longitudinal axis of the dome), and k_e is called the anisotropy parameter, which represents the relative contribution of the material's anisotropic properties to the stress distribution in the structure. In general, the winding angle ranges between 0° and 90°, and the anisotropy parameter between 0 and 1. A value of 1 for k_e denotes an isotropic material. Hence, it is obvious that the ratio between the longitudinal and hoop stress is influenced by the type of CFRP material (k_e) and the orientation of each ply (α). For a typical value of k_e = 0.2 (which reflects the high anisotropy of CFPR) and a ply oriented at α = 45°, the stress ratio becomes:

$$\frac{\sigma_\phi}{\sigma_\theta} = \frac{\sin^2\alpha + k_e \cos^2\alpha}{\cos^2\alpha + k_e \sin^2\alpha} = 1$$

For a winding angle of α = 30°, a ratio of

$$\frac{\sigma_\phi}{\sigma_\theta} = 0.5$$

occurs, while for α = 60°, the ratio becomes equal to 2. Therefore, for lower winding angles, the longitudinal stress is higher than the hoop stress, with the situation being reverse for higher winding angles (larger than 45°).

In summary, to accurately characterize the impact of tow-drop gaps on the dome areas of pressure vessels, it is essential to design a specimen that can be mechanically tested under conditions that closely mimic the actual loading these structures encounter. The most effective approach for this purpose would be to utilize biaxial tension as the load case, particularly with the option to apply varying magnitudes of loading in the two perpendicular directions. However, if implementing biaxial tension proves too complex, a uniaxial tension test can still serve as a valuable preliminary step towards understanding the effects of these manufacturing defects.

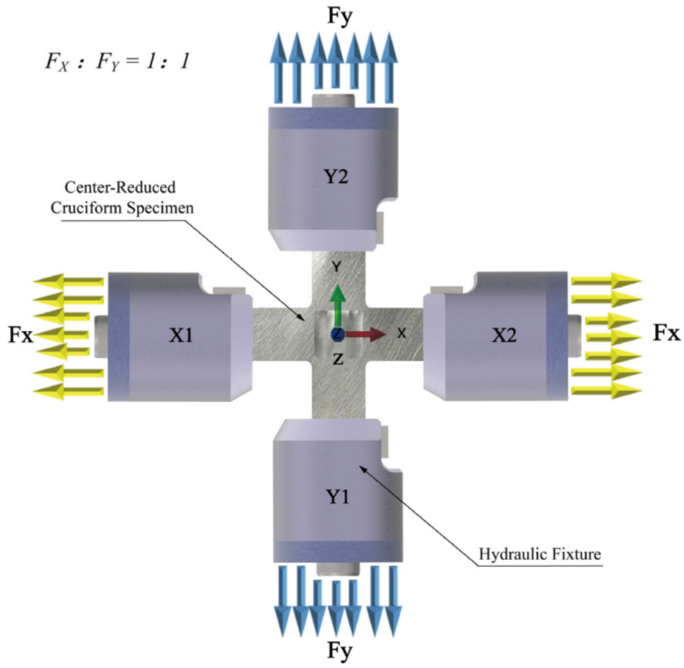

Figure 3.6: Example of a biaxial tension test fixture [51]

3.2.3. Specimen layup

A fundamental consideration in designing the specimen for this thesis is the layup configuration, which includes both the total thickness - determined by the number of plies - and the specific orientation of each ply. In practical applications, the total thickness of CFRP pressure vessel dome sections can extend up to 10 mm, or even more [46]. However, replicating this thickness for the purposes of this thesis would be impractical. A specimen this thick would be more difficult to handle and would require quite higher loads during testing, which could possibly exceed the capacity of the available testing equipment in the lab. Moreover, a thicker specimen would require a significantly larger quantity of material for manufacturing, which could prove to be both prohibitively expensive and logistically unfeasible within the scope of this thesis. The cost of sourcing sufficient material to produce a full-thickness specimen that meets industry standards would far exceed the project's budget and resources. Additionally, manufacturing such a specimen at full thickness would pose practical challenges, further complicating the experimental process. Therefore, it would be unreasonable to attempt to fabricate a specimen of industry-level thickness, given the constraints of this research. As a result, the total thickness for the specimen was deliberately reduced to ensure that it can be both manufactured and tested under the available conditions. Moreover, ISO 527-5 [52], which is a specific standard describing the test conditions for tensile testing of fiber-reinforced plastics, features two different specimen types with thicknesses of 1 and 2 mm. Taking all this into account, the thickness of the specimen was decided to be set to 1 mm (or as close to this value as possible, depending also on ply thickness).

Another significant aspect of the specimen design is to have a layup that is balanced and symmetric. To clarify, first of all, a balanced layup means that for every +θ ply there is a corresponding -θ ply somewhere in the stacking sequence. Additionally, a symmetric laminate features a symmetric stacking sequence with respect to the mid-plane of the laminate [21]. For instance, the laminate with layup [0/+45/-45/0/-45/+45/0] is symmetric and balanced. The question is: why is a balanced and symmetric laminate needed? To answer this, it is essential to refer to Classical Lamination Theory (CLT) and more specifically to the ABD matrix, which is the matrix that connects the loads (forces and moments) applied to a composite laminate to its resultant strains and curvatures:

$$
\begin{bmatrix} N_x \\ N_y \\ N_{xy} \\ M_x \\ M_y \\ M_{xy} \end{bmatrix} = \begin{bmatrix} A_{11} & A_{12} & A_{16} & B_{11} & B_{12} & B_{16} \\ A_{12} & A_{22} & A_{26} & B_{12} & B_{22} & B_{26} \\ A_{16} & A_{26} & A_{66} & B_{16} & B_{26} & B_{66} \\ B_{11} & B_{12} & B_{16} & D_{11} & D_{12} & D_{16} \\ B_{12} & B_{22} & B_{26} & D_{12} & D_{22} & D_{26} \\ B_{16} & B_{26} & B_{66} & D_{16} & D_{26} & D_{66} \end{bmatrix} \begin{bmatrix} \varepsilon_x \\ \varepsilon_y \\ \gamma_{xy} \\ \kappa_x \\ \kappa_y \\ \kappa_{xy} \end{bmatrix} \tag{3.5}
$$

The ABD matrix can be calculated for a laminate with a known layup, therefore from the above relation, the strains (and curvatures) of the laminate can be easily calculated (with a simple inverse of the ABD matrix), as the loads of the test will be known. The ABD matrix combines three sub-matrices - A, B and D - each representing different aspects of the laminate's mechanical response. Specifically:

- The A matrix (extensional stiffness matrix) relates in-plane forces to in-plane strains.
- The B matrix (coupling stiffness matrix) represents coupling between bending and stretching. It relates in-plane forces to curvatures and bending moments to in-plane strains. This coupling occurs in laminates that are unsymmetric with respect to their mid-plane.
- The D matrix (bending stiffness matrix) relates bending moments to curvatures and it captures the laminate's resistance to bending.

For a symmetric laminate, the B matrix is zero, hence bending-stretching coupling is avoided [21]. This is crucial to achieve, since this coupling can lead to bending in the specimen, which complicates the analysis and obscures the pure tensile response. Symmetry about the mid-plane eliminates the B matrix, ensuring that tensile loads result in pure in-plane deformations without unintended bending. Moreover, as can be deduced by Equation 3.5, the elements A_{16} and A_{26} in the ABD matrix couple the shear strain γ_{xy} with the axial forces N_x and N_y respectively. This is also something to be avoided, as having a pure axial in-plane deformation (thus no γ_{xy}) makes it easier to assess the direct impact of the tow-drop gaps on the laminate's tensile strength without introducing secondary shear effects that could affect the stress distribution around the gaps. In addition, any shear stresses that could possibly be present near the gap area, could be attributed to the gaps themselves, allowing for easier conclusions regarding the behaviour of the laminate containing defects. For a balanced laminate it holds that A_{16} = A_{26} = 0, therefore this coupling is indeed avoided [21].

4

Specimen Design

With the specimen design requirements established, as outlined in Chapter 3, the next step was to develop the actual specimen designs. Two primary designs were created: one for the uniaxial tensile testing specimen, and one for the biaxial tensile specimen. However, along the design process, it was revealed that a pure biaxial tensile testing machine was not available, neither in the DASML, nor in any other faculty of TUD. This poses a significant challenge in the research process. The challenge lies in validating the numerical results experimentally, as the biaxial tensile fixture is still at the concept stage and has not yet been manufactured. To address this, another type of biaxial tensile specimen could be used instead. In this setup, the cruciform-shaped specimen would be fixed in one direction (x- axis) and pulled in the other (y-axis). This method, although not purely biaxial, still offers some kind of loading in two perpendicular directions, due to the Poisson effect. Since for composite materials the in-plane Poisson ratio (see below for definition) is usually $\nu_{12} = 0.3$, theoretically the loading ratio that could be feasible with this method could be assumed to be close to 1:3. However, this is something that needs to be evaluated. Note that from here on, the specimen using this setup will be referred to as the semi-biaxial tensile specimen.

The Poisson effect refers to the material's tendency to contract in the direction perpendicular to an applied tensile load (or conversely expand in the direction perpendicular to an applied compressive load), an effect that can be illustrated in Figure 4.1. Mathematically, it is expressed through the Poisson's ratio:

$$\nu = -\frac{\varepsilon_t}{\varepsilon_a} \tag{4.1}$$

, where ε_t is the transverse strain and ε_a is the axial, or longitudinal strain (in the direction of the acting force) [53].

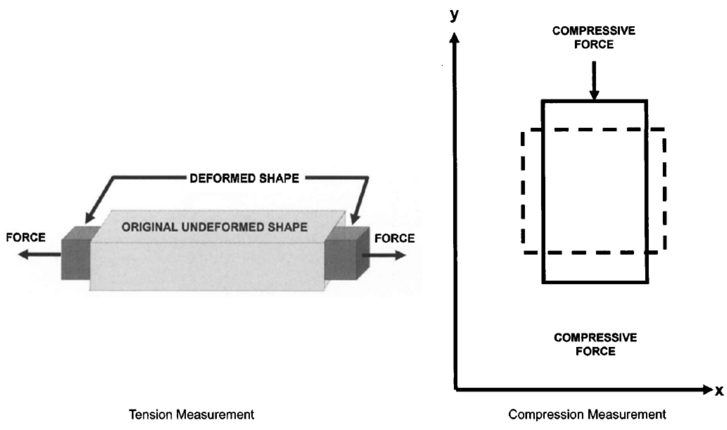

Figure 4.1: Poisson effect in tension and compression [53]

Therefore, in the case of semi-biaxial tensile loading, when the specimen would be pulled along the y- axis, it would attempt to contract along the x- axis. However, because the x- axis is fixed — preventing both translation and rotation — this contraction is restricted, resulting in a reaction force along the x-axis. Although the force generated in this direction will be lower than the applied force in the perpendicular direction, this setup still approximates the different loading ratios observed in internal pressure conditions (see Chapter 3, section 3.2.2 for details). Note that rotation is equally important to be restricted as translation, since if the specimen is free to rotate in one axis but not the other, bending stresses could arise which could affect the failure behaviour. Thus, it is clear that this semi-biaxial approach can provide a feasible method for experimentally evaluating complex stress states, when a fully biaxial fixture is unavailable, and could potentially act as an initial evaluation step.

To distinguish between the biaxial and semi-biaxial tension specimens, another version of the initial biaxial design was created. In terms of total geometrical dimensions, and distribution and dimensions of gaps, the two are exactly the same. In essence, the only difference between the two lies in the applied boundary conditions. In the first one (biaxial), a pure biaxial loading is applied, in the form of displacement-controlled tensile loading acting in two perpendicular directions. In the second one (semi-biaxial), a slightly different type of loading is applied, where a displacement-controlled tensile load (along the y-axis) acts on the two longitudinal arms of the specimen, while the other two arms are clamped.

The cruciform-shaped design, used for the FE modelling of the biaxial and semi-biaxial tensile specimens is shown in Figure 4.2. This design is a theoretical concept of a specimen suitable for a biaxial tensile testing machine, intended to be manufactured and used in the TUD lab in the future. Note that the geometry of the specimen is the standard cruciform shape. A typical example of a biaxial testing machine is also presented in Figure 4.3.

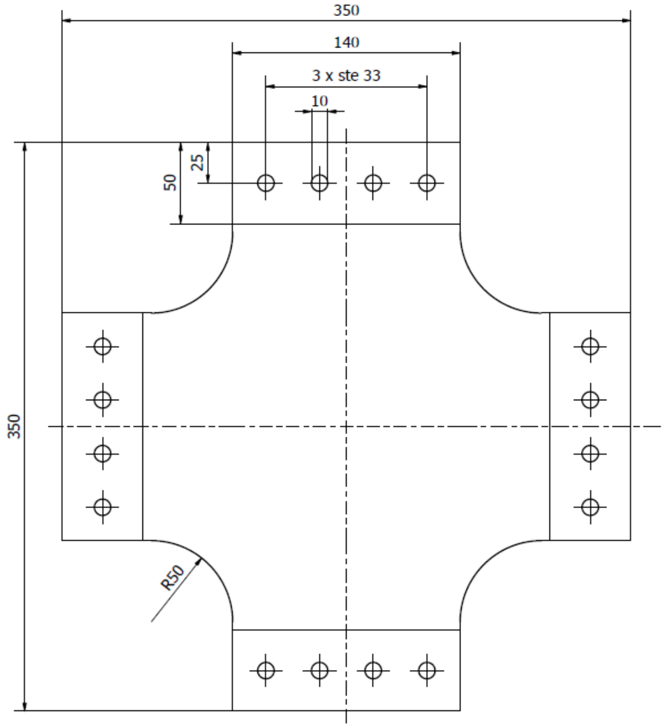

Figure 4.2: Geometry of biaxial tensile test specimen

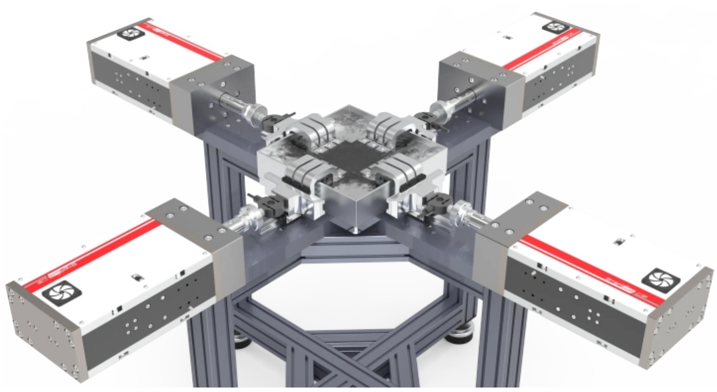

Figure 4.3: An example of a biaxial tension testing machine [54]

Apart from these two, an analysis for a uniaxial tensile testing specimen was also carried out. In terms of its dimensions, it is a simple, rectangular laminate, with its length and width being based on the respective dimensions of the biaxial tensile testing specimen, specifically 350 x 140 mm.

For each specimen type, two models were developed: a baseline specimen (without gaps) and a gap specimen (with tow-drop gaps). The gap specimen was designed to contain all tow-drop gaps into a single ply, referred to as the gap layer, replacing a corresponding ply in the baseline specimen. Then, to initially assess tensile strength reduction based on First Ply Failure (FPF) load, the performance of the gap specimens would be compared to that of the baseline specimens. Having the gaps inside one single ply would reduce complexity in the experimental setup, as it would allow for direct comparisons between the baseline and the modified specimen without having to change multiple layers or configurations. In addition, this choice allows for easier identification of failure mechanisms during testing, as the gaps are isolated in one specific location and thus, the complexity of interactions between gaps in multiple plies or staggered configurations is eliminated. Consequently, this setup reduces ambiguity, making it easier to pinpoint how and where failure initiates and propagates. Moreover, the selection of one single gap layer provides a better understanding of the interaction of adjacent tows in the presence of gaps, for similar reasons. Including multiple gap layers (especially in the case of non-staggered gaps) would make the detection of failure initiation and propagation much more complicated, not to mention the much greater time and effort that would be needed to model multiple gap layers. The details of the FE model setup for all the designs will be presented later in this chapter.

4.1. Materials used in FEM

The properties of all relevant materials used in the design and analysis process will be presented in this section. Regarding the CFRP material, the HexPly® 8552 epoxy matrix system, along with the AS4 high strength carbon fibers is used, forming the HexPly® 8552 AS4 prepreg [55]. Since the gaps will be modelled (initially) as resin-rich areas, properties of neat resin are also needed, and can be found in Table 4.2. Apart from the material properties, the tensile strength of the neat resin is also given in the prepreg's datasheet [55], with a value of 121 MPa. The nominal cured ply thickness of the prepreg is 0.13 mm, at a 37% cured resin content (hence 63% cured fiber content). The ply tow width is 1/4", or 6.35 mm.

Additionally, the relevant values for the strengths of the prepreg material are presented in Table 4.3 below. These values will be needed for calculating the failure criteria used in this thesis and which are presented in the next chapter, along with the results of the FE analyses.

HexPly® 8552 AS4		
Material Property	**Units**	**Value**
E_1	MPa	141000
E_2	MPa	10000
ν_{12}	–	0.3
G_{12}	MPa	4500
G_{13}	MPa	3000
G_{23}	MPa	3000
t (ply thickness)	mm	0.13
tw (tow width)	mm	6.35

Table 4.1: Material properties of HexPly® 8552 AS4 [55]

Hexcel 8552 Neat Resin		
Material Property	**Units**	**Value**
E	MPa	4670
G	MPa	1752
ν_{12}	–	0.33

Table 4.2: Material properties of Hexcel 8552 Neat Resin [55]

HexPly® 8552 AS4		
Strength Property	**Units**	**Value**
X_T	MPa	2207
X_C	MPa	1531
Y_T	MPa	81
Y_C	MPa	216
S_{12}	MPa	114
S_{23}	MPa	95

Table 4.3: Strength properties of HexPly® 8552 AS4 [55]

Apart from the above, unidirectional Glass Fiber Reinforced Polymer (GFRP) was also used as a material, in the form of a plate with a thickness of 2 mm, which is something that can be found relatively easily in the market. This material was used in the biaxial and semi-biaxial specimens, essentially enclosing the CFRP laminate. This choice was made in order to reinforce the arms of the specimen and shift the failure location to the center of the laminate, where the gaps are also located. An assumption was made about the GFRP material properties, based on the material values of a common used GFRP laminates found online [56]. The relevant material and strength properties are presented in Tables 4.4 and 4.5.

UD GFRP		
Material Property	**Units**	**Value**
E_1	MPa	24132
E_2	MPa	20684
ν_{12}	–	0.136
G_{12}	MPa	3800
G_{13}	MPa	2000
G_{23}	MPa	2000
t (plate thickness)	mm	2

Table 4.4: Material properties of UD GFRP 2 mm thick plate [56]

UD GFRP		
Strength Property	**Units**	**Value**
X_T	MPa	344.7
Y_T	MPa	275.8
S_{12}	MPa	89

Table 4.5: Strength properties of UD GFRP 2 mm thick plate [56]

4.2. Specimen layups

In terms of layup, all the specimen laminates were decided to be 7-ply thick, meaning a total laminate thickness of 0.91 mm (for a ply thickness of 0.13 mm). This choice was made after consideration of the desired thickness for the laminate, but also the need for it to be balanced and symmetric. As the latter requirement is driven by the ply orientations, let's first discuss this part.

4.2.1. Layup for uniaxial tensile specimen

First of all, it is obvious that for a uniaxial tensile specimen, at least some of the plies should be oriented at 0°. This is due to the inherent capability of the fibers in a composite material to carry most of the load, as they are much stronger and stiffer than the resin matrix. In the uniaxial tensile test, the load would be applied in a single direction (along the length of the specimen). If the fibers are aligned in the same direction as the applied load (0°), the composite can effectively use the high stiffness and strength of the fibers to resist deformation and failure. However, after an initial assessment for the baseline, it was shown that a 7-layer specimen containing only 0° plies would fail at a very high load (around 350 kN), much exceeding the 250 kN capability of the DASML testing machine. Therefore, it was decided to change the orientation of some of the plies, in order to reduce the failure load into acceptable limits.

The question then became what that orientation should be. In general, simulations showed that as the angle increases from 0° towards 90°, the failure of the specimen shifts from fiber to matrix driven. Matrix failure is something that if possible (at least for the uniaxial tension specimen) should be avoided, as it is a complicated failure mode, with usually no clear signs of identification. Unlike fiber failure, which is typically abrupt and occurs at well-defined stress levels, matrix failure can develop gradually, leading to non-catastrophic but progressive damage that is harder to detect and quantify. Due to the requirement to have a symmetric and balanced laminate, it means that out of the seven plies, four should be in an orientation other than 0°. After performing a few simulations, it was concluded that this shift in failure mode occurs slightly lower than ±45°. More specifically, for four plies oriented at ±50°, the Hashin failure criterion estimated the failure indices as follows: $F.I._{\text{matrix, tensile}} = 0.92$ and $F.I._{\text{fiber, tensile}} = 0.57$. When the ply orientations were reduced to ±45°, the failure indices became $F.I._{\text{fiber, tensile}} = 0.64$ and $F.I._{\text{matrix, tensile}} = 0.69$. It is inferred thus, that further reducing the orientations below ±45° would shift the dominant failure mode from matrix-driven to fiber-driven. Additionally, it was observed that increasing the orientation angle of the non-0° plies resulted in a decrease in the failure load. Consequently, to maintain fiber failure while ensuring a sufficiently low failure load, the orientation of the non-0° plies was selected to be ±40°. Hence, for a 7-layer baseline uniaxial tensile specimen, the layup was decided to be: [0/+40/-40/0/-40/+40/0]. Note that the laminate is balanced and symmetric around the central 0° ply.

Regarding the gap specimen, it was decided that the gap layer would substitute the central 0° (ply 4), effectively making the gap specimen balanced and symmetric around the gap layer. This choice was based on the desire to place the gaps on the inside of the laminate, as if they were to be induced on the external plies, two gap layers would exist, something that was rejected early on. An additional advantage of the central gap layer is that it allows for the modelling of the cured geometry of the specimen. This is of course also feasible if the gap layer replaced any ply from 1 to 6, but placing it outside the middle ply would require a second gap layer to maintain balance and symmetry. Positioning the gap in the outermost ply (ply 7) would eliminate out-of-plane fiber waviness, making it unsuitable for addressing Research Subquestion 2 (see Chapter 2).

For clarification of the specimen layup definition, the possible ply orientations are presented in Figure 4.4. The ±40° orientations are measured from the longitudinal axis (0°) of the laminate: -40° counterclockwise and +40° clockwise.

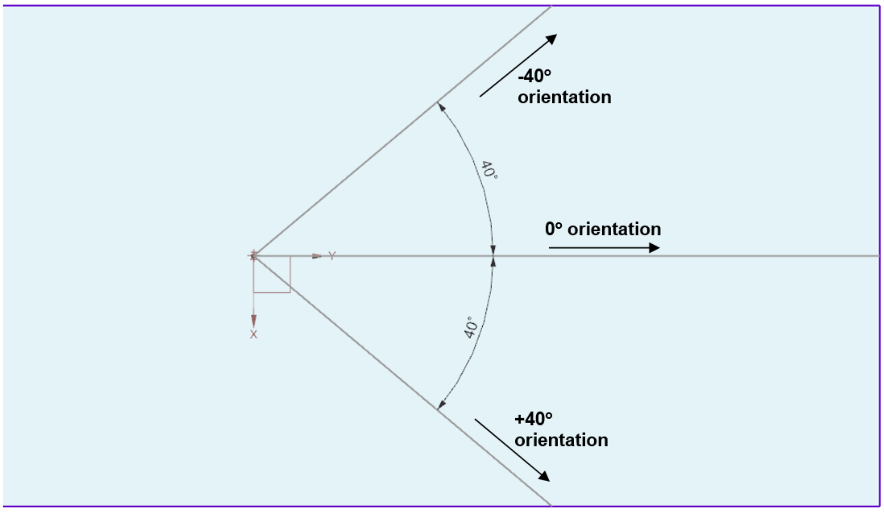

Figure 4.4: Ply orientations in the uniaxial tensile specimen

4.2.2. Layup for biaxial and semi-biaxial tensile specimen

Contrary to the uniaxial tensile specimen, the other two specimens are planned for biaxial (or semi-biaxial) tensile testing, which means they would experience loads in two perpendicular axes. Therefore, both 0° and 90° plies are needed in the specimen layup, in order to ensure sufficient load-bearing in both directions. Due to the constraint about the specimen thickness, it was decided not to include other orientations and thus, for a 7-ply laminate, the resulting (balanced and symmetric) baseline layup is: [0/90/90/0/90/90/0]. The main reason for this layup is to have the middle ply as 0°, allowing it to be replaced by the gap layer, as in the uniaxial tensile specimen. For a 7-ply laminate, above the middle ply there are three plies, and the same amount of plies exists below the middle ply. To include both 0° and 90° plies, at least one or two of the plies above and below the middle must be 90°. If only one ply in each section is 90°, the laminate would have five 0° plies and two 90° plies, creating an imbalance with much greater strength in the 0° direction. To achieve more balanced strength in both directions (a total balance is impossible in a laminate containing an odd number of layers), two 90° plies are placed above and below the middle, resulting in a layup with three 0° plies and four 90° plies. Note that, as can be seen in Figure 4.5, the 0° orientation is parallel to the y-axis of the specimen, while the 90° orientation is parallel to the x-axis of the specimen.

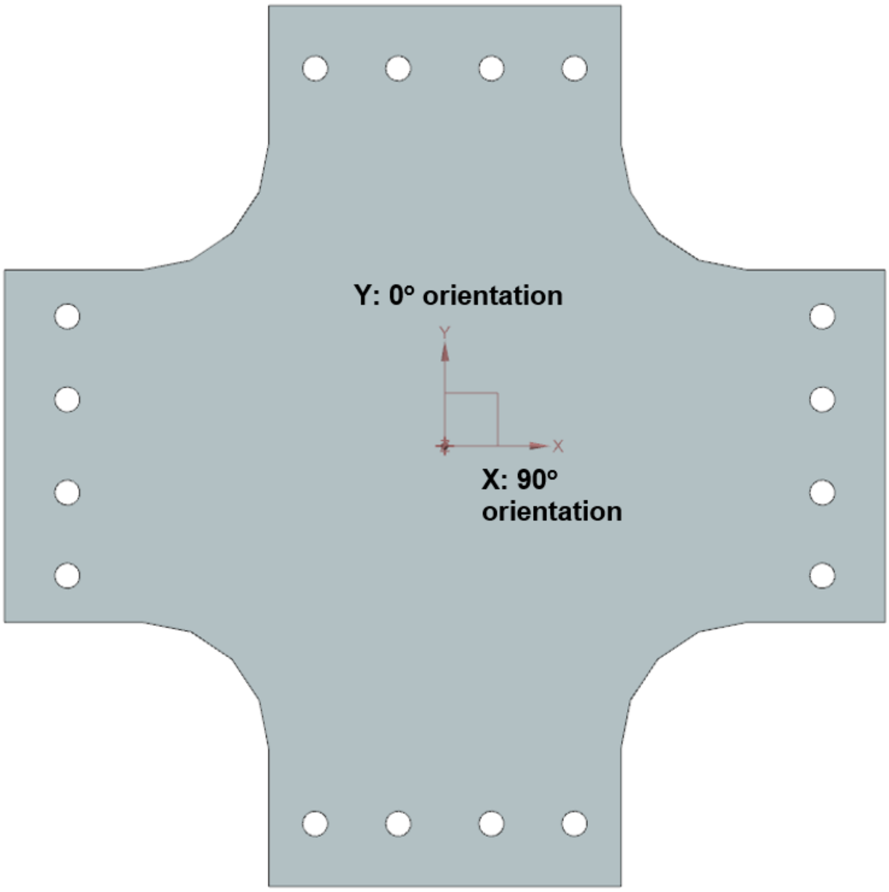

Figure 4.5: Ply orientations in the biaxial and semi-biaxial tensile specimen

4.3. Possible Gap Layer Designs

In this section, the various gap layer concepts considered for the design are presented. Two concepts were rejected due to significant limitations, and one concept was selected as the final design.

4.3.1. Gap Layer option 1

The first idea about the gap layer geometry came from a suggestion in Czel's thesis [39] about a possible optimal design for a specimen containing tow-drop gaps. As can be seen in Figure 4.6, the gap layer in this case would consist of one (or multiple) strips of unidirectional CFRP material laid at an inclined angle, surrounded by enveloping axial tows (at 0°), forming tow-drop gaps whose shape can be controlled to achieve any desired aspect ratio by adjusting the inclination angle. Larger inclination angle values (so from 0° towards 90°) would create tow-drop gaps with larger length-to-width aspect ratio.

This concept, although it seemed promising at first, posed some critical issues that made it considered unsuitable finally. First of all, multiple tow-drop gaps are created one next to the other. This distribution of gaps complicates the interpretation of failure mechanisms, as the overlapping stress fields and interactions between adjacent gaps decrease the ability to isolate and study the behaviour of individual gaps. This lack of clarity makes it challenging to draw precise conclusions about the failure causes and undermines the design's usefulness for detailed evaluation of the impact of the tow-drop gaps.

Additionally, with this concept, fiber steering is essentially not used, as the gap introduction is very similar as in the research of Falcó et al. (2014) [25]. Although the gaps have the characteristic triangular shape that is desired, they are produced with straight tows, limiting the correlation with real-life defects found in curved geometries. This correlation is essential, as discussed in Chapter 3.

Manufacturing difficulties could also arise with this gap layer design. First, the inclined tow (or tows) would have to be precisely placed in the desired position (center of the ply to be constructed) and then each axial tow would have to be accurately laid down and cut in the exact location where the inclined tow edge begins, in order to make sure that the pattern of gaps presented in Figure 4.6 is achieved. Especially in the corners of the inclined tow (bottom left and top right in Figure 4.6), the exact termination of the axial tows could be quite a challenge. Slight errors in the placement of the tows could produce a number of overlaps apart from the gaps, something that is not desired in the context of this thesis.

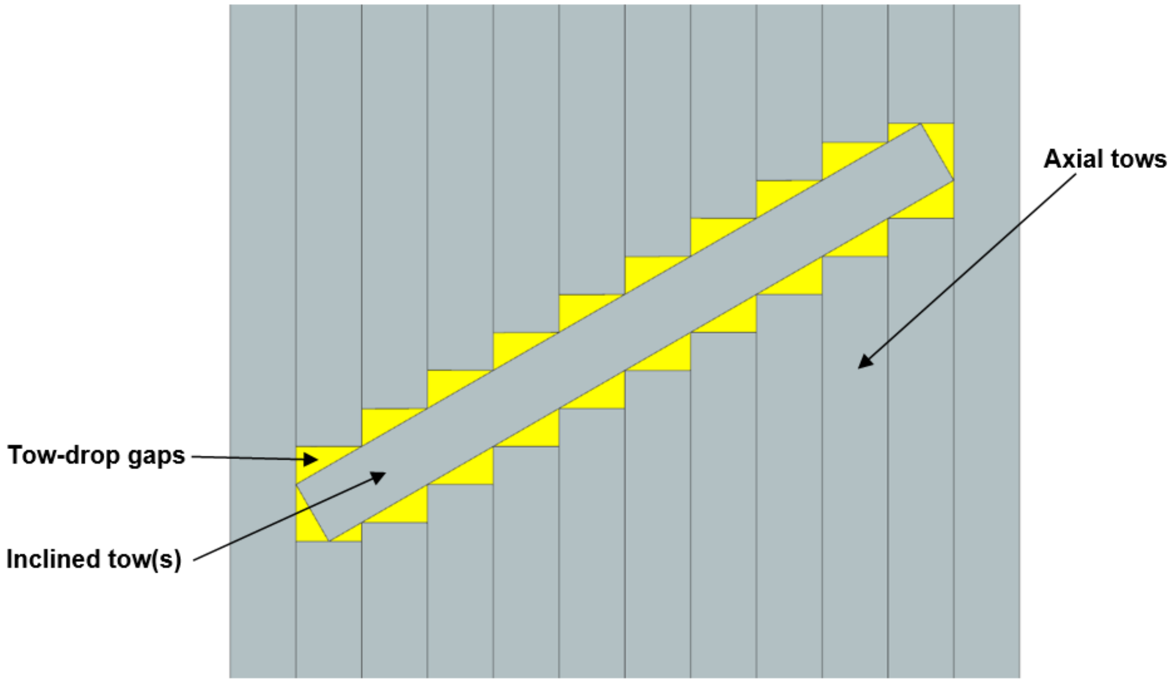

Figure 4.6: Gap Layer option 1 (zoomed in area containing gaps)

4.3.2. Gap Layer option 2

Apart from the gap layer discussed above, another option was investigated. This option involved introducing separated gaps into the middle ply of the laminate, (more or less) far apart from one another. In Figure 4.7, a possible design of this gap layer is presented. It is obvious that these gaps cannot be created with tow-dropping during AFP, since in order to produce the triangular shape that is needed for characterizing this type of defects, the respective tow would have to be terminated under an angle, something not feasible with current AFP techniques. To address this issue, the gaps would need to be created manually, likely using a specialized cutter. However, since the gap layer is in the middle of the laminate, manual cutting during layup risks damaging the underlying tows. To solve this, a metal strip could be placed over the underlying laminate ply before cutting the gaps in the gap layer, which would prevent damage in the plies underneath. Once the gaps are created, the strip would be carefully removed, leaving the laminate intact. Note that two isolated gaps are introduced in this concept, but the creation of multiple gaps is also possible. Even one single gap could be created, if the goal is to examine the impact of a single, isolated gap.

Although this option would solve the problem of clustered gaps that could obscure the failure identification and understanding, additional issues would be caused, which eventually led to the dismissal of this idea as well. The main reason of rejection was the method of gap introduction, as the process that was described above adds extra manufacturing complexity, which is something unnecessary and to be avoided if possible. However, another (and probably more important) reason for not choosing this method is the fact that tows would need to be cut not only perpendicularly, but also under an angle. In this method (Figure 4.7), the tow is cut on two sides to form the triangular gap, severing fibers in both directions. This process weakens the tow by disrupting its continuity and increasing the likelihood of stress concentrations at the cut edges. These stress concentrations can serve as initiation points for cracks or delamination, potentially excessively reducing the local strength of the material, compared to the traditional tow-dropping technique during AFP. Thus, in order to be closer to real-life tow-drop gaps, which would allow for a more accurate estimation of their impact, this design was also rejected.

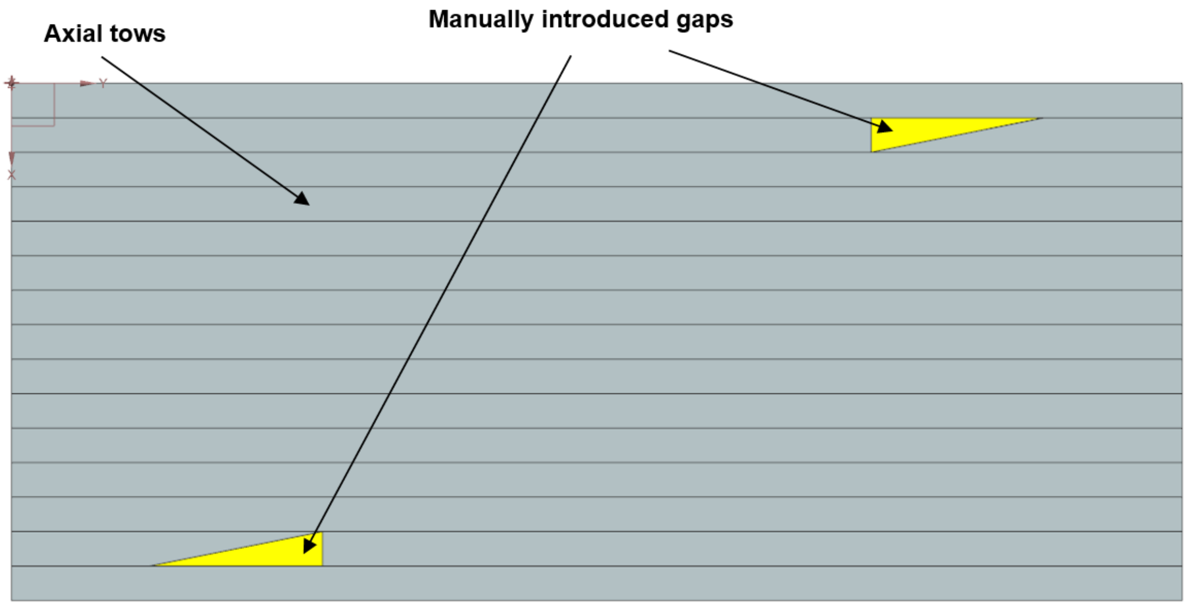

Figure 4.7: Gap Layer option 2

4.3.3. Gap Layer option 3

As outlined in Chapter 3, a key requirement for a specimen to accurately represent tow-drop gaps from AFP is for the gaps to exhibit a characteristic triangular shape. This shape can be achieved in several ways, but the approach that was qualified involves taking advantage of the tow-steering capabilities of the AFP process. By steering tows that are initally oriented at 0° and then returning them to their original 0° orientation, a one-tow-width distance is created between adjacent tows. If an additional 0° tow is placed between these two and cut precisely at the point where the steering begins, a gap is formed. This gap has a shape that closely resembles the shape of standard tow-drop gaps induced by AFP, with a base width of 6.35 mm (one tow width) and a total length of 71.2 mm (from the base until the tip of the gap). Therefore, the gaps created using this method conform at a great extent with the requirements set in Chapter 3 regarding the geometry and size of gaps.

The advantage of this method is that it enables precise control over the gap's shape, ensuring a consistent triangular form representative of actual tow-drop gaps seen in AFP processes. Note that the design of the gap layer essentially follows the same principle for both the uniaxial and biaxial specimens, with the AFP machine laying down, steering and terminating tows accordingly, until the whole surface of the ply is covered. For symmetry reasons, three gaps are created with this technique, with the central one being reversed compared to the other two. A distance of 31.75 mm (five tow widths) is maintained between gaps to ensure they do not influence each other's behaviour. For the uniaxial tension specimen, the same distance (5 tow widths) is maintained between the edges of the gaps and the specimen's edges to isolate the gaps from free-edge effects, making sure their impact can be accurately assessed.

In terms of steering, a steering radius of 400 mm is used for the design of all gap layers. This is the minimum steering radius that can be achieved with AFP [39], but of course some process testing will be needed during the actual manufacturing, to ensure that this specific material can withstand such a degree of steering.

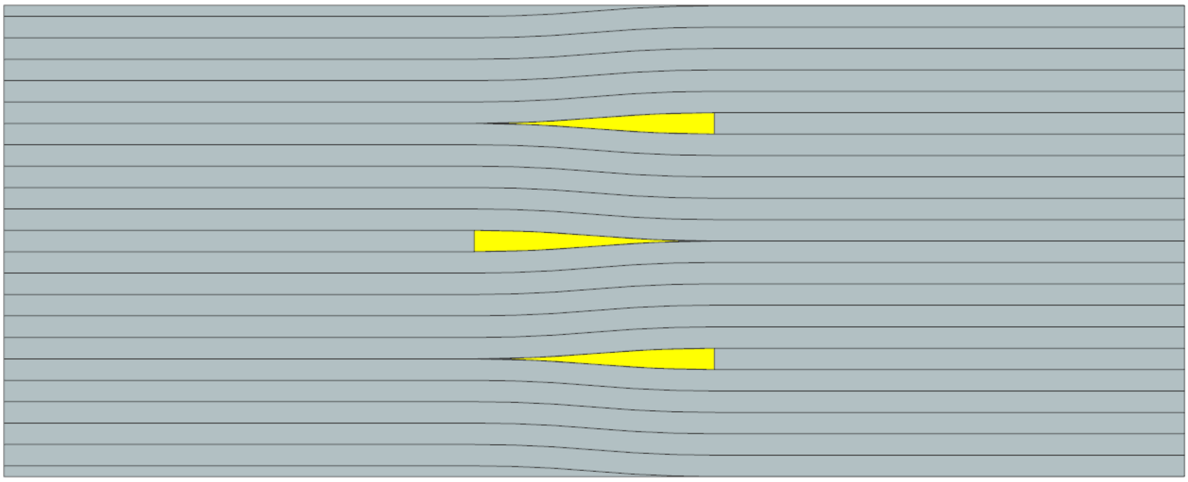

Figure 4.8: Definition of gap layer for uniaxial tension specimen

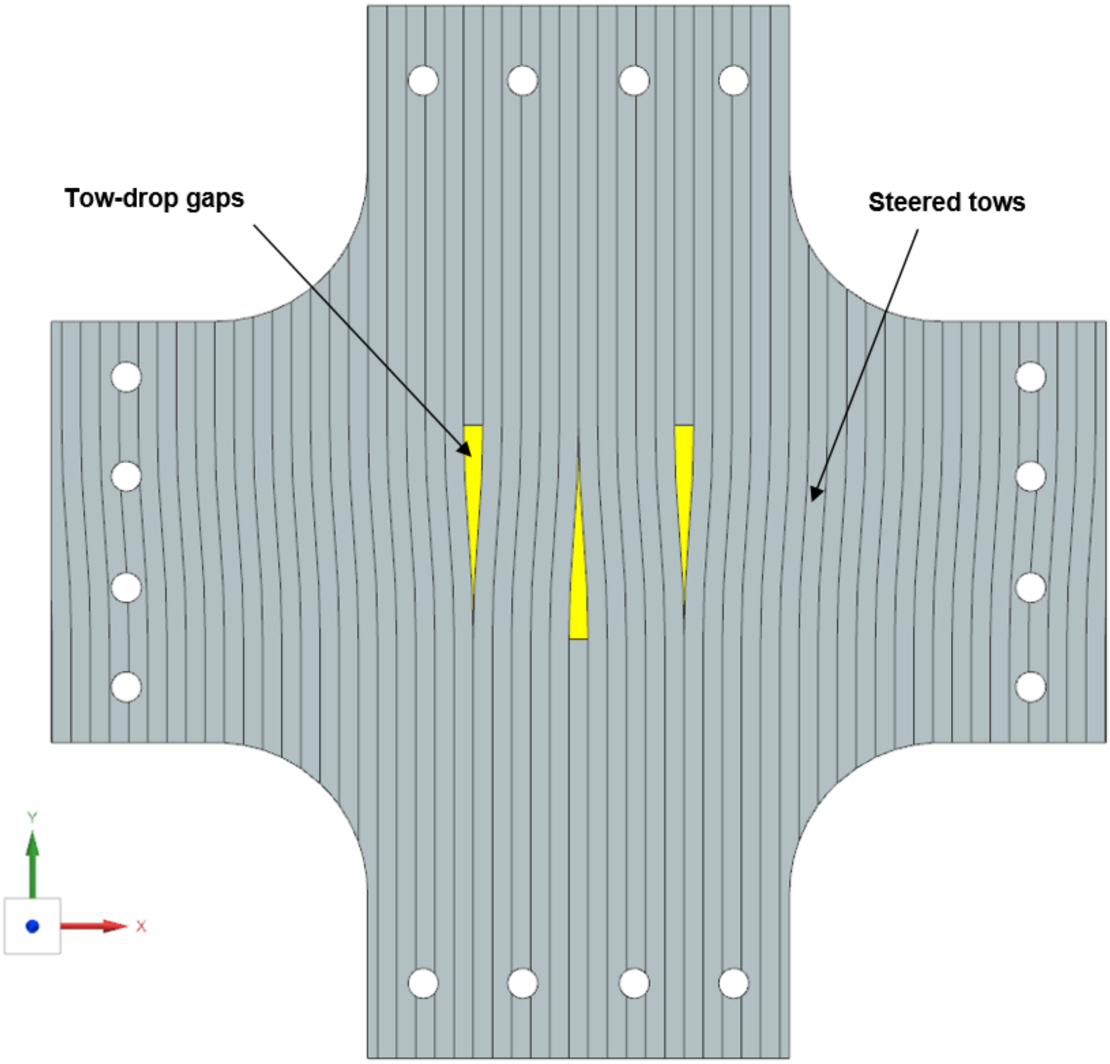

Figure 4.9: Definition of gap layer for biaxial tension specimen

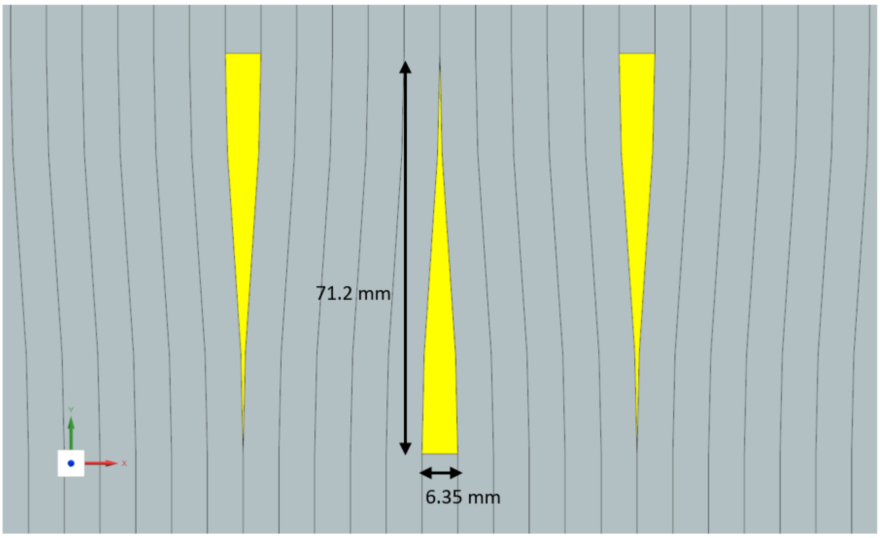

Figure 4.10: Definition of gap layer (zoom)

4.4. FE model for uniaxial tensile specimen

To attempt to answer the research questions posed in this thesis as accurately as possible, an extended use of FE modelling was deemed necessary. The FEM software that was used was Siemens NX/ Simcenter 3D. For the uniaxial tensile specimen, the FE model for the baseline (laminate without gaps) was first created, in order to get a first estimate about the failure load and ensure it is below the respective limit. Shell elements were initially used, for a faster model setup and run time. However, although for a simple flat laminate with no defects, shell elements were proven to be sufficient for an accurate analysis, it was quickly revealed that for a more detailed model containing gaps, elements capable of capturing a three-dimensional stress field were necessary; therefore, solid elements are used in this work.

The first attempt to simulate the gap specimen did not involve the actual geometry of the laminate after curing, therefore fiber waviness was not accounted for at this stage. The laminate was modelled as a solid block of material, composed of 7 layers one on top of each other, well connected with glue constraints. Each layer represents one ply and has a thickness of 0.13 mm, making up a total of 0.91 mm thickness for the whole laminate. Plies 1 to 3 and plies 5 to 7 are essentially 3D rectangular plates (with dimensions 350 x 140 x 0.13 mm). Ply 4, which is the gap layer, is identical with the others in terms of total dimensions, only with a very important distinction: it is divided in four distinct areas. Three of these areas represent the gaps and one covers the remaining portion of the layer. This is done in order to simulate the different materials that are at play in the gap layer. More specifically, the gap layer has the material properties of the CFRP material everywhere, apart from the gap areas. These areas are assigned the material properties of the neat resin, therefore considering the gaps as resin pockets.

Regarding the mesh of the model, a mesh convergence study was performed in order to estimate the level of mesh refinement needed to capture the necessary details. The results of this study are presented in Figure 4.11. It can be seen that as the element size in the gap areas decreases (from 2 mm to 0.125 mm), the maximum failure index ($F.I.$) predicted by the Hashin criterion for a 100 kN tensile force stabilizes around $F.I. = 0.88$. This occurs at an element size of 0.5 mm, as the difference in the failure index compared to a 1 mm element size is negligible, approximately 0.1%. A 1% F.I. deviation was set as the convergence criterion, indicating that the solution is considered converged if consecutive iterations differ by less than this threshold. The solid elements that were used were the CHEXA8 elements (3D hexahedral finite elements). The size of the elements was decided to be 2 mm for plies 1 to 3 and 5 to 7, as well as for the gap layer, apart from the gap areas. For the latter, a 0.5 mm element size was chosen instead, in order to cover the complex geometry of the gaps as well as possible. With these element sizes, around 97000 elements in total were featured in the final model. Only one element per layer was used in the thickness direction to reduce the total number of elements, significantly lowering computational effort and time — something critical for iterative analyses. However, this approach limits the accuracy of capturing through-thickness stress gradients and failure mechanisms, such as delamination and interlaminar stresses, which require finer discretization. Despite these limitations, this meshing strategy was considered acceptable.

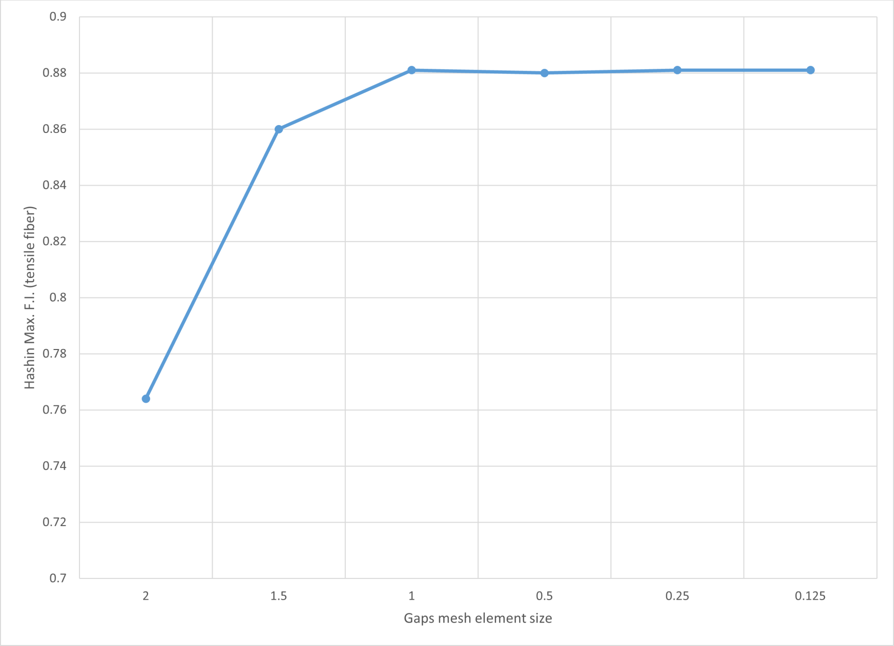

Figure 4.11: Mesh convergence study for gap area of the uniaxial tensile gap specimen

A crucial aspect for an accurate FE analysis is the correct material orientation in every part of the model, since the primary material is CFRP and thus anisotropic. For all plies except the gap layer, the material orientation is determined by the ply's specified angle (0°, +40°, or -40°) using the corresponding in-plane vectors in the XY plane. For the gap areas, material orientation is not important since the resin is isotropic. However, in the gap layer, the material orientation for the areas of the ply that are steered (adjacent to and between the gaps) should align closely with the tow steering. This is achieved by assigning the material orientation per element, with a vector tangent to the steered tow boundary, hence defining the primary material direction. A visualization of this is provided in Figure 4.13.

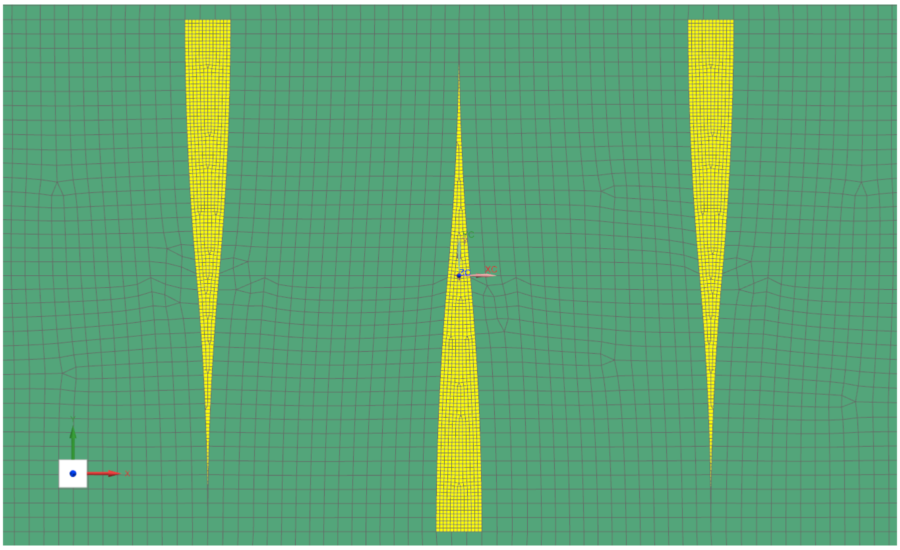

Figure 4.12: Gap layer meshes for CFRP (green) and gaps/resin pockets (yellow)

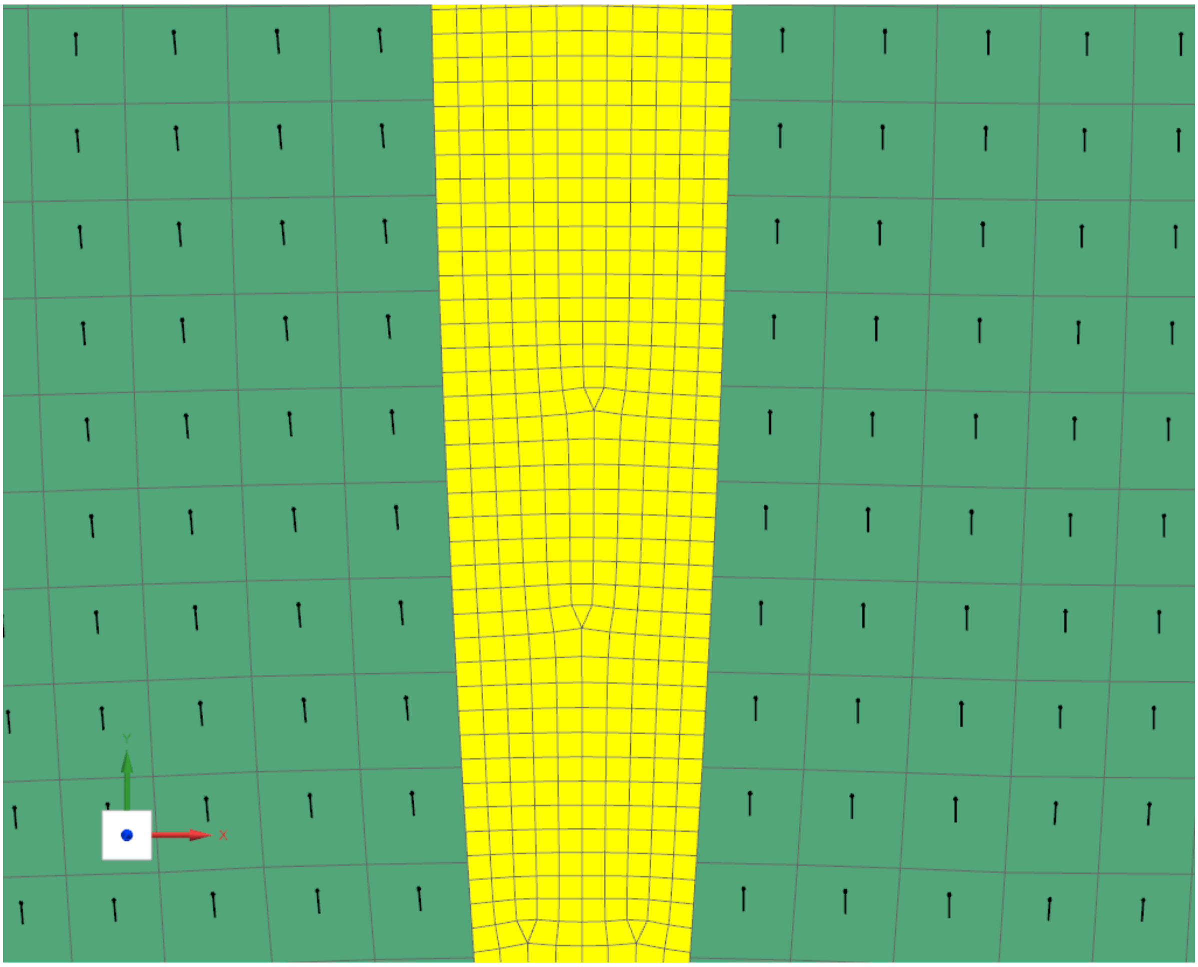

Figure 4.13: Gap layer meshes for CFRP (green) and gaps/resin pockets (yellow) - zoom. The black arrows show the material orientation, which follows the steered tow boundaries

As for the boundary conditions, for the uniaxial tensile specimen, a fixed constraint was imposed on one edge, along the width of the specimen. The opposite edge of the specimen was restricted to move or rotate in all directions, apart from the longitudinal axis of the specimen, along which axis was assigned a tensile force. The tensile force magnitude was chosen arbitrarily but was reasonably aligned with the expected failure load for this laminate in a tensile test. As will also be explained in the next chapter, a failure index based on a certain failure criterion will be calculated in the analysis, and the First Ply Failure (FPF) load can be estimated by interpolation. These conditions ensure that a pure uniaxial tensile load is simulated. All boundary conditions were applied on a node in the center of the respective edge, which was connected to the whole edge with tie constraints (RBE2 elements). The boundary conditions applied on the model are presented in Figure 4.14.

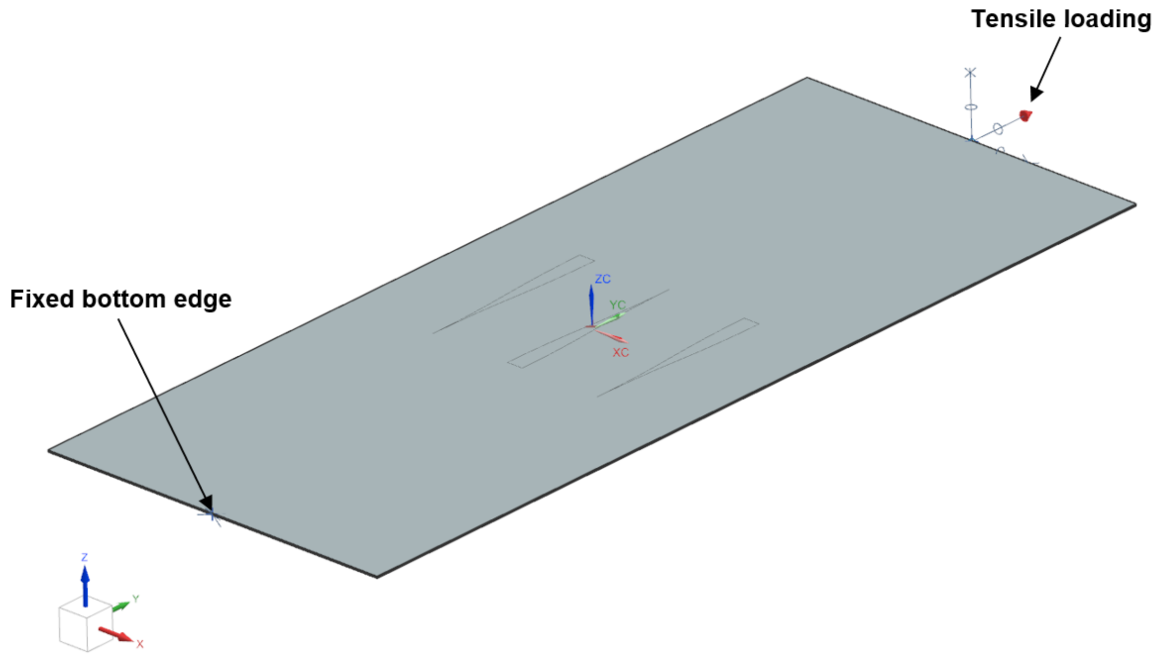

Figure 4.14: Boundary conditions in the uniaxial tensile specimen model. The outline of the gap areas in the middle of the laminate is also slightly visible

4.5. FE model for biaxial and semi-biaxial tensile specimen

The process for the FE modelling of the biaxial and semi-biaxial tensile specimens was largely similar to that of the uniaxial tensile specimen. In essence, a single FE model was created for both specimens, with two separate boundary condition sets applied (one for each specimen). In terms of geometry, the laminate was again modelled as a solid, with seven layers having the cruciform shape presented in Figure 4.2 and a thickness of 0.13 mm being stacked one on top of the other. Two unidirectional GFRP plates were also attached to the outside plies of the 7-ply CFRP laminate, with a rectangular cutout in the middle in order to reinforce the arms of the specimen and move the failure location to the inside, where the gaps also exist. The same type of solid elements (CHEXA8) was again used, with around 200000 elements in total. The large increase in the total number of elements (almost double), compared to the uniaxial tensile specimen, is due to the larger dimensions of the biaxial tensile specimen. Details about the mesh will not be presented here, since the meshing process was more or less the same as in the uniaxial tension specimen.

In terms of boundary conditions, for the biaxial specimen, a displacement controlled loading was assumed, meaning that equal (but opposite in direction) displacement is applied in all four ”arms” of the specimen (Figure 4.15). The (tensile) displacement is applied at a coupling point in the middle of each arm's edge, connected to the entire edge using tie constraints (RBE2 elements, as before). This coupling point is also restricted to move or rotate in any other direction, thus, a pure biaxial displacement is achieved. The details of the specimen's geometry and boundary conditions are presented in Figure 4.15.

As mentioned before, for the modelling of the semi-biaxial specimen, only the boundary conditions of the model that had already been set up for the biaxial specimen were altered. Specifically, instead of applying displacement controlled (tensile) loading in all four arms, only the two arms (along the y-axis) were prescribed with this kind of loading. The other two arms of the specimen (along the x-axis) had their edges fixed, simulating a clamped boundary condition that would induce a reactive tensile force due to the Poisson's effect, as the specimen wants to contract in the transverse direction. The boundary conditions of this specimen can be seen in Figure 4.16.

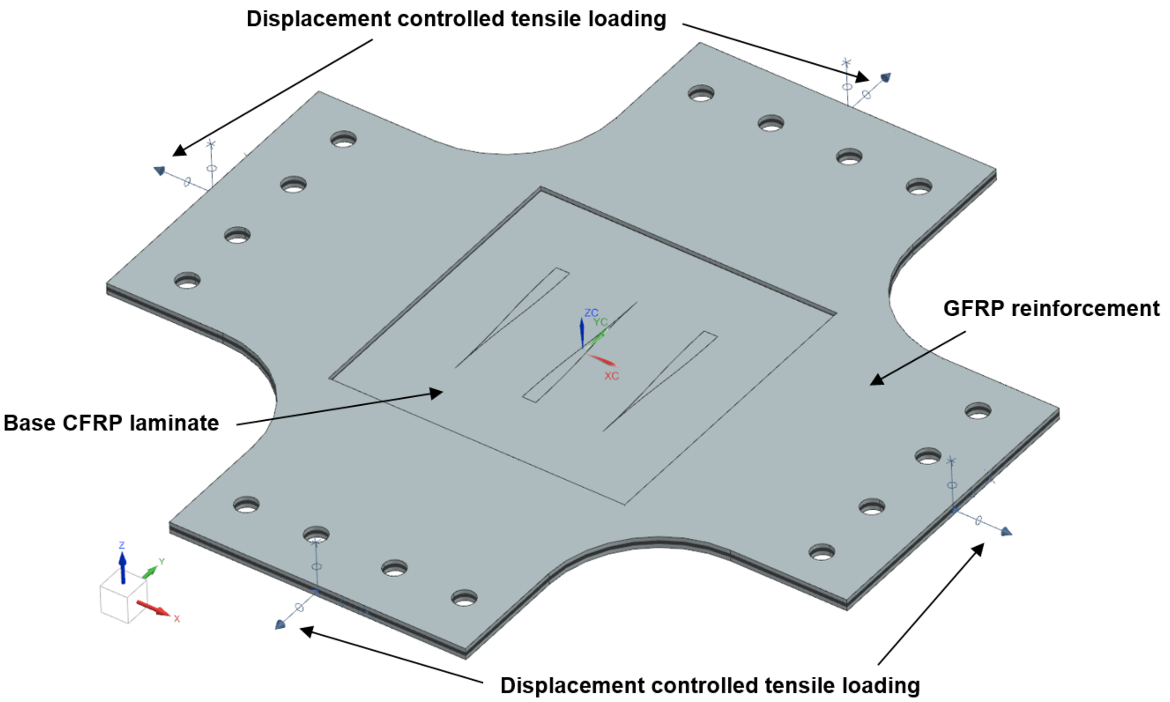

Figure 4.15: The biaxial tensile specimen model and its boundary conditions. The outline of the gap areas in the middle of the laminate is also visible

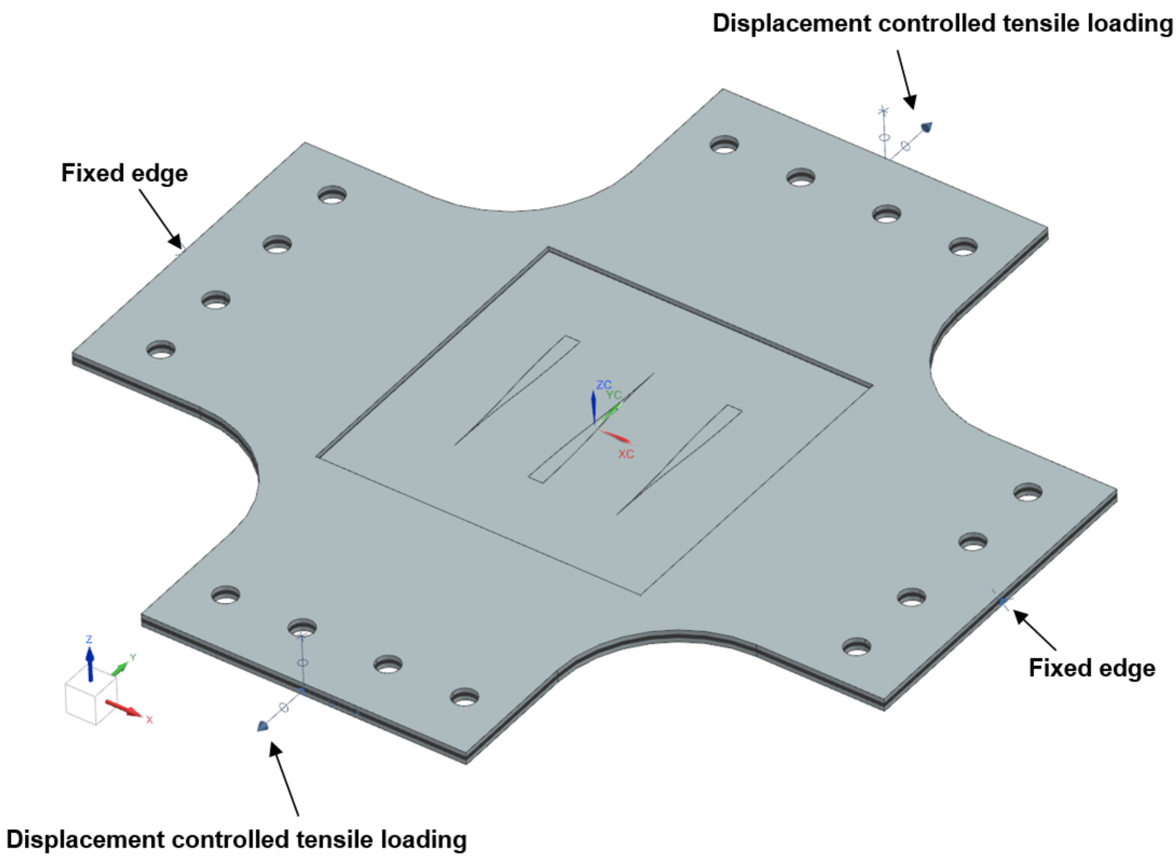

Figure 4.16: Boundary conditions in the semi-biaxial tensile specimen model. The outline of the gap areas in the middle of the laminate is also visible

5 Initial FEM Results and Discussion

Once the specimen designs described in Chapter 4 were finalized, the FE analyses were prepared and executed. In this chapter, the initial FEM results for the uniaxial, biaxial and semi-biaxial tension specimens will be presented and discussed. Due to limitations of the FEM software, a Python code had to be generated in order to calculate composite failure based on the Hashin failure criterion. Specifically, the principal stresses in each element of each ply are extracted from the FEM results, and are imported into the code which evaluates the Failure Indexes (F.I.) for the four different failure modes of the Hashin criterion. The highest F.I. among the four denotes the type of failure. The mathematical formulation of this criterion is presented once more below [22], [23]:

Tensile Fiber Failure Mode (if $\sigma_{11} > 0$):

$$F.I. = \frac{\sigma_{11}^2}{X_T^2} + \frac{\tau_{12}^2 + \tau_{13}^2}{S_{12}^2} < 1 \tag{5.1}$$

Compressive Fiber Failure Mode (if $\sigma_{11} < 0$):

$$F.I. = -\frac{\sigma_{11}}{X_C} < 1 \tag{5.2}$$

Tensile Matrix Failure Mode (if $\sigma_{22} + \sigma_{33} > 0$):

$$F.I. = \frac{(\sigma_{22} + \sigma_{33})^2}{Y_T^2} + \frac{\tau_{23}^2 - \sigma_{22}\sigma_{33}}{S_{23}^2} + \frac{\tau_{12}^2 + \tau_{13}^2}{S_{12}^2} < 1 \tag{5.3}$$

Compressive Matrix Failure Mode (if $\sigma_{22} + \sigma_{33} < 0$):

$$F.I. = \left(\frac{\sigma_{22}}{2S_{23}}\right)^2 + \left[\left(\frac{Y_C}{2S_{23}}\right)^2 - 1\right]\frac{\sigma_{22}}{Y_C} + \left(\frac{\tau_{12}}{S_{12}}\right)^2 < 1 \tag{5.4}$$

The FE analysis aimed to estimate the First Ply Failure (FPF) load for each specimen type (uniaxial, biaxial, and semi-biaxial) for both baseline and gap specimens. A comparison between the FPF loads of the baseline and the gap specimen would then give a first estimate about the impact of the tow-drop gaps in the tensile strength of the composite laminate. The First Ply Failure theory assumes that the failure of any single ply in a laminate results in the failure of the entire laminate. However, the first-ply failure load is typically conservative, as failure in the form of matrix cracking may not immediately cause the laminate to fail [57]. In reality, what typically occurs is progressive failure, where plies that theoretically have failed at the FPF load can continue to bear some load before final failure. In the context of this thesis, only First Ply Failure is considered. Note that at this stage, the gaps are modelled as resin pockets, without accounting for fiber waviness.

5.1. Uniaxial Tensile Specimen

To achieve accurate results in FEM, it is crucial to apply the correct boundary conditions and load cases. For the uniaxial tension specimen (both baseline and gap specimen), as discussed in Chapter 4, one edge was fixed in all degrees of freedom, while a tensile force was applied on the opposite edge (as seen in Figure 4.14). The tensile force was applied as a point load in the middle of the edge, at a coupling point connected to the whole edge. The top edge was also free to move only in the direction of the tensile force, simulating thus a pure uniaxial tension. In terms of force magnitude, all the analyses were conducted with a 100 kN tensile force. The resulting stresses from this boundary condition and loading configuration were used to calculate the Hashin failure criterion, and based on that the FPF load was estimated using extrapolation. For example, if the highest F.I. from the Hashin criterion at a 100 kN tensile force is exactly 1, the FPF load is 100 kN. If the highest F.I. is 0.8, the FPF load is calculated as 100/0.8 = 125 kN.

5.1.1. Baseline specimen results

In this section the FEM results for the baseline panel will be presented. As can be seen in Figure 5.1, stress concentrations occur in the corners of the rectangular panel. These stress concentrations are due to the boundary conditions applied on the edges. To tackle this issue, the advantages of the well-known St Venant's principle will be exploited. This principle states that the effects of these local disturbances diminish beyond a distance roughly equal to the disturbance size [58]. Therefore, stress concentrations at the corners can be neglected, allowing the analysis to focus on the center of the specimen, where the stress field remains unaffected.

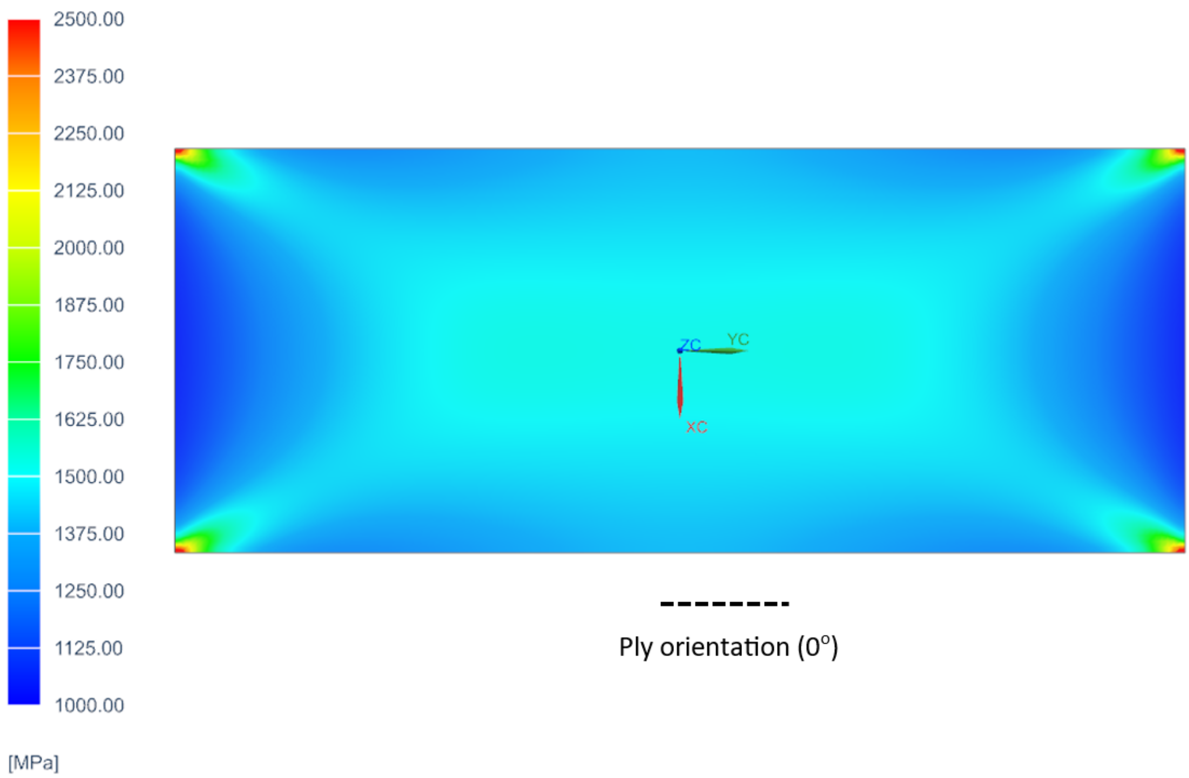

Figure 5.1: Distribution of σ_{11} in ply 1 of uniaxial baseline specimen for a uniaxial tension of 100 kN. The load is applied in the horizontal (0°) direction. Stress concentrations in the corners of the specimen are clearly visible.

The analysis for the panel without defects predicted that the off-axis plies (plies oriented in angles different than 0°, therefore plies 2 (+40°), 3 (-40°), 5 (-40°) and 6 (+40°)) fail first and simultaneously. The Hashin criterion showed a fiber failure occurring at the center of these plies, with a calculated Failure Index equal to 0.69 for a 100 kN tensile load. This means that a first estimate for the FPF load would be: $FPF_{baseline} = 100/0.69 \approx 145kN$.

The analysis results can be visualized in Figures 5.2 and 5.3 which present the normal stress parallel to the fiber direction (σ_{11}), as well as the in-plane shear (τ_{12}) stress for ply 5. The grey areas in the figures indicate regions with stress values exceeding those at the failure area (ply center). The normal stresses in the fiber direction (-40°) at the failure location are relatively low, approximately 312 MPa, as shown in Figure 5.2, representing less than 15% of the material's total tensile strength (2207 MPa). In contrast, the shear stress at the failure location, shown in Figure 5.3, although lower in magnitude (93.7 MPa) corresponds to around 82% of the material's total shear strength. This shows that although fiber failure is predicted, in-plane shear is probably the driving force in the failure of the baseline specimen.

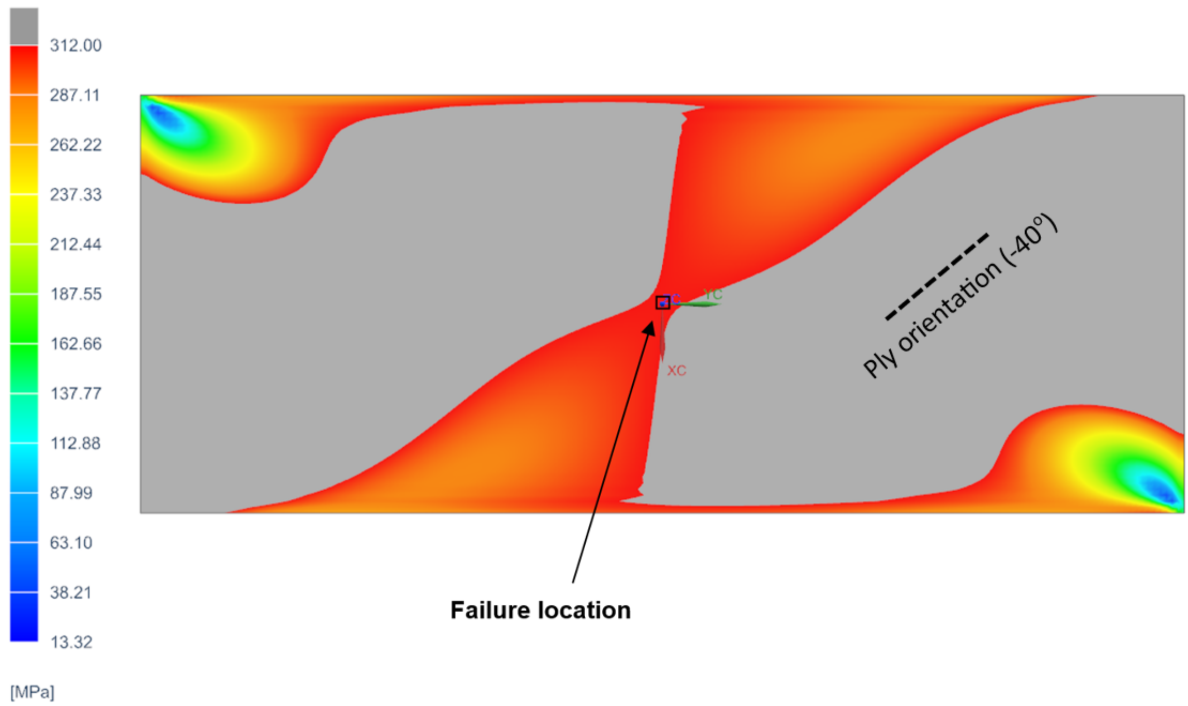

Figure 5.2: Distribution of σ_{11} in ply 5 of uniaxial baseline specimen for a uniaxial tension of 100 kN

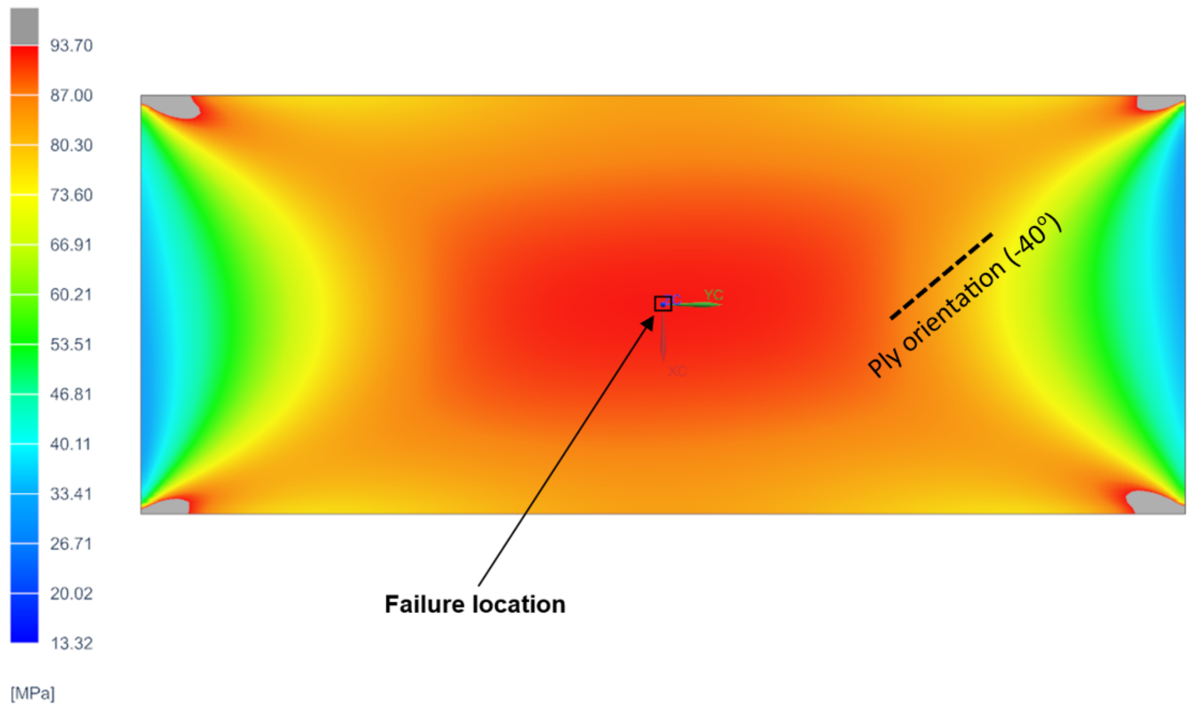

Figure 5.3: Distribution of τ_{12} in ply 5 of uniaxial baseline specimen for a uniaxial tension of 100 kN

5.1.2. Gap specimen results

After obtaining a first estimate about the FPF load of the baseline uniaxial tension specimen, the next step was to run the same FE analysis for the respective specimen containing gaps, as described in Chapter 4. At this point, fiber waviness is not taken into account, therefore the gaps (created with fiber steering as discussed previously) are assumed to be fully filled with resin. The results of this analysis indicated again a fiber failure according to the Hashin criterion, occurring almost simultaneously in plies 3 and 5 which are oriented at -40°. However, in contrast with the baseline specimen, the failure area is not located at the center of the plies, but in the areas of the plies that are directly above or below the gaps (resin pockets) in ply 4, and more specifically close to the gaps' wider edge.

Figure 5.4 presents the σ_{11} distribution on ply 5. The stress scale in this figure is set to the maximum σ_{11} at the failure region (adjacent gap locations), with grey areas indicating regions where σ_{11} exceeds this value. It is clear that the regions with σ_{11} values higher than those at the gap locations are significantly larger; however, these are not the failure regions. This indicates that σ_{11} is not the critical factor in the failure of the gap specimen. Instead, as shown in Figures 5.5, 5.6, and 5.7, the failure locations correspond to peaks in shear stresses τ_{12} and τ_{13}. If the mathematical formulation of the Hashin Fiber Failure Mode is again considered:

$$F.I. = \frac{\sigma_{11}^2}{X_T^2} + \frac{\tau_{12}^2 + \tau_{13}^2}{S_{12}^2} < 1 \tag{5.5}$$

it can be deduced that failure is dependent on the ratios of the (ply) longitudinal and shear stress with their respective strengths. It is observed that in-plane shear τ_{12} has a peak value of 100 MPa, which is almost 88% of the total shear strength of the CFRP material. On the other hand, σ_{11} has a maximum value of 420 MPa in the region of failure, which is less than 20% of the total tensile strength. Thus, it is reasonable (as was the case with the baseline specimen) that the fiber failure predicted by the Hashin criterion is again dominated by shear.

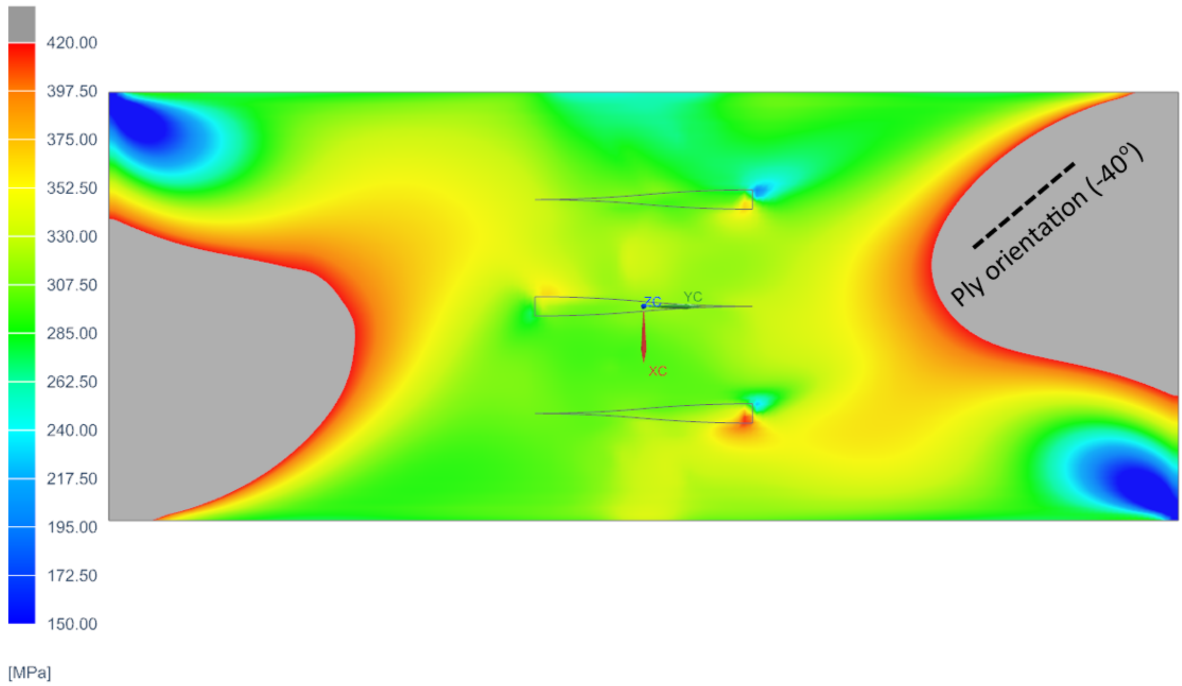

Figure 5.4: Distribution of σ_{11} in ply 5 of uniaxial gap specimen for a uniaxial tension of 100 kN.

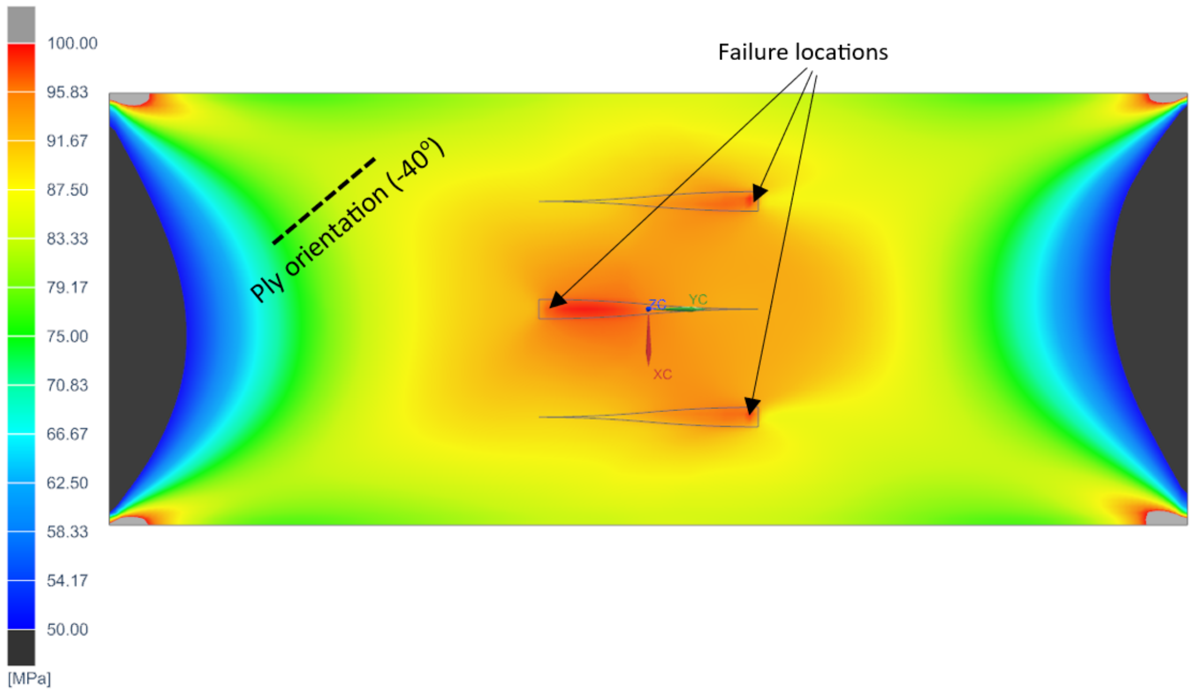

Figure 5.5: Distribution of τ_{12} in ply 5 of uniaxial gap specimen for a uniaxial tension of 100 kN

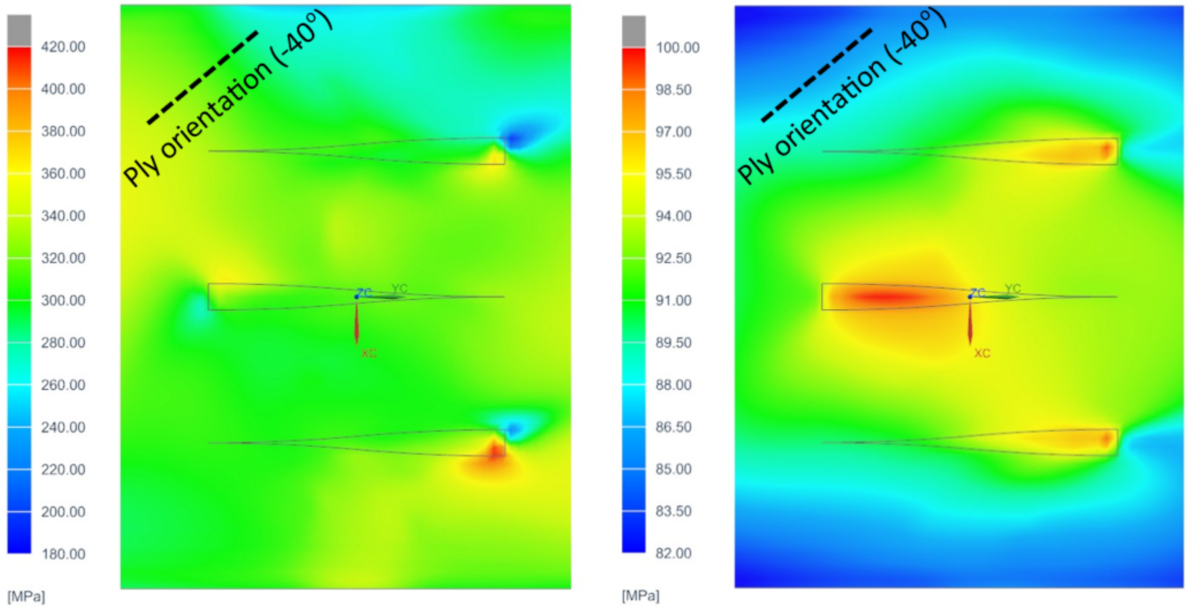

Figure 5.6: Distribution of σ_{11} (left) and τ_{12} (right) in ply 5 of uniaxial gap specimen for a uniaxial tension of 100 kN (zoom)

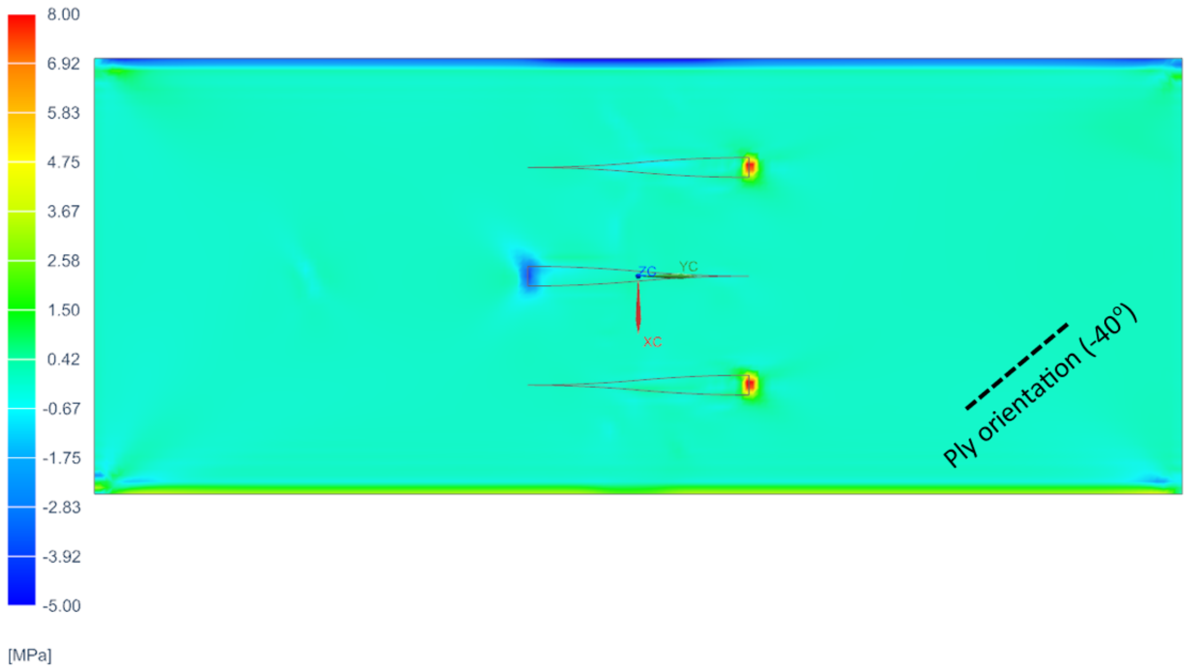

Figure 5.7: Distribution of τ_{13} in ply 5 of uniaxial gap specimen for a uniaxial tension of 100 kN

The predicted failure occurs in the plies adjacent to the gap layer, specifically above or below the wider ends of the gaps. This can be explained by the fact that gaps are modelled —and, to some extent, exist in reality —as resin-rich areas. The tensile load that is applied to one edge of the specimen must be transferred through all the plies along the specimen's length. In ply 4, the load is transferred effectively, until it encounters the resin pockets in the gap areas. Due to the absence of fibers in these regions, the load cannot continue directly and must be redirected, either through the steered tows adjacent to the gaps or through the plies neighboring the gap layer. The portion of the load redirected through the steered tows generates a σ_{11} stress concentration at the edges of the gaps (Figure 5.8). Meanwhile, the load transferred through the adjacent plies creates a shear stress concentration (both in-plane and out-of-plane), which ultimately causes failure in these plies, as previously discussed.

The quantified impact of the gaps on the tensile strength of the specimen is reflected in the calculation of the Hashin criterion, which yielded a maximum fiber failure index (F.I.) of 0.88 for a 100 kN tensile load. This indicates an estimated first-ply failure (FPF) tensile load of approximately $100/0.88 \approx 113.6$ kN, which is 21.6% lower than the corresponding FPF load for the baseline specimen. This strength knockdown is in general in agreement with relevant knockdown values found in literature. More specifically, as is presented in Table 2.1, tensile strength knockdowns range from 2% to 55% depending on laminate thickness and layup, type of gaps (tow-to-tow or tow-drop), gap size and gap introduction. The experimental and numerical studies of Falcó et al. (2014 and 2017) [25], [31] give a similar estimation for the uniaxial tensile strength knockdown, ranging from 12.5% (FE models without accounting for fiber waviness) to 22% (through experimental work, which obviously accounts for the real geometry of the defects after curing). These studies examined multiple gaps across various plies of the laminate, unlike the single gap layer considered in this thesis. Also, the gap size in Falcó et al. (2014 and 2017) [25], [31] is smaller, with the same base width but a length of 29.9 mm, less than half of the 71.2 mm examined here. However, multiple gaps in more than one plies have been studied in these researches, which could make up for the smaller gap size and increase the strength knockdown, especially when gaps are not staggered. Falcó et al. used a different layup as well, including 0°, ±45°, and 90° plies, whereas the uniaxial tensile specimen in this thesis features only 0° and ±40° plies. All of the above prove that, even though the strength reduction results found through simulations in the present thesis can be considered reasonable based on similar results in literature, accurate comparisons are hard, if not impossible to be made, due to fundamental differences among the specimen designs across different studies.

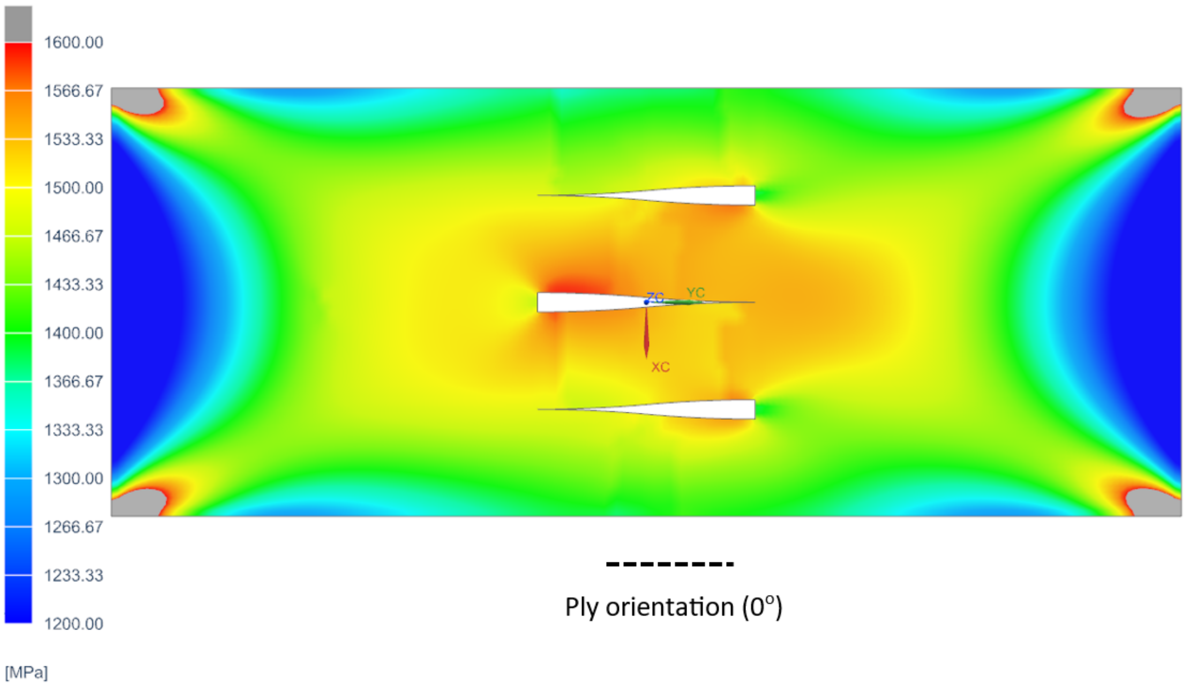

Figure 5.8: Distribution of σ_{11} in ply 4 (gap layer) of uniaxial gap specimen for a uniaxial tension of 100 kN

5.2. Biaxial Tensile Specimen

This section presents the results and discussion for the biaxial tensile specimen. As detailed in Chapter 4, the cruciform-shaped specimen is subjected to biaxial loading under controlled displacement. The displacement magnitude was set arbitrarily to 1 mm in each direction, with the specimen pulled 1 mm along both the positive and negative y-axis and 1 mm along both the positive and negative x-axis. No other boundary conditions were applied. The magnitude of displacements for the biaxial tensile specimen is presented in Figure 5.9.

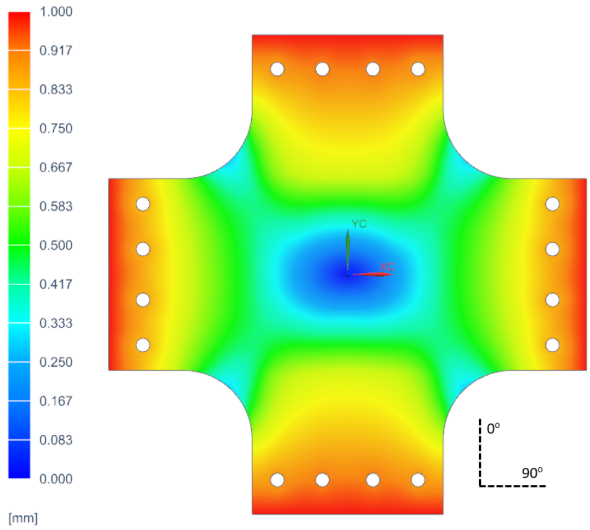

Figure 5.9: Displacement magnitude for the biaxial tensile specimen

Under this displacement-controlled loading, the Hashin criterion was evaluated for all four failure modes to determine failure based on the Failure Index (F.I.), with failure occurring if F.I. exceeds 1. The reaction (tensile) forces resulting from this loading were extracted from post-processing for both x- and y- directions, and the respective tensile failure loads were calculated based on the largest value of the F.I., as in the case of the uniaxial tensile specimen. Thus, for the biaxial (and also for the semi-biaxial) specimen, the total tensile failure load is divided in two components; one in x- direction and one in y- direction.

It was mentioned previously that a 2 mm thick GFRP plate was added outside the CFRP laminate (on top of ply 7 and below ply 1) to reinforce the specimen's arms, reduce stress concentrations in the fillet areas, and shift the failure location to the specimen's center. This GFRP plate is made of unidirectional glass fibers and was placed oriented at 0° (along the y-axis). Therefore, although the CFRP laminate consists of three 0° plies and four 90° plies, the two GFRP plates (2 mm thick each) that are oriented at 0° would make the total structure stronger in the 0° (y-) direction. Hence, the tensile failure load is expected to be larger in this direction. In the following sections, the FEM results for the baseline and gap specimens will be presented and analyzed.

5.2.1. Baseline specimen results

For the arbitrary 1 mm displacement along both positive and negative x- and y- directions that was imposed on the baseline specimen, it was revealed during post-processing that the reaction tensile forces were: $F_x = 100.4$ kN and $F_y = 123.5$ kN. However, these are not the FPF tensile loads, as the analysis showed that for the imposed displacement, the maximum value of the Hashin criterion was: $F.I. = 2$. Thus, in order to find the FPF loads in the x- and y- directions, the above values for the forces must be divided with the value of the maximum F.I., giving therefore the following estimates for the FPF tensile loads of the baseline specimen: $F_x = 50.2$ kN and $F_y = 61.75$ kN. This proves the assumption that the failure load would be larger in the y-direction.

Concerning the failure mode predicted by the Hashin criterion, the analysis showed a tensile matrix failure. The failure was located at the center of plies 2, 3, 5 and 6 (plies oriented at 90°) and occurred almost simultaneously, as the values for the F.I. in all these plies were almost identical. If the mathematical formulation of this failure mode is once again examined:

$$F.I. = \frac{(\sigma_{22} + \sigma_{33})^2}{Y_T^2} + \frac{\tau_{23}^2 - \sigma_{22}\sigma_{33}}{S_{23}^2} + \frac{\tau_{12}^2 + \tau_{13}^2}{S_{12}^2} < 1 \tag{5.6}$$

it can be seen that the transverse and out-of-plane stresses σ_{22} and σ_{33}, along with the shear stresses τ_{12}, τ_{23} and τ_{13} compose the F.I. calculation. Focusing on ply 5, the FE analysis showed that at the failure location, the shear stresses, as well as σ_{33} are basically zero. This means that the dominant stress component to determine failure is σ_{22}, which is the stress component perpendicularly to the fiber direction. In Figure 5.10, the peak transverse stress can be observed in the center of ply 5, which is the location of failure.

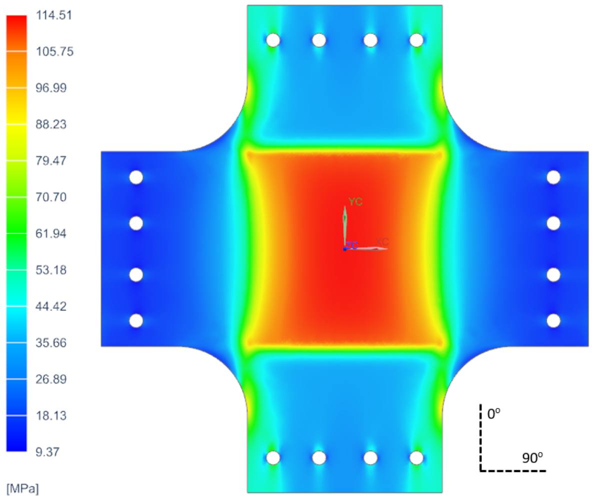

Figure 5.10: Distribution of σ_{22} in ply 5 of baseline specimen for a biaxial tensile displacement of 1 mm

Thus, it can be concluded that the baseline biaxial tensile specimen fails almost simultaneously at plies oriented at 90° (along the x-axis) due to excessive transverse stress at the center of these plies, leading to tensile matrix failure according to the Hashin failure criterion. In essence, a tensile matrix failure due to transverse stress refers to the breakdown of the polymer matrix material (matrix cracking) that binds the fibers together, caused by stresses acting perpendicular to the fiber direction. This failure mode is usually not easy to be identified experimentally, as matrix cracking could be initiated and propagated slowly, allowing for the material to withstand further loading after the estimated First Ply Failure load. Thus, suitable non-destructive testing (NDT) and monitoring methods should be used in order to assess the actual level of damage, when the tensile experiment is carried out. Specifically, monitoring efforts should focus on detecting and tracking the initiation and growth of matrix cracks, and identifying signs of delamination that may follow matrix cracking. More details about damage monitoring and suitable NDT techniques will be discussed in Section 5.4.

Apart from the stress components analyzed above, which are ultimately the ones that cause tensile matrix failure, the normal stress component parallel to the fibers (σ_{11}) in ply 5 is also presented below (Figure 5.11). It can be seen that in the failure area (center of the ply), the stress magnitude is around 900 MPa, well below the relevant tensile strength of the material (2207 MPa), showing that the ply is capable of withstanding a much larger load in the fiber direction, and therefore that σ_{11} is not the dominant stress component for failure.

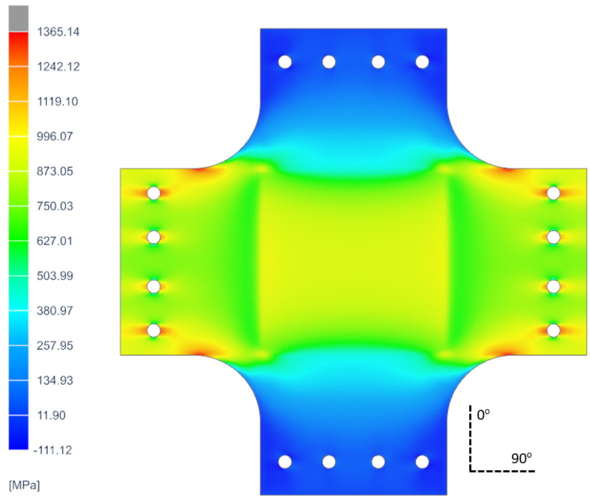

Figure 5.11: Distribution of σ_{11} in ply 5 of baseline specimen for a biaxial tensile displacement of 1 mm

5.2.2. Gap specimen results

The gap specimen for the biaxial tensile test was also subjected to the same type of displacement-controlled loading: 1 mm tensile displacement along both positive and negative x- and y- directions. The reaction forces due to this loading were: $F_x = 101.2$ kN and $F_y = 124.2$ kN. Again, a calculation of the Hashin criterion based on the stress condition under this loading revealed a maximum $F.I. = 2.4$. which means that the FPF tensile loads can be estimated at: $F_x = \frac{101.2}{2.4} = 42.2$ kN and $F_y = \frac{124.2}{2.4} = 51.8$ kN. These values are approximately 16% lower than the respective failure tensile loads calculated for the baseline panel, something that again showcases the negative impact of the gaps in the tensile strength of the laminate, even in biaxial tension.

The Hashin criterion calculations indicate that the failure mode is tensile matrix failure, with ply 3 and ply 5 — plies adjacent to the gap layer — failing first, almost simultaneously. The failure location can be found at the ply areas exactly above or below the gaps, and more specifically towards the wider end of the gaps. This observation is in line with the failure location of the uniaxial tensile specimen, although this time, it is not the in-plane shear stress that dominates the failure behaviour, but rather the transverse stress. The same explanation as before can be given more or less; when the axial load (in y-axis) encounters the gaps in ply 4, due to a sudden stiffness reduction, it has to be rerouted, both around the gaps in the same ply, but also through the adjacent plies. Since ply 4 consists of plies oriented at 0° (with low level of steering in the gaps area and thus negligible deviation from 0°), the extra load is effectively transferred through the steered tows, as their load-bearing capacity is highest at 0°. On the contrary, plies 3 and 5 are oriented at 90°, thus, any excess axial loading cannot be transferred successfully by these transverse plies, resulting in transverse stress concentration and therefore in matrix failure due to exceeding the transverse strength of the material. The distribution of σ_{22} in ply 5 for the 1 mm tensile displacement can be visualized in Figures 5.12 and 5.13, where the failure location above the wider end of the gaps is clearly marked by the peaks of σ_{22}. The distribution of σ_{11} in ply 5 for the 1 mm tensile displacement is also presented in Figure 5.14, where it is again clear that in the failure locations, the maximum σ_{11} (around 1000 MPa) is less than half of the material's tensile strength (2207 MPa). This is another observation supporting the predicted tensile matrix failure mode, since the fibers are capable of carrying more than twice the current load. Note that even the stress concentrations occurring in the corners and around the holes for the bolts are well bellow the allowable limit.

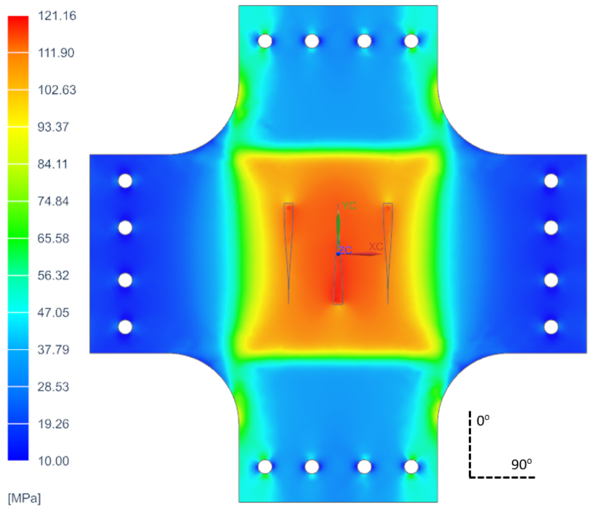

Figure 5.12: Distribution of σ_{22} in ply 5 of gap specimen for a biaxial tensile displacement of 1 mm

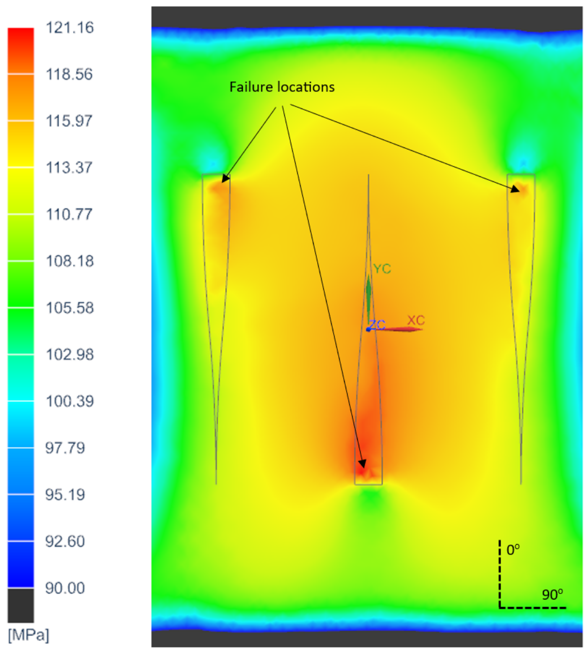

Figure 5.13: Distribution of σ_{22} in ply 5 of gap specimen for a biaxial tensile displacement of 1 mm (zoom)

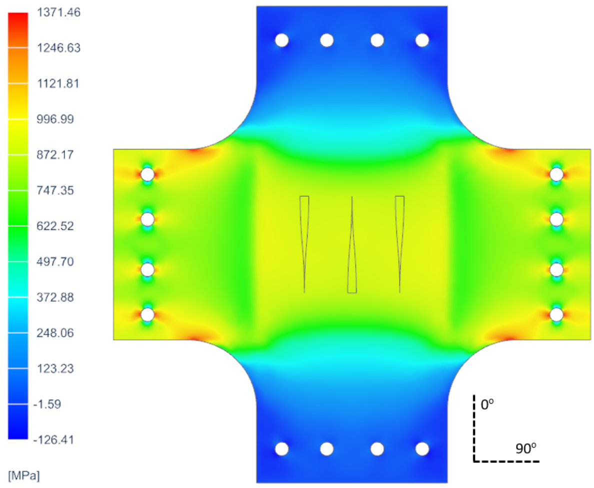

Figure 5.14: Distribution of σ_{11} in ply 5 of gap specimen for a biaxial tensile displacement of 1 mm

5.3. Semi-Biaxial Tensile Specimen

The FEM results for the semi-biaxial tensile specimen are presented and discussed in this section. First, it is essential to emphasize the key difference between this specimen design and the pure biaxial one. In this design, a displacement-controlled loading is applied only in the y-direction, with the top and bottom arms pulled equally, while the left and right arms remain fixed, simulating a clamped condition. The displacement magnitude was again chosen arbitrarily to be 1 mm, and the failure loads were estimated in the same way as described above. The displacement magnitude of the semi-biaxial specimen is presented in Figure 5.15. The process of calculating the FPF loads in x- and y- directions is the same as in the biaxial tensile specimen, therefore the reader is referred to Section 5.2 for a detailed description.

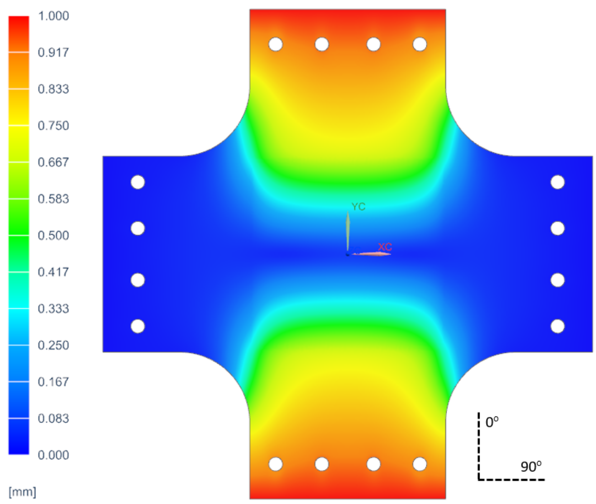

Figure 5.15: Displacement magnitude for the semi-biaxial tensile specimen

5.3.1. Baseline specimen results

For the baseline specimen, the semi-biaxial tensile specimen under the specified loading and boundary conditions exhibited reaction forces of $F_x = 9.9$ kN and $F_y = 113.6$ kN. Evaluation of the Hashin criterion showed a maximum $F.I. = 1.46$, with the failure mode again being tensile matrix failure. Thus, the FPF loads can be estimated as: $F_x = \frac{9.9}{1.46} = 6.8$ kN and $F_y = \frac{113.6}{1.46} = 77.8$ kN.

The analysis predicted that, as in the pure biaxial case, plies 2, 3, 5 and 6 (oriented at 90°) fail first almost at the same time. Plies 5 and 6 seem to fail slightly earlier than plies 2 and 3, but the difference in the calculated Failure Indexes was almost negligible (less than 0.5%) , therefore it is assumed that all these four plies fail simultaneously. The failure was located again in the center of these plies, as can be seen in Figure 5.16.

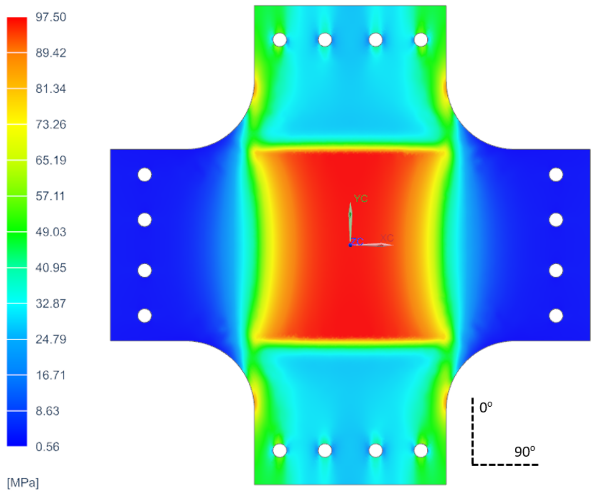

Figure 5.16: Distribution of σ_{22} in ply 5 of baseline specimen for a semi-biaxial tensile displacement of 1 mm

In terms of the type of failure predicted, the same behaviour as in the biaxial tensile specimen was observed. Essentially, the specimen will again fail due to excessive transverse stress in the center of the plies oriented along the x-axis, resulting in tensile matrix failure. Also, Figure 5.17 presents the distribution of σ_{11} in ply 5 of the baseline specimen, where a compressive stress is observed in the center of the ply (failure location), not exceeding 100 MPa in magnitude, while the rest of the ply experiences a tensile normal stress. In any case, the maximum stress magnitude is around 5% of the material's strength, showing again that σ_{11} does not affect the failure behaviour in this case.

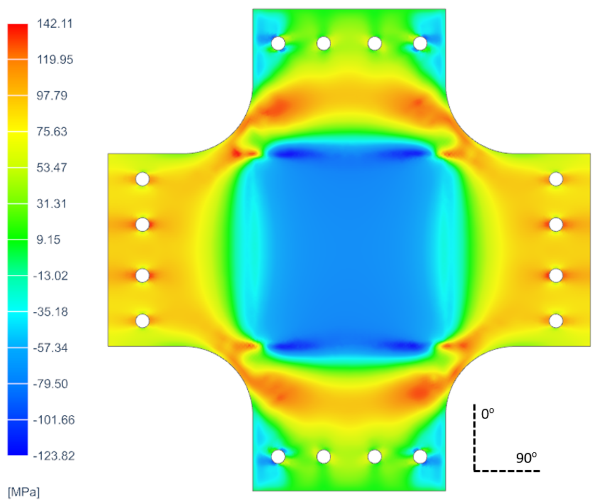

Figure 5.17: Distribution of σ_{11} in ply 5 of baseline specimen for a semi-biaxial tensile displacement of 1 mm

5.3.2. Gap specimen results

The FEM results for the gap specimen showed reaction forces of $F_x = 10$ kN and $F_y = 114.2$ kN under the same displacement-controlled loading and boundary conditions, nearly identical to the reaction forces of the baseline panel. The maximum Hashin Failure Index again indicated tensile matrix failure in plies 3 and 5 (adjacent to the gap layer), with $F.I = 1.8$. This means that, following the same procedure as before, the estimated FPF loads are: $F_x = \frac{10}{1.8} = 5.5$ kN and $F_y = \frac{114.2}{1.8} = 63.4$ kN. These failure loads are 19.1 % and 18.5 % lower than the respective loads in the baseline semi-biaxial specimen. For the sake of simplicity, and in order to refer to a singular value for the strength knockdown, the average between these two strength reductions is taken at 18.8%. Hence, it is proven that the tow-drop gaps created in the context of this thesis have detrimental effects on the tensile strength of all the cases investigated: uniaxial, biaxial and semi-biaxial tension.

As before, the failure location in the semi-biaxial tensile specimen was predicted to occur just above (ply 5) or below (ply 3) the wider end of the central gap. Figures 5.18 and 5.19 show the σ_{22} distribution in ply 5 of the gap specimen, where the peak in this stress component is clearly visible. Figure 5.20 shows the σ_{11} distribution in ply 5 of the gap specimen, where a quite similar image as the one in the respective baseline specimen (Figure 5.17) can be observed.

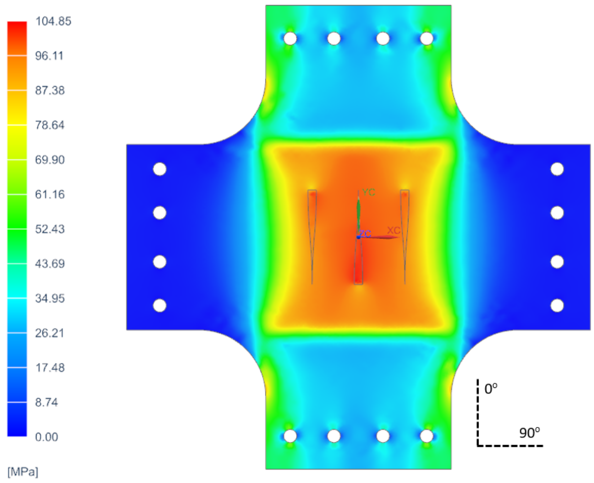

Figure 5.18: Distribution of σ_{22} in ply 5 of gap specimen for a semi-biaxial tensile displacement of 1 mm

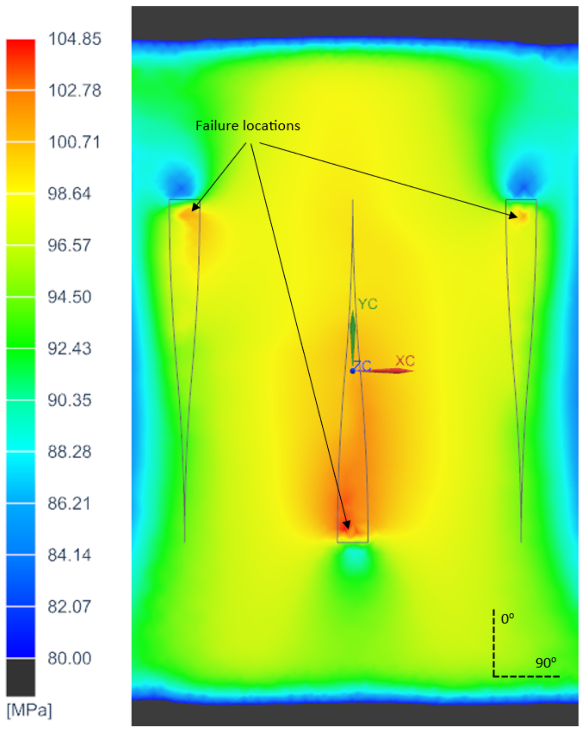

Figure 5.19: Distribution of σ_{22} in ply 5 of gap specimen for a semi-biaxial tensile displacement of 1 mm (zoom)

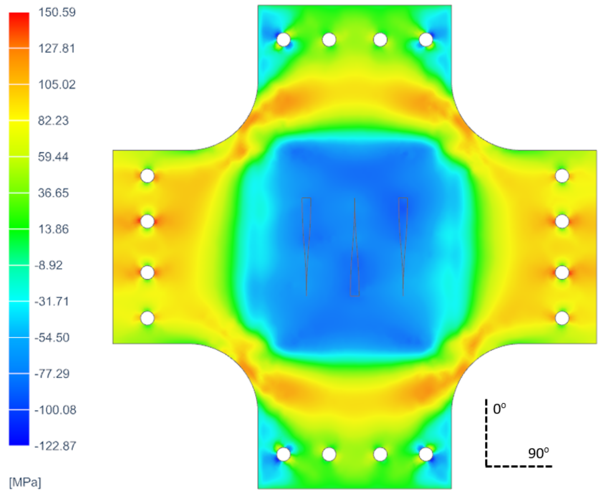

Figure 5.20: Distribution of σ_{11} in ply 5 of gap specimen for a semi-biaxial tensile displacement of 1 mm

5.4. Understanding and identifying failure

So far, the numerical results confirm that failure occurs at specific load magnitudes in both baseline and gap specimens, as well as the fact that tow-drop gaps induced by AFP in a composite laminate have a negative impact on the laminate's tensile strength. The Hashin criterion used in this study identifies four failure types and predicts the load when failure occurs. However, it does not explain the physical implications of each failure mode, such as what happens within the laminate during a specific mode. Additionally, it raises the following question; how can one identify failure? This section aims to address these fundamental issues.

First of all, two different failure modes have been predicted by the Hashin criterion so far: tensile fiber failure and tensile matrix failure.

In the present thesis, as was discussed above, tensile fiber failure was observed in the uniaxial tensile specimen and more specifically in the off-axis plies, oriented at +40° or -40°. Because these plies are not aligned with the direction of the tensile load, they exhibit a relatively low axial stress state in the location of failure, however the shear stresses take up a much larger percentage of the total shear strength capacity, making shear the crucial stress component for failure (see Figure 5.6). The shear stress in this case is the in-plane, or intralaminar shear, τ_{12}. This stress component is the one acting between the different tows composing the ply, and could lead to (matrix) microcracks, fiber-matrix debonding or even fiber rupture. Microcracks are intralaminar matrix cracks that run parallel to the fibers and extend through the ply thickness. Fiber-matrix debonding - which could also lead to microcracks - usually means that the fiber-matrix adhesion is not strong enough, causing premature failure of the laminate due to insufficient load transfer between matrix and fibers. Moreover, fiber fracture occurs when the load-carrying fibers have to bear a higher tensile stress than their respective strength, leading to excessive stretching and ultimate failure (breakage) of the fiber. The final failure of the laminate under tension usually comes gradually, after a specific sequence of the above failure types taking place [59]:

1. Initial micro-damage occurs due to failure at the fiber-matrix interface (fiber-matrix debonding).
2. Micro-damage extends through the ply thickness, marking the onset of meso-damage (microcracking propagation).
3. Multiple meso-damages develop within the same ply, increasing crack density.
4. Local stiffness loss causes stress redistribution to adjacent plies, overloading fibers and resulting in final laminate failure.

This is the damage initiation and propagation sequence that is assumed to take place in the case of the uniaxial tensile specimen, probably leading to final tensile failure due to fiber fracture.

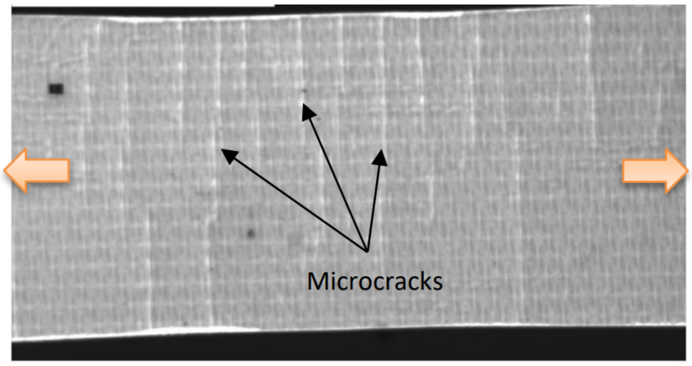

Figure 5.21: Microcracks extending through the ply thickness [59]

On the other hand, the biaxial and semi-biaxial tensile specimens exhibit tensile matrix failure. This is due to the transverse stress in the failure location being higher than the respective transverse strength of the material, and the physical form that corresponds to this type of failure is delamination, which is a crack that occurs between two plies. Damage begins in plies where the fiber orientation is transverse to the load direction, with microcracks forming parallel to the fibers. These microcracks typically grow and spread throughout the plies. When enough microcracks have developed, delaminations (which are essentially cracks) between adjacent plies occur. These delaminations run parallel to the plies, negatively affecting load transfer between subsequent layers and therefore leading to stress redistribution and stress overload of the transverse plies [59]. This explains why failure in the biaxial and semi-biaxial specimens is located in the plies at 90°. The different failure types discussed in this section can be seen in Figure 5.22.

The failure modes predicted by the FE analyses of the discussed specimens closely match those reported in similar cases in the literature. As discussed in Chapter 2, the most common failure types across all studies were matrix cracking and delaminations (particularly in laminate areas with high transverse and shear stresses caused by gaps) and fiber fracture (notably in plies oriented at or near 0°). The alignment between literature observations and this study's results supports the reliability of the FE models developed so far, despite their significant simplifications, such as the omission of fiber waviness.

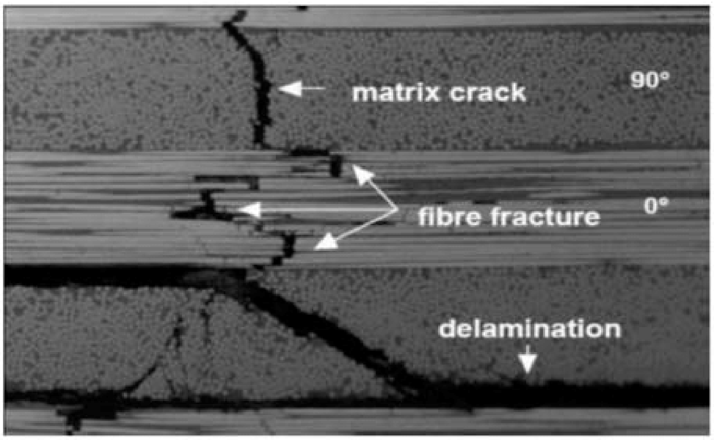

Figure 5.22: Matrix crack, fiber fracture and delamination failure types [59]

Apart from understanding the physical implications of laminate failure, addressing failure identification is also crucial. While this thesis focuses on numerical analysis, experimental validation is needed to confirm the effects of tow-drop gaps. Thus, during tensile (uniaxial, biaxial or semi-biaxial) testing, it is essential to have an accurate way to identify the damage initiation, propagation, and ultimate laminate failure

In uniaxial tensile testing, as mentioned above, the ultimate failure is assumed to occur as fiber fracture. This is typically identified by a distinct snapping or cracking sound, indicating fiber breakage, along with a sharp decrease in tensile load. Hence, it is clear that the tensile fiber failure mode predicted by Hashin for the uniaxial tensile specimen is relatively straightforward to be identified. Note that the predicted tensile loads in Section 5.1 represent first-ply failure loads. Final failure during testing is expected at slightly higher loads, as additional fibers beyond just those in the initial failure location must be fractured to cause total laminate failure.

The situation regarding failure identification in the biaxial and semi-biaxial tensile specimens is more complicated. Because fiber fracture does not occur, it is much harder, or even impossible to identify final laminate failure empirically (by hearing a distinct sound). This does not mean that matrix cracking or delaminations do not produce any sound. They do, but it is largely inaudible to the human ear and requires specialized equipment to detect. Therefore, other non-destructive testing techniques for damage evaluation are needed. It is important to emphasize that real-time monitoring techniques will be discussed in this section, which would help assess damage evolution during testing, enabling for better predictions of final failure.

One of the most useful methods in this matter would be Acoustic Emission Testing (AET), presented visually in Figure 5.23. This is an in-situ damage assessment method, which monitors acoustic waves produced inside the laminate by the release of energy during microstructural changes, such as matrix cracking [60]. Sensors are placed on the surface of the laminate (external plies), detecting and recording the aforementioned acoustic waves, as they are propagated through the laminate and reach the surface. The frequency of these waves is measured, and based on the frequency magnitude, the damage mechanisms discussed above (matrix cracking, fiber-matrix debonding, fiber fracture and delaminations) can be distinguished. In general, the frequencies detected in AET can range from 20 kHz to 1 MHz [61]. Frequency magnitudes from 120 kHz up to 220 kHz usually correspond to matrix cracking, from 220 kHz to 250 kHz signify delaminations, while frequencies higher than 300 kHz relate to fiber fracture [62]. Frequency magnitudes for fiber-matrix debonding often overlap those of matrix cracking, so it is not always easy to identify the exact type of damage using this technique. These ranges can be slightly different, depending on the type of acoustic emission sensor used, however a general trend is that the detected frequency becomes larger when moving from matrix crack, to delamination, to fiber fracture detection [62], [63], [64]. Hence, it is clear that Acoustic Emission is a valuable non-destructive, in-situ monitoring method, that can be used during tensile testing to evaluate the damage initiation, progression and have better estimations about the final laminate failure, allowing for a validation of the numerical models presented so far.

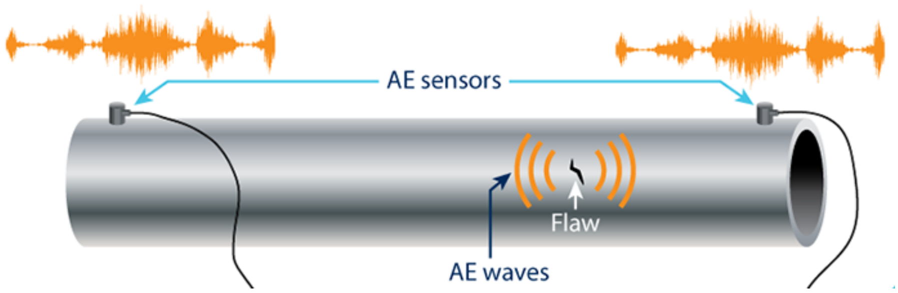

Figure 5.23: Schematic of Acoustic Emission Testing on a pipe [65]

Apart from Acoustic Emission Testing, Ultrasonic Testing (UT) is another NDT method that can be exploited to assess the damage mechanisms taking place during tensile testing of the designed specimens. Ultrasonic Testing is another technique that uses the propagation of ultrasonic waves within the material being inspected. Specifically, UT is an inspection technique that evaluates the interactions (reflection, transmission, or scattering) of pulsed elastic waves in composite structures under examination. Defects, voids, or cracks obstruct ultrasonic waves, causing these interactions, which then can be detected and analyzed to assess the size, location, and extent of the damage. [66], [39]. At first glance, it may appear very similar to AET, however the key difference is that it is an active testing method, meaning that it uses an external energy source, typically generated by a piezoelectric transducer, to create high-frequency ultrasonic waves. On the contrary, AET is a passive technique. Instead of providing energy to the object being examined, it detects and ”listens” to the energy released by the object itself [67]. Ultrasonic Testing can be used in-situ, while performing the tensile tests of the specimens presented in this thesis, by using a coupling medium (e.g., water, gel) between the transducer and the specimen to facilitate wave transmission. Although this poses practical difficulties (maintaining coupling, transducer alignment), it can still provide valuable real-time information about the initiation and propagation of internal damage (delaminations, matrix cracking), caused by gaps.

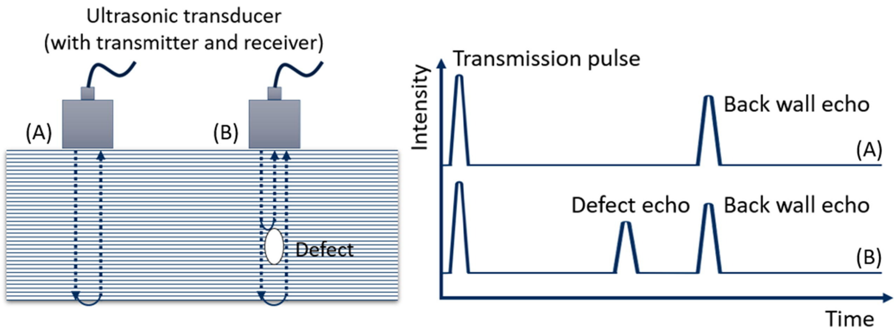

Figure 5.24: Schematic of Ultrasonic Testing [68]

Lastly, another valuable NDT technique that could be used for damage evaluations is Digital Image Correlation (DIC). Digital Image Correlation is a non-contact optical method for full-field measurement of shape, displacement, and deformation [69], [70]. DIC works by capturing digital images of a specimen at different instances and using correlation algorithms to track local displacements, providing quantitative full-field data on displacement and strain development [70]. In the context of this research, DIC could be used to monitor strain distribution and local deformation around regions influenced by tow-drop gaps. By analyzing the strain maps generated during the uniaxial and biaxial tensile tests, it could be possible to identify regions of stress concentration and observe the progression of damage mechanisms in real time. This information could validate the numerical predictions of this thesis and allow for better understanding of the specimens' behaviour under each loading state. However, due to the tow-drop gaps being located within the laminate (and not in its surface plies), DIC may face challenges in directly capturing their effects, as it primarily measures surface deformations. Internal defects may not always induce visible surface deformation unless they cause secondary damage, such as delamination or matrix cracking, that propagates to the outer layers of the laminate. However, since it is strongly suspected that this type of damage will (at least up to a certain extent) be involved in the failure mechanisms of the designed specimens, DIC would still be a useful candidate for non-destructive evaluation.

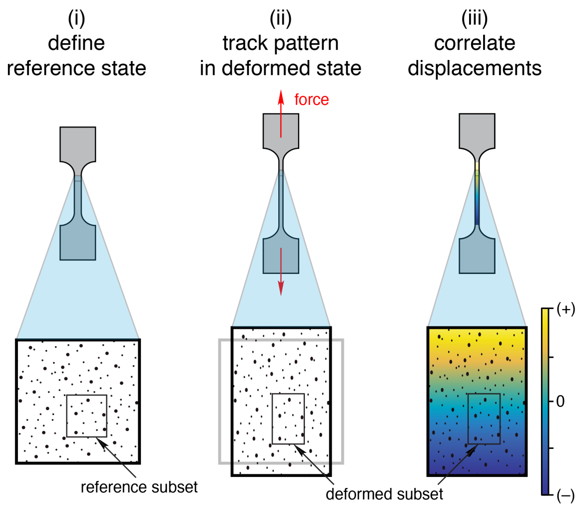

Figure 5.25: Basic principles of DIC [71]

6 Investigating the effect of Fiber Waviness

The results in Chapter 5 are based on a simplified model that does not account for the laminate's actual geometry after curing. Gaps are treated as resin pockets, with no changes assumed in the geometry of the plies above them. However, as discussed in Chapter 2, this does not reflect real-life conditions.

In reality, it has been observed that during curing, a significant level of deformation occurs in the interior of the laminate, especially in the areas around the gaps. As many studies showed [16], [27], [32], [33], [39], [40], [42], prior to curing, the gap is technically an empty void. During curing, under high temperature and pressure, the gap is partially filled with neat resin, while the adjacent ply bends downward to fill the remaining space (Figure 6.1). The rest of the plies above the gap usually follow the same movement, meaning they also exhibit some kind of undulation. In reality, these gap filling mechanisms are very complex, and they have been described and analyzed in detail by [40] and [42]. A simpler approach was used in this thesis to model the fiber deformation thought to be occurring in the discussed specimens, at least to a certain extent.

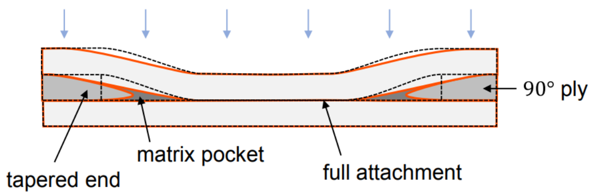

Figure 6.1: Schematic of deformed ply filling the gap, achieving full attachment [27]

In the first stages of the present thesis, it was intended to implement the fiber waviness by following a similar approach to what Nguyen et al. (2021) [33] did. Specifically, it was initially planned to manufacture a set of smaller samples - basically a smaller portion of the gap specimen discussed so far for each case (uniaxial or (semi-)biaxial) - in the size of a rectangular area slightly larger than the gap area. These samples would not be produced for mechanical testing, but they would be sectioned and put under the microscope in order to study the details of the laminate geometry after curing. The microscopy images would be analyzed to recreate the post-cured laminate geometry in and around the gap areas in the FE model. This would involve measuring the deviation angles of each ply from their nominal horizontal orientation to estimate the relevant out-of-plane fiber waviness. Then, the exact geometry would be incorporated into the FEM models for the full-scale tensile specimens, assuming no fiber waviness outside the gap area. These updated FE models for the three cases discussed so far would be ran, and the updated results about the specimens' failure locations and tensile strengths would be obtained, allowing for a comparison with the results of both the baselines and the initial models without fiber waviness. As an initial step, in this thesis, assumptions about fiber waviness levels were made based on relevant literature, and an initial model was developed as a proof of concept for a preliminary comparison with simpler models. This chapter presents this initial approach to account for the fiber waviness in the FE models for uniaxial, biaxial, and semi-biaxial tensile specimens, along with preliminary results on failure type, location, and strength reduction.

6.1. Modelling fiber waviness

The process of creating a FE model that takes into account at least to a certain extent the actual cured laminate geometry is similar for the uniaxial and (semi)biaxial tensile specimens. A lot of simplifications and assumptions had to be taken in this quest, which will be described in the following section.

First of all, it was assumed that only the plies above the gaps would experience some level of out-of-plane waviness as described above. It is reasonable to assume that, because underneath the gaps the plies are intact, there would be no reason for them to deform. However, realistically, it is possible that all the plies in the laminate are deformed (although not to the same extent) since the out-of-plane movement needs to be continuous. This was not taken into account, to reduce the number of plies needed to be modified and therefore reduce complexity of the model and the needed computational time. Therefore, in all the models, plies 1, 2 and 3 were still modelled flat, without any deformation.

The attempt to model the waviness starts with ply 4 and goes all the way up to the top surface of the laminate. To begin with, it is generally assumed that plies 5–7 remain flat for their largest part, bending downwards only in the gap areas to fill the triangular-shaped gaps that were previously considered as neat resin regions. As one can imagine, modelling a continuous ply that bends downwards in the gap area and then upwards again is relatively straightforward for tow-to-tow gaps which are rectangular, but becomes significantly more challenging for tow-drop gaps due to their complex geometry. To simplify the modeling process, each ply was not individually modeled with up-and-down waviness. Instead, the same model as before was used, consisting of seven rectangular plies represented as solid bodies and glued together. However, a key modification was made: in plies 4, 5, and 6, the gap areas were partitioned, and different material properties and orientations were assigned. Note that the term ”gap areas” refers to the triangular-shaped tow-drop gaps, which are actual gaps in ply 4. Similar regions are also defined in plies 5 and 6 to represent the fiber waviness caused by the gaps that are present in ply 4. Apart from these 3 modified plies, ply 7, along with the bottom three plies remained unchanged.

The partitions that were made in the gap areas of plies 4, 5 and 6 represent the fiber waviness that is thought to be taking place in the specimens that were designed. For example, previously, the gap areas in ply 4 were resin pockets containing only neat resin. Now, these areas are divided so that a significant portion represents the section of the adjacent ply bending into the gap. The material in this region is changed from neat resin to the prepreg material, and the material orientation is assigned to be the material orientation of the ply above. The rest of the gap areas in ply 4 are still modelled as neat resin areas. This means that the resin pockets size is significantly reduced.

The same process is repeated for plies 5 and 6. The gap areas in these plies are divided in similar ways as the ones in ply 4, only with the distinction that instead of resin pockets, the respective regions keep the material orientation of the nominal ply. For example, the gap areas in ply 5 are divided into areas of fiber waviness (with the material orientation of ply 6) and areas without fiber waviness (with the material orientation of ply 5). Similarly, the gap areas in ply 6 are partitioned into regions with fiber waviness, assigned the material orientation of ply 7, and regions without fiber waviness, keeping the material orientation of ply 6. This occurs because the ply waviness is assumed to not fully conform to the gap geometry. As the gaps narrow, the bent ply is assumed to eventually curve upward again, marking the end of the waviness region. The area where this transition occurs is assumed to be close to the middle of the gap areas.

The deformed ply geometry is assumed to be wavy, with the ply above the gap layer bending downwards to fill the gap, then curving upwards to exit the gap, similar to the pattern shown in Figure 6.1. The assumption that the deformed ply fills the whole gap comes from the gap size, which is considered large enough for the adjacent ply to reach the bottom. A constant waviness angle of 10° was assumed for the deviation between the ply centerline and the point of maximum deformation, both at the start and end locations of the ply undulation. This assumption is based on Nguyen et al. (2019) [27], which reported a maximum deviation of 10° in their specimens. This value was adopted in the present thesis as a worst-case scenario. The same value for the waviness angle was used to model fiber waviness across all plies, although in reality, this is usually not true, with different waviness levels for different plies being observed (Figure 6.2). Note that in the absence of microscopic observations or more accurate methods to determine the actual level of waviness in the laminate, such assumptions are necessary to assess the impact of ply undulation at a basic level. Nevertheless, as this is a proof of concept, these assumptions were considered sufficient for an initial assessment.

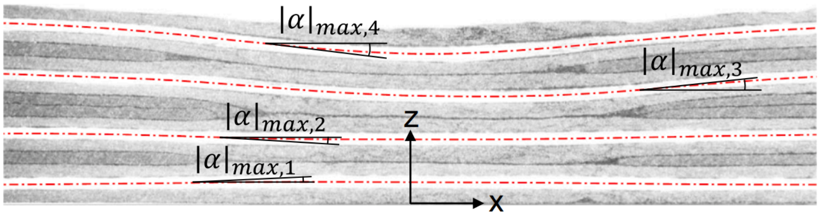

Figure 6.2: Schematic of measurement of different ply waviness angles in different plies [27]

Figures 6.4, 6.5 and 6.6 present the details of the modelling of fiber waviness in the (semi-)biaxial cases, in terms of geometry. Important distinctions in the assumed geometry of the fiber waviness are made between the uniaxial and the biaxial and semi-biaxial specimens. In the uniaxial specimen, because plies 5 and 6 are off-axis, oriented at -40° and +40° respectively, the way the waviness is modelled follows the orientation of these plies. For example, for the waviness in modified ply 4, as can be seen in Figures 6.3, the partitions for the wavy areas and the resin pockets are made along a line inclined at 40° counterclockwise with respect to the y- (horizontal) axis, corresponding to the -40° orientation shown in Figure 4.4. Note that in Figure 6.3, the purple areas represent the portion of ply 5 bending into the gap, while the yellow areas indicate the resin pockets. The sides of the triangular-shaped gap area feature slightly darker yellow strips, indicating resin pockets beneath the bent portion of ply 5. The purple color there is set to be slightly transparent to reveal these resin pockets.

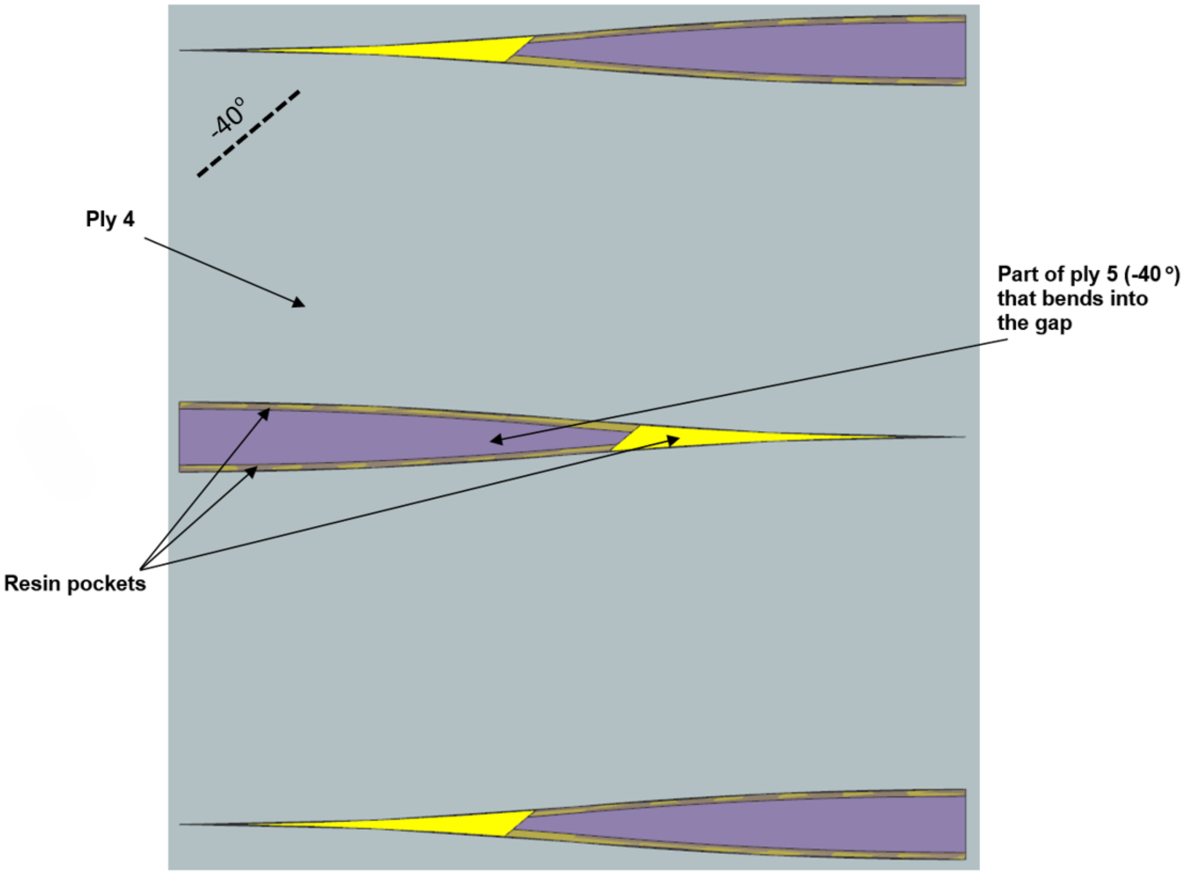

Figure 6.3: Schematic of modified ply 4 (zoomed in gap area). The purple areas mark fiber waviness from the ply above (ply 5 at -40°), while the yellow areas are resin pockets.

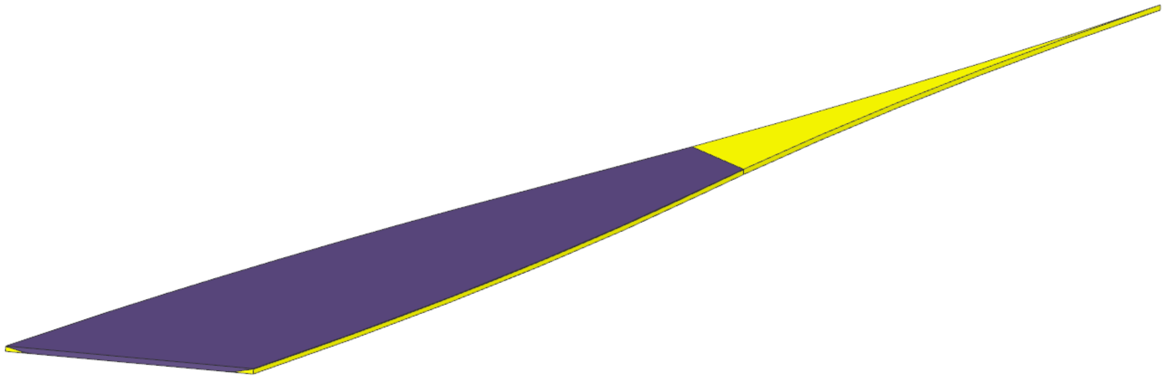

Figure 6.4: View of one of the gap areas in modified ply 4. The purple section marks fiber waviness from the ply above (ply 5 at -40°), while the yellow sections are resin pockets.

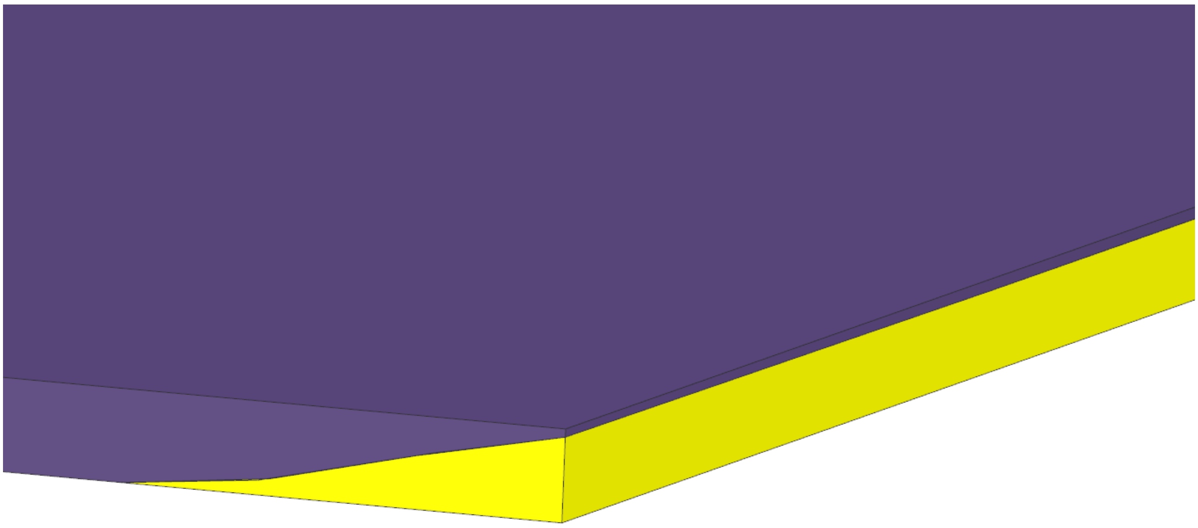

Figure 6.5: Zoomed in view of one of the gap areas in modified ply 4 (back). The purple section marks fiber waviness from the ply above (ply 5 at -40°), while the yellow sections are resin pockets.

Figure 6.6: Back view of one of the gap areas in modified ply 4. The purple section marks fiber waviness from the ply above (ply 5 at -40°), while the yellow sections are resin pockets.

The assumptions about the post-cured geometry of the laminate are made after considering the process of creating the different layers using AFP. As mentioned, the first three plies are laid down flat, with no deformation. After that, the gap layer is created, following the process described in Chapter 4. This leaves three gaps, which initially are basically empty regions, with no material. When the next ply is to be laid down (ply 4 at -40°), it is obvious that the AFP process will place the tows in the respective orientation, but when they encounter the gaps, the tows will be deformed downwards. Because the gap size is sufficient, it is believed that the waviness will be such that the tows of ply 5 will eventually cover the whole gap and will touch the top surface of ply 3, effectively becoming part of ply 4. After covering most of the gap width, the tows are assumed to deform upward, exiting the gap and continuing placement on the top surface of ply 4 to cover ply 5.

It is evident from the laying process that was described above, as well as from Figures 6.4, 6.5 and 6.6 that the empty areas that are left when laying down ply 4 will become much smaller than those in the original, simpler gap model. These areas are empty during layup (essentially being voids), but will be filled with neat resin, due to resin percolation during curing. It is also possible that a certain portion of these regions are filled with resin mixed with some fibers that squeeze in the gap (resin squeeze flow, see [40] and [42]), but in this modelling process only pure resin percolation is taken into account.

The same method is followed for modelling the fiber waviness in the modified ply 5, but this time the relevant partitions are made along a line at 40° clockwise with respect to the horizontal (y-) axis, corresponding to the +40° orientation. The main difference is that no resin pockets are modeled, as ply 5 is not the gap layer. Instead, areas that would be resin pockets in modified ply 4 remain part of ply 5 and are marked in grey. Thus, only the bent portion of ply 6, basically following the waviness of the layer below is modelled (Figure 6.7, marked in purple). The details of the geometry are the same as in the modified ply 4. Note that in Figure 6.7, some areas with the orientation of ply 5 next to the fiber waviness regions are covered by the bent portion of ply 6, and are not clearly visible. For clarification, refer to Figures 6.4, 6.5 and 6.6, which show details of modified ply 4, but a similar view holds for modified ply 5 as well.

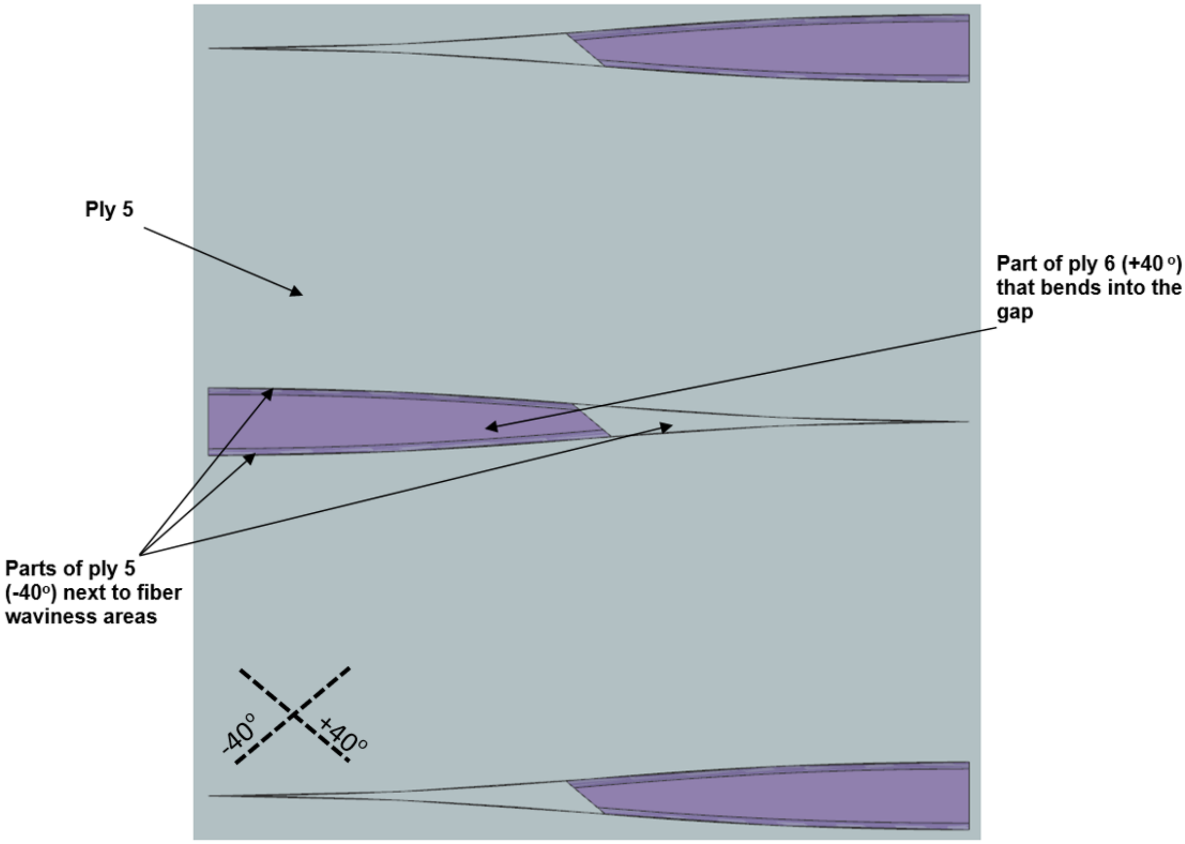

Figure 6.7: Schematic of modified ply 5 (gap area). The purple areas denote fiber waviness from the ply above (ply 6 at +40°), while the grey areas are all part of nominal ply 5 (-40°).

The modelling of fiber waviness for the modified ply 6 is slightly different than previously. Ply 7, which partially bends downward into the gap areas, is oriented at 0°. This could affect the post-cured geometry of the laminate in these areas, leading to slightly different geometry partitions in the model, as can be seen in Figure 6.8. Essentially, while in the cases of modified plies 4 and 5 the waviness was modelled in the -40° or +40° directions respectively, in this case it will be modelled in the 0° direction. A clearer view is presented in Figures 6.9, 6.10 and 6.11 Note that again, the purple section marks the part of bent ply 7 (0°), while the grey sections mark the parts of the nominal ply 6 (+40°). Note that some areas with the orientation of ply 6 next to the fiber waviness regions are covered by the bent portion of ply 7, but are more clearly visible in figures 6.10 and 6.11. These figures present clearly the transition areas between the nominal ply 6 and the part of ply 7 that bends downwards, following the same motion as the adjacent plies.

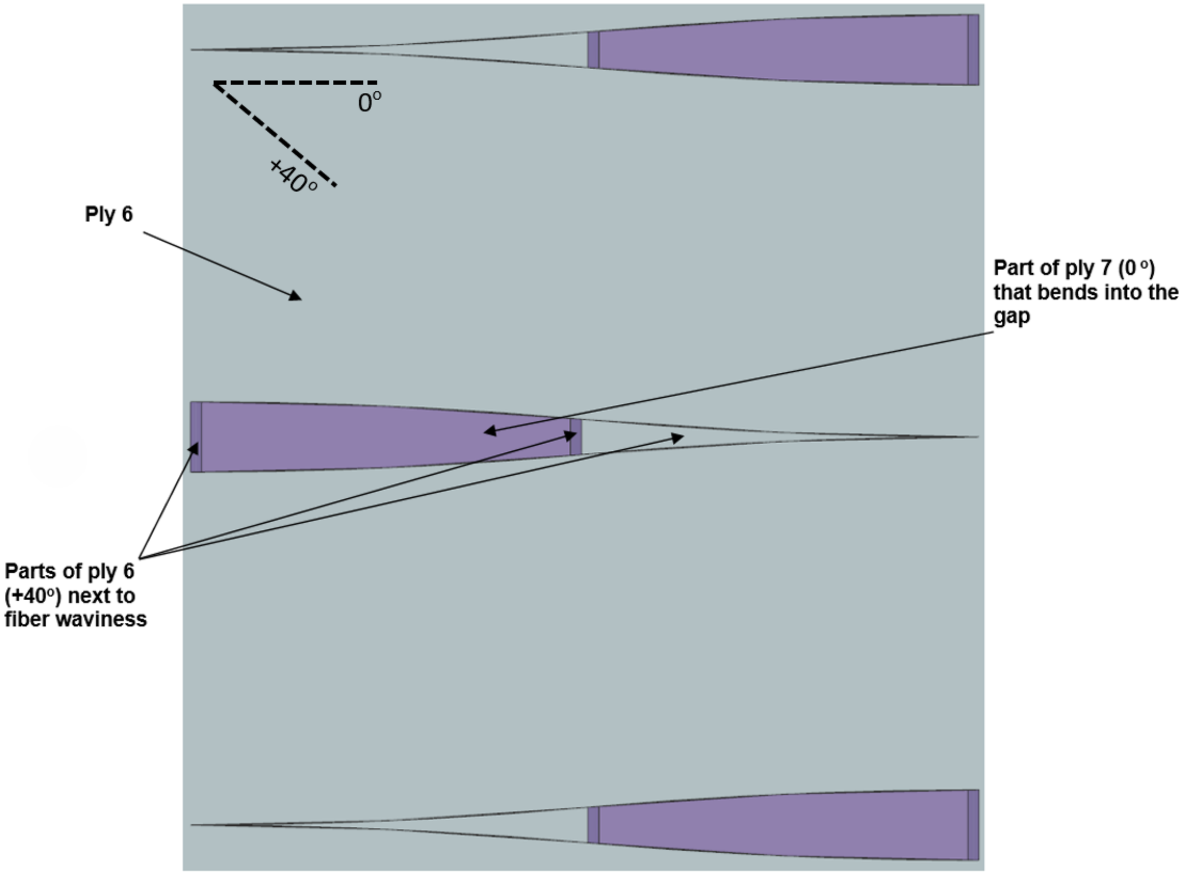

Figure 6.8: Schematic of modified ply 6 (zoomed in fiber waviness area). The purple regions denote fiber waviness from the ply above (ply 7 at 0°), while the grey areas are all part of nominal ply 6 (+40°).

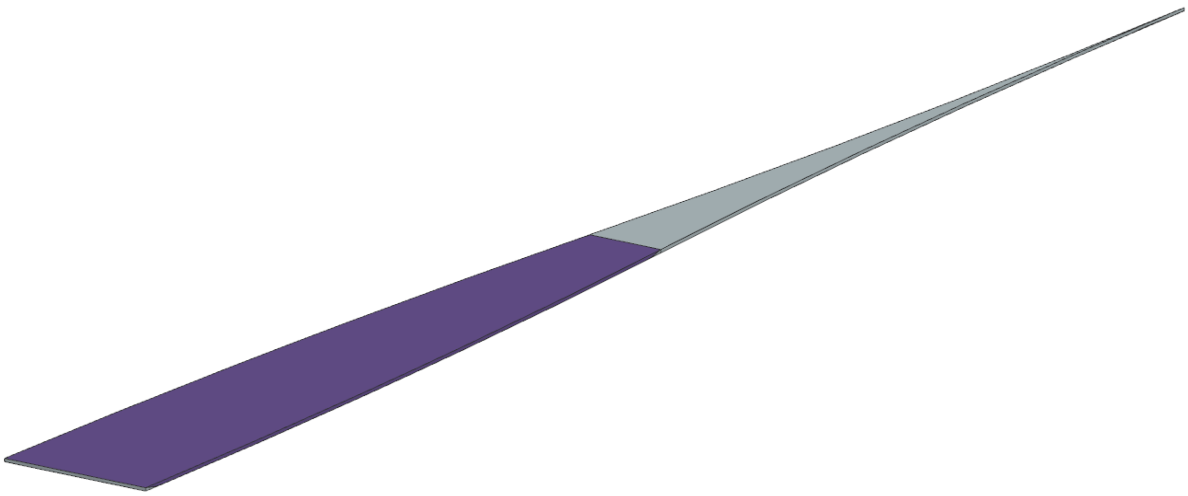

Figure 6.9: View of one of the areas containing fiber waviness in modified ply 6. The purple section marks fiber waviness from the ply above (ply 7 at 0°), while the grey sections are all part of nominal ply 6 (+40°).

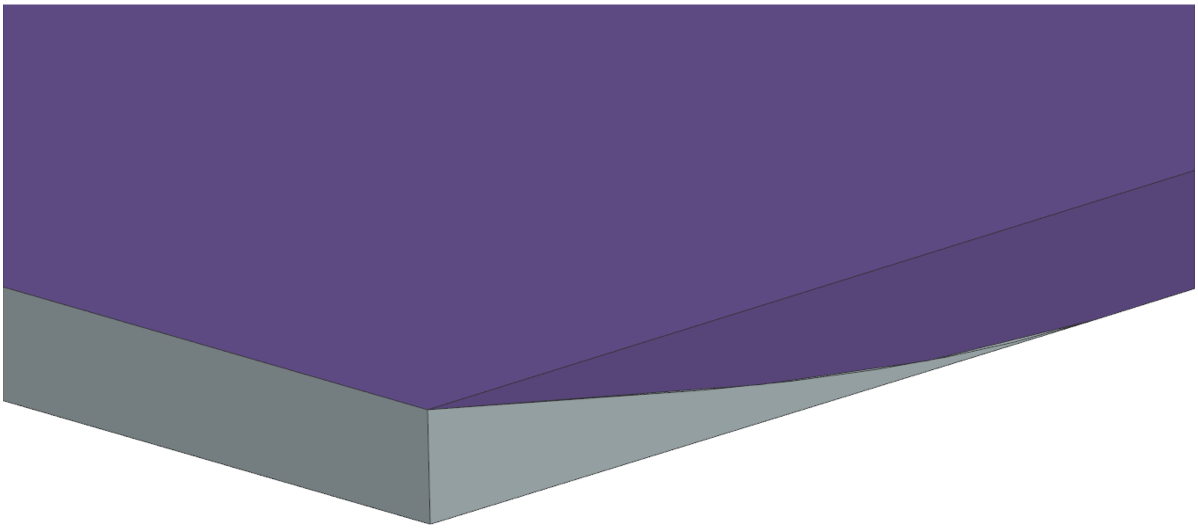

Figure 6.10: Zoomed in view of one of fiber waviness areas in modified ply 6 (back). The purple section marks fiber waviness from the ply above (ply 7 at 0°), while the grey sections are all part of nominal ply 6 (+40°).

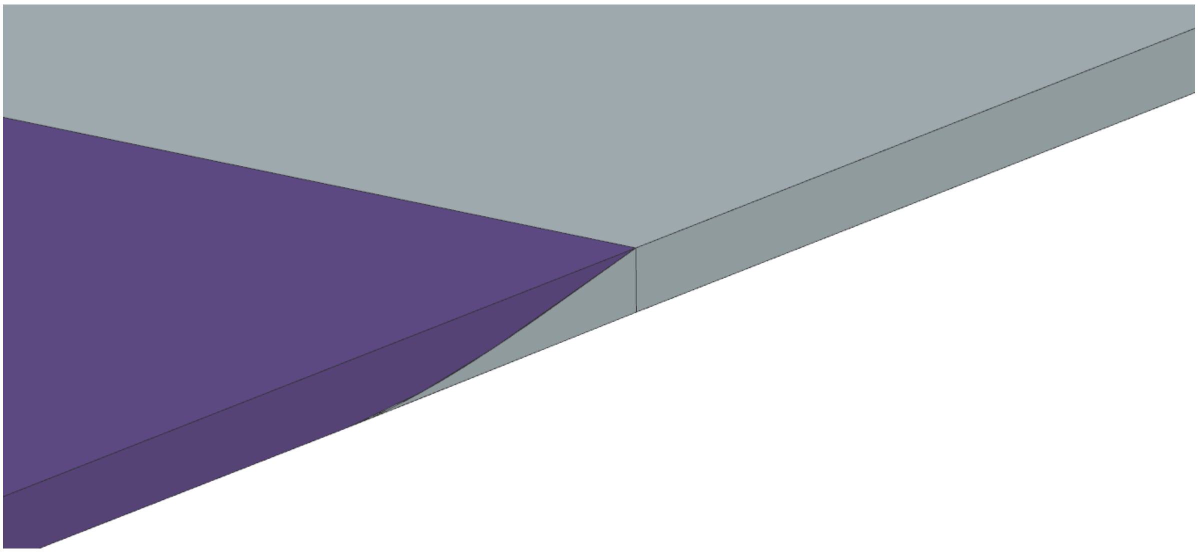

Figure 6.11: Zoomed in view of one of fiber waviness areas in modified ply 6 (middle). The purple section marks fiber waviness from the ply above (ply 7 at 0°), while the grey sections are all part of nominal ply 6 (+40°).

As previously mentioned, plies 4, 5, and 6 in the uniaxial tensile specimen were modified to model fiber waviness, while plies 1-3 and 7 remained unchanged. For ply 7, this results in regions where the local thickness is double the nominal value. This occurs because the unmodified ply 7 remains a rectangular plate with a thickness of 0.13 mm, but sections of the gap areas in modified ply 6 (marked in purple in Figure 6.8) are also considered as parts of ply 7, increasing its total thickness. This simplification was made for a quicker analysis, but in reality, ply 7 is also expected to exhibit some degree of out-of-plane waviness, especially if the curing is carried out without the use of caul plates, as demonstrated by Li et al. (2015) [16].

Apart from the uniaxial tensile specimen, a similar approach for modelling the fiber waviness was followed for the biaxial and semi-biaxial tensile specimens as well. The same process was applied to both cruciform-shaped specimens, as a single model was used for both, differing only in boundary conditions. Therefore, references to the biaxial tensile specimen also include the semi-biaxial specimen in the modeling process description of this section. The results will be presented later separately, as was done in Chapter 5.

One major distinction of the updated biaxial tensile specimen model compared to the uniaxial one was that ply 5 was not modified. This choice was made to gain time during the generation of the model, since plies 5 and 6 are both oriented at 90°. Therefore, it is obvious that using the same method as before, the nominal part of the ply would be at 90°, matching the orientation of the bent portion of the adjacent ply (ply 6), resulting in no change in material orientation. Hence, in the biaxial tensile specimen, only plies 4 and 6 were modified, in a similar fashion as described above.

Specifically, for ply 4, once more the gap areas were partitioned into two different sections: the bent part of the adjacent ply (ply 5 at 90°) which fills the gap and the resin pockets. These two areas are again marked with purple and yellow respectively in Figure 6.12. As the ply above ply 4 is oriented at 90°, its tows are expected to bend downward upon reaching the edge of the gap and bend upward again when exiting the gap. This forms the characteristic resin pockets along the edges of the gap, which merge with the larger resin pocket extending from the middle of the gap to the tip. The assumption about the resin pocket in the narrower part of the gap is based on the gap's geometry. From the middle to the tip, the gap becomes too narrow for the adjacent ply to bend and fill it, leaving space for the resin pocket.

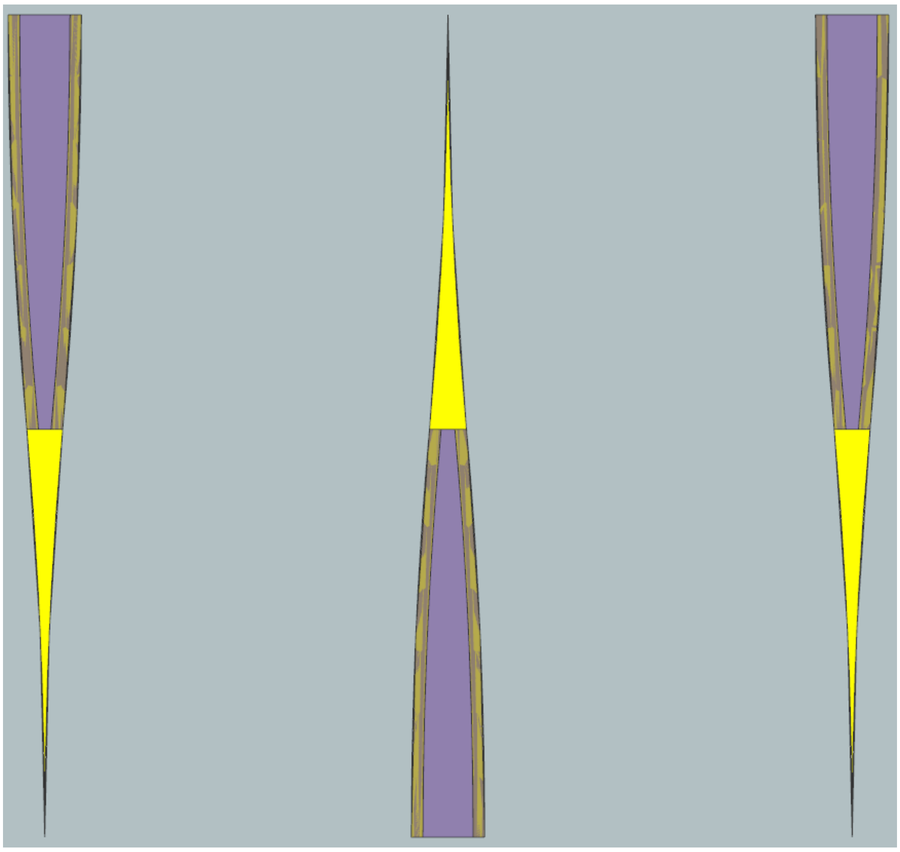

Figure 6.12: Schematic of modified ply 4 (zoomed in gap area). The purple areas denote fiber waviness from the ply above (ply 5 at 90°), while the yellow regions are resin pockets.

The same areas in modified ply 6 were divided into regions using the same geometry as in modified ply 4. Although the adjacent ply (ply 7) is oriented at 0°, meaning the fiber waviness geometry should match that of uniaxial tensile specimen's modified ply 6, the method from biaxial tensile specimen's modified ply 4 was used for quicker model setup and analysis. This is a major simplification, since it accounts for waviness perpendicular to the orientation of ply 7 but ignores the 0° waviness likely present near the bottom edge and middle of the gap. In any case, some degree of waviness is still modeled using this method, and due to time constraints, it was deemed sufficient for drawing initial conclusions. Note that this setup serves as a proof of concept, with a more realistic geometry replication requiring analytical microscopic observations. Figure 6.13 depicts the modified ply 6, with the purple areas again being the parts of ply 7 that follow the out-of-plane deformation of the plies below, and the rest being parts of nominal ply 6.

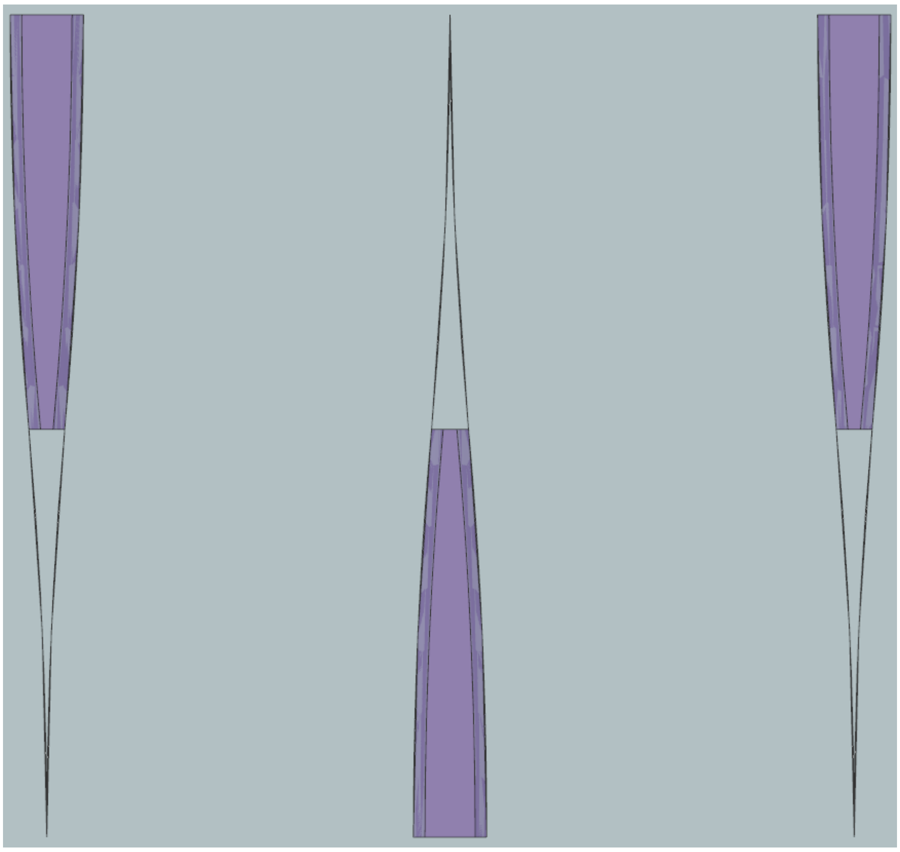

Figure 6.13: Schematic of modified ply 6 (zoomed in fiber waviness area). The purple areas denote fiber waviness from the ply above (ply 7 at 0°), while the grey areas are all part of nominal ply 6 (90°).

6.2. Results

In this section, the results from the FE models of the uniaxial, biaxial and semi-biaxial tensile specimens incorporating fiber waviness will be presented, along with a discussion and comparison with the respective results found in Chapter 5.

6.2.1. Uniaxial tensile specimen

For the uniaxial tensile specimen, after recreating the geometry and assigning the correct material properties in the gap areas of each ply to represent the fiber waviness (as described above), the same process was followed for simulating the tensile experiment. A tensile force of 10 kN was again applied on the right edge of the specimen, which is allowed to move only in the direction of the force, while the left edge was fixed.

In terms of results, first of all the specimen once more failed directly above the gap layer. An important distinction is made in this case regarding the failure location, as the simpler uniaxial specimen without any level of fiber waviness failed at plies 3 and 5 almost simultaneously (with ply 3 being underneath the gap layer). This leads to the conclusion that fiber waviness plays indeed a major role in the specimen failure, as now the ply below the gap layer does not fail at the same time as the ply above it. The exact location is directly above the gaps, again towards the wider end of the gaps, although this time closer to the edge. This is the area where fiber waviness is assumed, with ply 5 adopting the +40° material orientation of ply 6 above it. Essentially, this location is the part of ply 6 (+40°), which bends into the gap.

Numerically, taking into account the Hashin criterion, it was estimated that the failure mode now changed to tensile matrix failure, from tensile fiber failure being the respective failure mode in the simpler model without fiber waviness. The Failure Index in this case was equal to 1.54 in the failure location, leading to a FPF tensile load of: $F = \frac{100}{1.54} \approx 65$ kN, which is almost 55 % lower than the respective FPF tensile load of the baseline (or 42.8% lower than the respective FPF tensile load of the simplified gap specimen model presented in Chapter 5). A much larger tensile strength reduction is noted this time, compared to the one when the model did not account for fiber waviness. The exact level of tensile strength knockdown needs to be reviewed, as such a high increase when implementing fiber waviness at just a first level is considered somewhat unrealistic.

If the relevant mathematical expression is examined again (Equation 5.6), the role of the transverse and shear stress components is evident. The out-of-plane normal stress component σ_{33} is almost negligible in the failure location, while in the same location the transverse stress σ_{22} has a value (35 MPa) slightly lower than half of the total tensile strength of the material in the direction perpendicular to the fibers (81 MPa). Shear in all directions has a major influence in the failure of the specimen, especially in-plane shear τ_{12}, as before. However, in contrast with the simple case that did not account for fiber waviness, in this model relatively high out-of-plane shear stresses are observed as well. The distribution of all shear stress components in the failure locations is presented in Figures 6.14 and 6.15. Note that in some cases the peak stresses have negative values (and thus are marked in blue instead of red), however they always occur in the predicted failure location (right above the gaps, very close to the gaps' wider edge).

To sum up this discussion regarding the uniaxial tensile gap specimen, after making a first attempt to model the fiber waviness that would exist in the actual laminate after curing, it was found that the failure location is almost in exact agreement with the simpler model. Specifically, the areas that failed first were exactly above the gaps, very close to the gaps wider end. However, this area in the simpler model (discussed in Chapter 5), corresponds to the flat ply 5 (-40°), and is exactly above a resin pocket, while in the updated model, it corresponds to the part of ply 6 (+40°) that has bent into the gap. In terms of tensile strength knockdown, a much larger deviation from the baseline was found compared to the simple model, something that proves the negative impact of the waviness combined with the (smaller) resin pockets, as opposed to when the resin pockets were much larger, but waviness was non-existent. The actual level of strength knockdown is worth further investigation, since a knockdown this large (55% contrary to 21.6 % without accounting for waviness) is excessive and contradictory of the literature results.

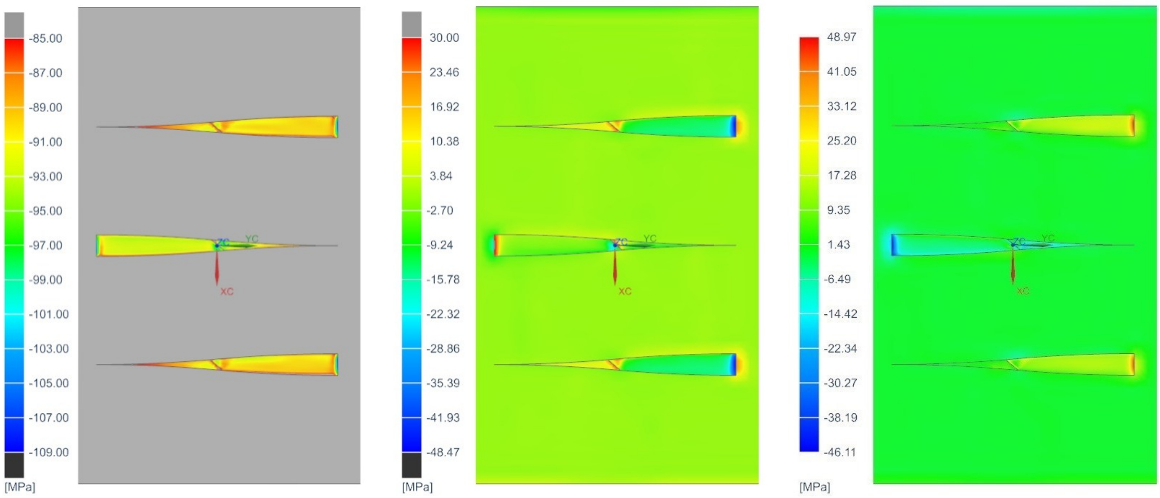

Figure 6.14: Distribution of τ_{12} (left), τ_{23} (middle) and τ_{13} (right) in the failure location, area above gaps, for uniaxial tensile gap specimen containing fiber waviness. Calculated for tensile force = 100 kN.

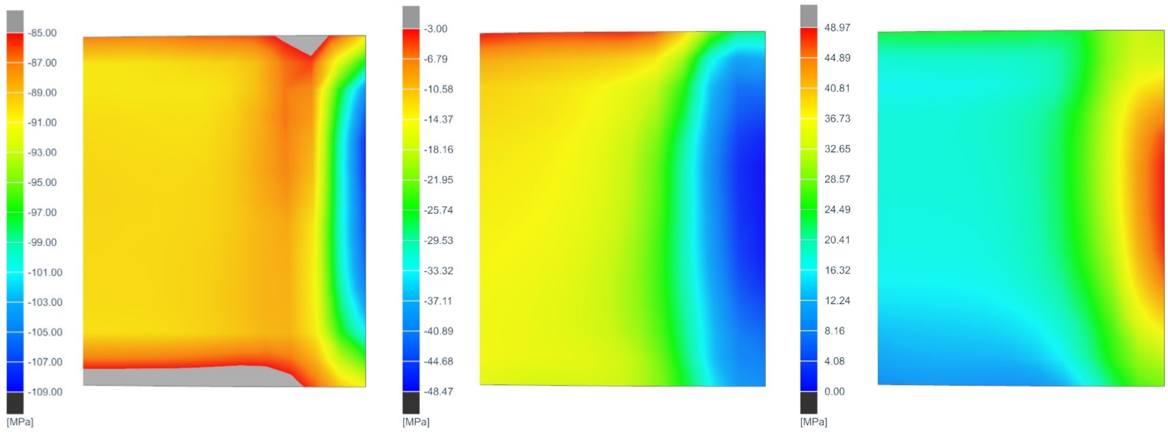

Figure 6.15: Distribution of τ_{12} (left), τ_{23} (middle) and τ_{13} (right) in the failure location, zoomed-in area above top gap, for uniaxial tensile gap specimen containing fiber waviness. Calculated for tensile force = 100 kN.

6.2.2. Biaxial tensile specimen

Regarding the biaxial tensile specimen, the same process for the FE analysis was repeated, but this time the model included fiber waviness. A displacement-controlled tensile loading was applied on the edges of the four arms of the specimen; pulling it in x- and y- directions by 1 mm, simulating a pure biaxial loading case.

The results showed that the applied displacements induced the following reaction forces on the specimen: $F_x = 95.9$ kN and $F_y = 120.2$ kN. The Hashin failure criterion evaluated a maximum $F.I. = 2.45$, indicating again a tensile matrix failure. Therefore, dividing the reaction forces with the calculated maximum failure index gives the estimated FPF loads in x- and y- direction: $F_x = 39.1$ kN and $F_y = 49.06$ kN. The failure load is again higher in y- direction, which makes sense because in total more plies are oriented in this (0°) direction (3 in the CFRP laminate + 2 GFRP plates attached on the outside). These failure loads are 22.1% and 20.6% lower than the respective FPF loads of the baseline in x- and y- direction presented in Chapter 5. As was done before, to simplify, the strength knockdown is represented by the average of the two reductions, calculated at 21.4%. This strength knockdowns is slightly higher than the one estimated without modelling fiber waviness (which was 16%), meaning that oversimplifying the geometry of the gap areas might cause the analysis to underestimate the impact of the gaps slightly.

It was observed that ply 6 (oriented at 90°) failed first, soon followed by ply 5 (also oriented at 90°) with their respective maximum failure indexes being very close (2.45 for ply 6 and 2.4 for ply 5). Note that, as explained above, a ply here refers to the nominal part of the ply combined with the bent portion of the adjacent ply, which bends into the gap or moves in a similar motion, as the plies above the gap bend together. The exact location of failure this time changed slightly, moving from the areas above the wider end of the gaps to the areas in the middle of the gaps. This location essentially corresponds to the location where the waviness of the ply above ends. For ply 5, this is just the location where the nominal ply 5 encounters the bent ply 6 (they are both oriented at 90°), but for ply 6, this is the location where the nominal ply 6 meets the bent part of the adjacent ply 7, resulting in an abrupt stiffness change, as the material orientation switches from 90° to 0°. This could be the reason why ply 6 fails first, as the different oriented plies might be causing a more severe transverse stress concentration that the ones that are aligned.

These observations showcase that even at this first, quite simplified attempt, fiber waviness does play a major role in the final failure of the laminate. In contrast with the uniaxial tensile specimen, where shear is the most important stress component, the transverse normal stress σ_{22} now seems to be the dominant factor for failure, as its value surpasses the relevant strength by a great margin; it reaches 120 MPa, whereas the strength is only 81 MPa (Figures 6.16 and 6.17). The tensile matrix failure mode in the Hashin criterion, as can be seen in Equation 5.3, is also dependent on the shear stresses, however their values are either zero (for τ_{12} and τ_{13}) or under 10% of the total strength $S_{23} = 95$ MPa for $\tau_{23} \approx 7.5$ MPa. This leads to the conclusion that, similar to the gap specimen in Section 5.2, the laminate fails due to excessive transverse stress at the transition area between a bent ply and the adjacent straight ply. The distribution of σ_{11} in ply 6 is also presented in Figure 6.18. This time, contrary to what was presented in Figure 5.14, the magnitude of the normal stress component is much larger, reaching a value of around 1250 MPa in the failure areas. Still, this is quite lower than the material's tensile strength (2207 MPa), resulting in a FI for tensile fiber failure that is lower than the respective for tensile matrix failure in the Hashin criterion calculations.

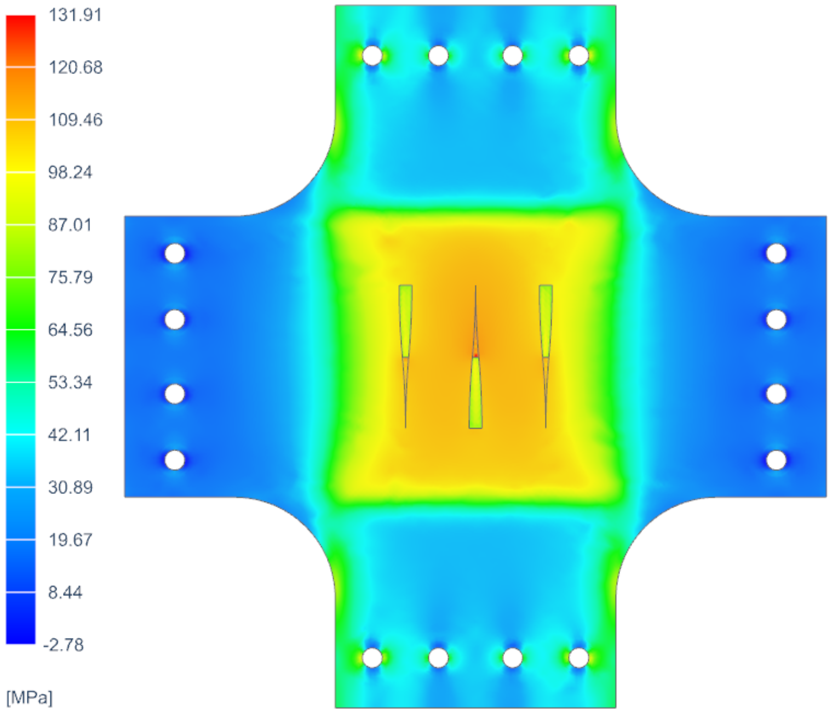

Figure 6.16: Distribution of σ_{22} in ply 6 of gap specimen (including fiber waviness) for a biaxial tensile displacement of 1 mm

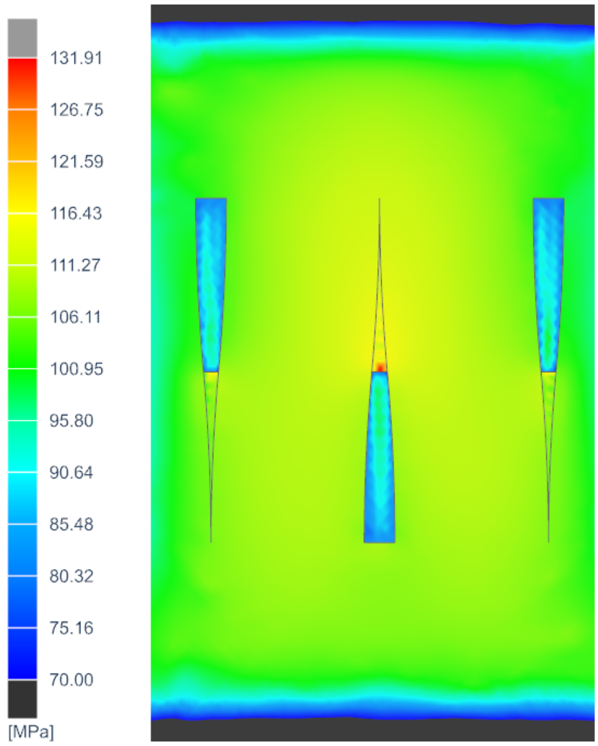

Figure 6.17: Distribution of σ_{22} in ply 6 of gap specimen (including fiber waviness) for a biaxial tensile displacement of 1 mm (zoom)

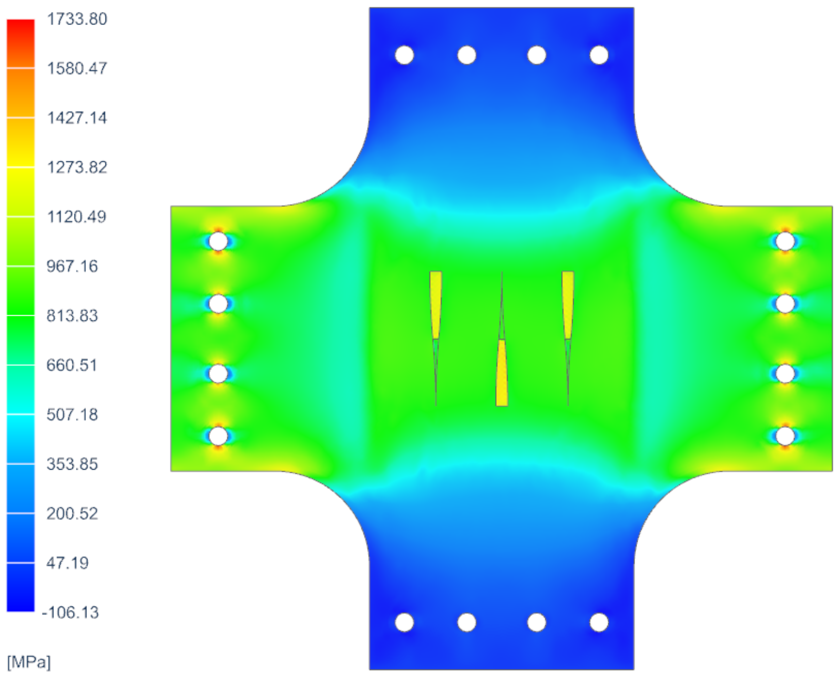

Figure 6.18: Distribution of σ_{11} in ply 6 of gap specimen (including fiber waviness) for a biaxial tensile displacement of 1 mm

6.2.3. Semi-biaxial tensile specimen

The FEA for the semi-biaxial tensile specimen was based on the same model created for the biaxial tensile one, changing again only the boundary conditions. For the relevant boundary conditions of this case (analyzed before), the analysis predicted once more a failure of plies 5 and 6 first, in the same way as in the pure biaxial tensile specimen. Tensile matrix failure was the estimated failure mode, with the Hashin criterion calculating a maximum $F.I. = 1.9$, and the reaction forces were predicted to be $F_x = 9$ kN and $F_y = 111.2$ kN. Therefore, the estimated FPF loads are: $F_x = \frac{9}{1.9} = 4.7$ kN and $F_y = \frac{111.2}{1.9} = 58.5$ kN. These loads are 30.9% and 24.8% lower than the respective FPF loads of the semi-biaxial tensile baseline specimen. Again for simplicity, a single value for the strength knockdown will be used, calculated as the average of the two reductions, resulting in 27.9%. This strength reduction exceeds the 18.8% reduction observed in the simpler model without fiber waviness, highlighting once more the significant impact of fiber waviness on performance.

In terms of failure, the same observations as in the biaxial tensile specimen hold here as well. Failure again occurs first in ply 6, with ply 5 following shortly after. The locations of failure are above the center of the gaps, in the respective area where fiber waviness of the adjacent ply ends. As mentioned above, this is the area where the material orientation changes from 0° to 90° for ply 6, as the bent part of ply 7 (0°), encounters the nominal, non-bent part of ply 6 (90°), resulting in a sudden stiffness change. Peaks of transverse stress are observed in these areas (especially in the center above the middle gap), exceeding again the relevant transverse strength. The σ_{22} distribution in ply 6 can be seen in Figures 6.19 and 6.20. Note that the areas where fiber waviness is modelled (which are considered parts of ply 7 (0°) that is bent downwards) have much lower transverse stresses than in the case of the pure biaxial specimen ($\approx$ 20 MPa contrary to $\approx$ 85 MPa). This is due to the nature of the loading; in the semi-biaxial tensile specimen the displacement-controlled loading acts only in the y- direction (0°), which is aligned with the material orientation in the area where ply 7 is deformed, meaning the fibers in this area can take up the loading effectively. However, in front of the middle of the gap areas, where fiber waviness ends and the material orientation is again 90° (nominal orientation of ply 6), the plies are perpendicular to the loading, creating thus transverse stress concentrations that ultimately lead to failure.

The σ_{11} distribution in ply 6 can also be seen in Figures 6.21 and 6.22. Figure 6.22 is essentialy the same as Figure 6.21, but without showing the bent parts of ply 7 (0°), in order to reveal the stress distribution in the nominal ply 6 (not containing waviness). It is observed that, although in most of the ply area the normal stress is very low in magnitude, the areas featuring fiber waviness show a large stress rise which reaches up to 1400 MPa. This is still lower than the tensile strength of the material, hence why the laminate still fails in the tensile matrix mode. An explanation for the large difference in σ_{11} magnitudes can be given if the fiber orientations are taking into account; the areas in blue colour in Figure 6.21 belong to the nominal ply 6, which is oriented in 90°. However in the semi-biaxial case, the displacement-controlled load is applied in the 0° direction (y- axis), therefore perpendicular to the ply orientation. Hence, these areas cannot withstand almost any of the load. On the other hand, the areas marked in orange/red in 6.21 belong to ply 7, which at this location is bending downwards, following the movement of the plies beneath. Ply 7 is at the same orientation as the displacement-controlled load, thus being able to carry much more load.

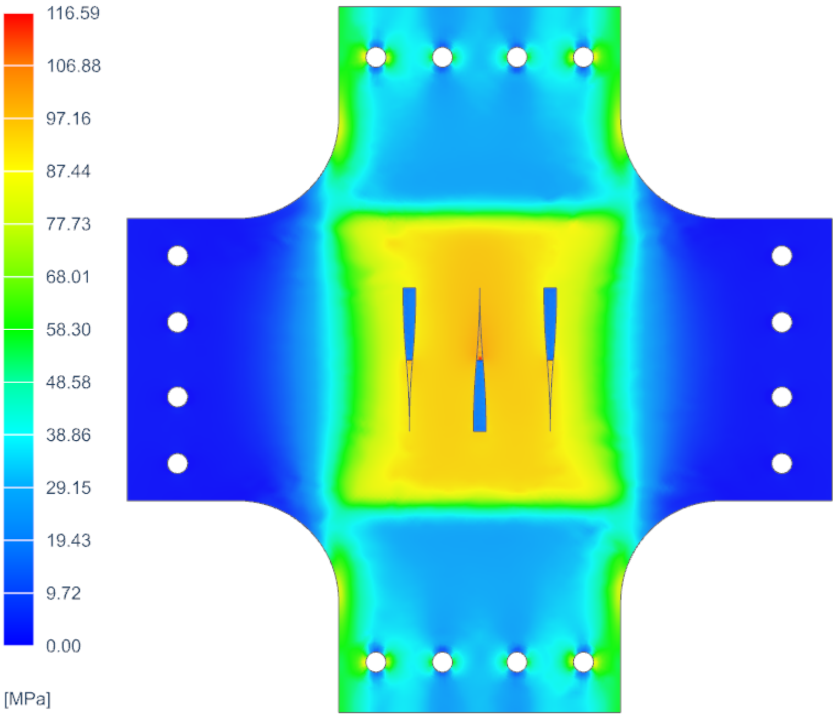

Figure 6.19: Distribution of σ_{22} in ply 6 of gap specimen (including fiber waviness) for a semi-biaxial tensile displacement of 1 mm

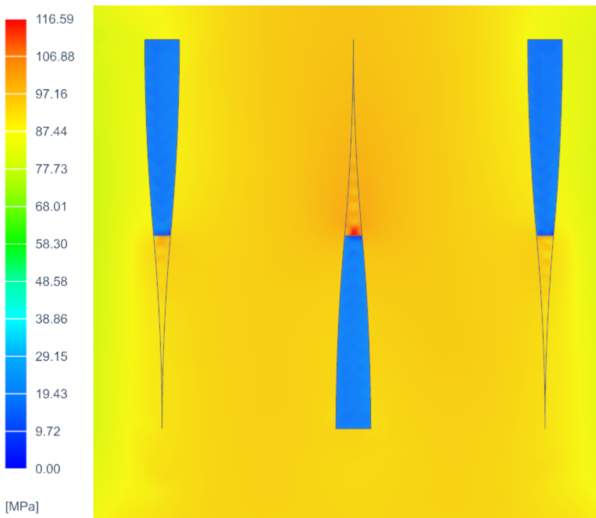

Figure 6.20: Distribution of σ_{22} in ply 6 of gap specimen (including fiber waviness) for a semi-biaxial tensile displacement of 1 mm (zoom)

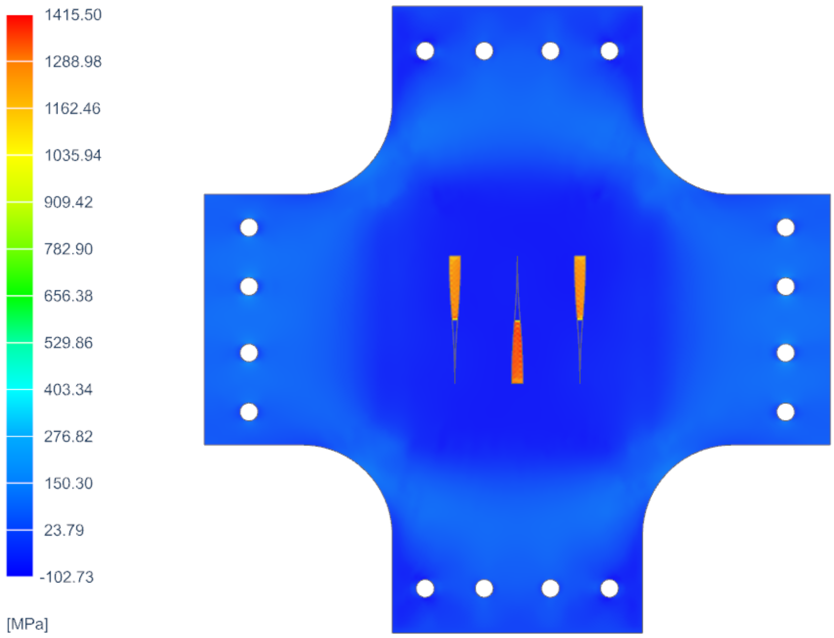

Figure 6.21: Distribution of σ_{11} in ply 6 of gap specimen (including fiber waviness) for a semi-biaxial tensile displacement of 1 mm

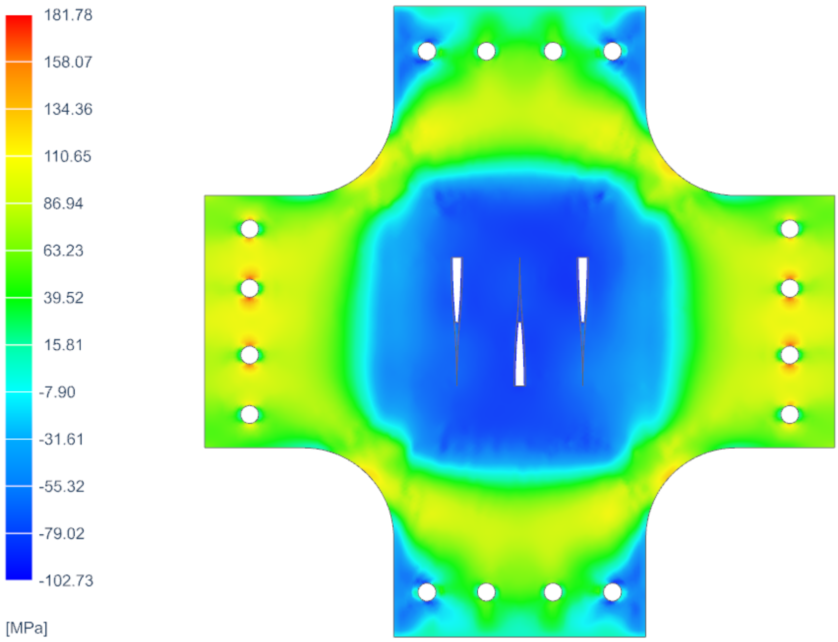

Figure 6.22: Distribution of σ_{11} in ply 6 of gap specimen (not including fiber waviness) for a semi-biaxial tensile displacement of 1 mm

6.3. Limitations of the models

The analysis presented above proved that fiber waviness within the laminates, caused by tow-drop gaps, can significantly reduce their tensile strength, by inducing severe stress concentrations, especially in the transition regions between plies with different material orientations. The tensile strength reduction was estimated to be greater in all cases (uniaxial, biaxial, and semi-biaxial tension) when fiber waviness was taken into account compared to when it was not. However, the exact extent of the strength reduction remains uncertain for the specimens presented in this thesis, due to significant assumptions and simplifications that introduce limitations in the FE models.

First of all, a key simplification involved the geometry of the fiber undulation itself. A constant maximum waviness angle of 10° was assumed and applied in all plies containing some sort of fiber waviness. This is of course not realistic, as different plies are expected to exhibit different levels of undulation. However, this choice was made based on observed data in literature (Nguyen et al. (2019) [27]), as the actual waviness angle was still unknown, since no microscopy examination of the laminate was performed. Also, the fiber undulation was assumed to terminate approximately at the midpoint of the gap areas, or in the corresponding regions above the gaps in the plies located above the gap layer. This assumption was based on the fact that as the tow-drop gaps narrow near their tips, there is thought to be insufficient space for the plies to bend into the gaps. Of course, this assumption is reasonable, however the exact location where this occurs should be determined in a future study aiming to validate the models, using optical microscopy.

In addition, fiber waviness was generally not modeled along the longitudinal direction of the gaps, except for modified ply 6 of the uniaxial tensile specimen, where however no waviness was modelled in the lateral direction. This decision was due to the complicated geometry of such features, which often caused meshing failures. Clearly, replicating the exact geometry of waviness in both longitudinal and lateral directions would create highly complex curvatures in certain areas, such as the wide edge of the gaps, making meshing extremely challenging. Efforts to resolve this required a great mesh refinement, significantly increasing computational time due to very small elements, and often leading to analysis crashes. Therefore, the waviness should be sufficiently simplified, with each ply considering it in only one direction. While this simplification reduced the model's fidelity in capturing the actual conditions, it was considered necessary to ensure the feasibility of the simulations within the available time and using the available resources.

Apart from the above, two additional simplifications were made: fiber waviness was not modeled in ply 5 of the biaxial and semi-biaxial specimens, and ply 7 was modeled flat and at full thickness, resulting in ply 7 locally exhibiting double thickness. The former choice was made because, despite the waviness, both the wavy and non-wavy regions shared the same material orientation and were thus treated as a single ply. The latter choice was made because for a quicker model setup, however it could be considered valid to a certain point, as in laminates cured with the help of a caul plate, the bottom and top plies can indeed be flat, as was demonstrated by Li et al. (2015) [16]. In Figure 6.23 a cut section of their FE model produced using a caul plate can be seen. Note how both the top and bottom plies are flat, and the level of fiber waviness inside the laminate is quite high across all plies. This shows how complicated it really is to make a fully accurate model of a laminate containing gaps, with an implemented extensive fiber waviness, justifying to some extent the simplifications made in the context of this thesis.

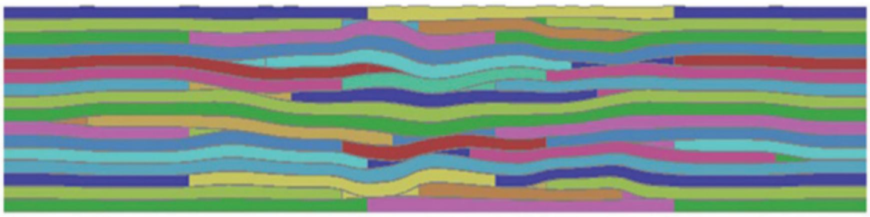

Figure 6.23: Schematic of cut section of FE model for laminate produced with hard tooling (caul plate) [16]

Lastly, another key limitation of the current models is that they focus solely on First Ply Failure (FPF), without incorporating Progressive Damage Analysis (PDA). The current model can determine the onset of damage (the instance of First Ply Failure), but it does not capture the specimen's maximum load capacity, which is more easily measured experimentally and reflects its residual strength. In reality, the specimens would probably be able to withstand higher loads than the FPF loads currently predicted, as the material would redistribute stresses to the undamaged plies, delaying ultimate failure. Without PDA, the model cannot simulate this behaviour and can be seen as conservative. However, because the same principle is applied in both baseline and gap specimens, comparisons between them to derive strength knockdowns can be considered valid. Thus, most of the uncertainty lies in the prediction of the actual failure load magnitude.

6.4. Summary of results

Table 6.1 below summarizes the tensile strength knockdown values predicted in both the initial models (without accounting for fiber waviness) and the updated models (incorporating fiber waviness).

Gap Specimen	**Knockdown - No Fiber Waviness**	**Knockdown - With Fiber Waviness**
Uniaxial	21.6	55
Biaxial	16	21.4
Semi-biaxial	18.8	27.9

Table 6.1: Tensile strength knockdown for different gap specimens compared to the baseline (initial and updated models).

In general, the updated (semi)-biaxial models showed a 5-10% increase in strength knockdown compared to the initial models without fiber waviness. However, the uniaxial case exhibited a significantly larger increase, raising concerns about the accuracy of these results.

In order to determine which strength knockdown values are closer to reality, the already well-discussed studies of Falcó et al. [25], [31] will be revisited. These studies investigated the impact of tow-drop gaps in the tensile strength of laminates, under uniaxial tension using both numerical and experimental approaches. They estimated a 12.5% strength reduction in their FE model, and a 22.1% knockdown when performing the actual tensile test. However, one of their main simplifications in their FE models is that they totally omitted fiber waviness inside the laminate, which in reality occurs due to the presence of the gaps. This leads to the reasonable assumption that this omission is the primary cause of the nearly 10% deviation observed between their simulations and experimental results. The results of the studies from Falcó et al. are thought to be relevant to this thesis, since they cover tow-drop gaps of similar geometry and size, even though certain parameters such as laminate layup, total thickness and gap configuration might be slightly different.

Going back to the results of the present thesis, for the biaxial and semi-biaxial tensile specimens, the deviation between the simpler models and the updated ones (containing fiber waviness) is below 10%. This leads to the conclusion that, based on the previous remark regarding the deviation between simulations and experiments, it can be considered valid. However, for the uniaxial tensile specimen, a significantly larger difference is observed between the models, with the simpler model estimating a 21.6% reduction compared to the 55% reduction predicted by the updated model. This is obviously an unreasonable deviation, possibly due to modelling errors, extensive simplifications, or a combination of the above. A more reasonable strength knockdown value for the uniaxial tensile specimen would range approximately between 22% and 32%, based on the previously established reasoning. In any case, a revision of this particular FE model is deemed necessary for accurate predictions.

In addition, Figures 6.24, 6.26 and 6.28 present in detail all the stress components values, as well as their evolution (from baseline to updated gap specimen containing fiber waviness), for the uniaxial, biaxial and semi-biaxial tensile specimens. These stress values were calculated for the respective applied loading and boundary conditions, in the predicted location of failure. Note that these are not the stresses at the instance of First Ply Failure, however the trends observed in the stress components (increase, decrease, or negligible change) hold in general. The stress magnitudes were then divided with their respective strengths, and the resulting percentages are presented in Figures 6.25, 6.27 and 6.29.

It is clear that in the uniaxial tensile specimen (Figures 6.24), the highest stress in terms of magnitude is the normal stress σ_{11}, followed by the in-plane shear stress τ_{12}. This is something that is observed in all three models (baseline, initial gap specimen and updated gap specimen). However, as explained previously, the in-plane shear stress (τ_{12}) in every case is much closer to the respective in-plane shear strength, which is why it is the dominant factor for failure. This can be seen in Figure 6.25, where the percentages for τ_{12} range from 82% of the total strength in the baseline, to 95.2% in the final gap specimen model. What is interesting in Figure 6.24) is that in the updated models containing waviness (grey bars), the out-of-plane shear stress components τ_{23} and τ_{13} show a quite high rise, reaching 49 MPa, while in the previous models they were either zero (baseline) or quite low (around 3.5 MPa - initial gap specimen without fiber waviness). This means that in the updated model, the out-of-plane shear stresses are now more than half of the respective out-of-plane shear strengths (95 MPa) - Figure 6.25. At the same time, the in-plane shear is also higher, but the degree of increase is much lower (108.5

MPa contrary to 104.7 MPa and 93.5 MPa in the baseline and initial gap specimen models respectively). A large percentage increase can be observed for σ_{22} as well, reaching in the updated model more than 40% of the total transverse strength, while in the baseline and initial gap specimen models it was much lower and showed a descending trend. Thus, the sharp increase in the strength knockdown (55%, whereas in the simpler model this was 21.6%) can be attributed to this sharp increases in the transverse and out-of-plane shear stresses. The exact reason is still unknown, but it is probably due to the simplifications and limitations of the model discussed in Section 6.3. In any case, this needs to be further investigated.

Figures 6.26 and 6.27 present the same stress component evolution (both in absolute magnitudes and normalized) for the biaxial specimen. In this case, especially if one looks at Figure 6.27, it is clear that the main responsible stress component for failure is the transverse stress (σ_{22}), which exceeds the material's transverse strength by a high margin. The normal stress parallel to the fiber direction (σ_{22}) also reaches up to 40 - 43 %, while the rest of the stress components are quite low compared to their strengths. Another remark that can be made here concerns the reasons behind the strength knockdown increase (from 16 to 21.4 % - Table 6.1). This is probably due to the increase of the out-of-plane normal stress (σ_{22}) and the out-of-plane shear stresses (τ_{23} and τ_{13}). The percentages rise to 9.3%, 13.7% and 4.5%, while previously they were either zero (baseline model) or quite lower (simplified gap specimen model). This observation leads to the conclusion that fiber waviness increases the out-of-plane stress components, something reasonable since the definition of fiber waviness in the context of this thesis is the out-of-plane motion of a ply, which tries to fill the tow-drop gaps.

In terms of the semi-biaxial tensile specimen (Figures 6.28 and 6.29), most of the same remarks as for the biaxial tensile case hold as well. A key difference is that the percentage of σ_{11} with respect to the respective strength is largely lower. This observation is logical, since as discussed, failure occurs in modified ply 6, which is oriented in 90°, therefore perpendicularly to the applied displacement. Note again that all the figures below (Figures 6.24 to 6.29) present data in the FPF location, thus in the exact failure location of the first ply that fails. Lastly, τ_{13}, although being out-of-plane, does not seem to affect the strength knockdown increase, something reasonable as it again involves direction 1, which is parallel to the fiber direction.

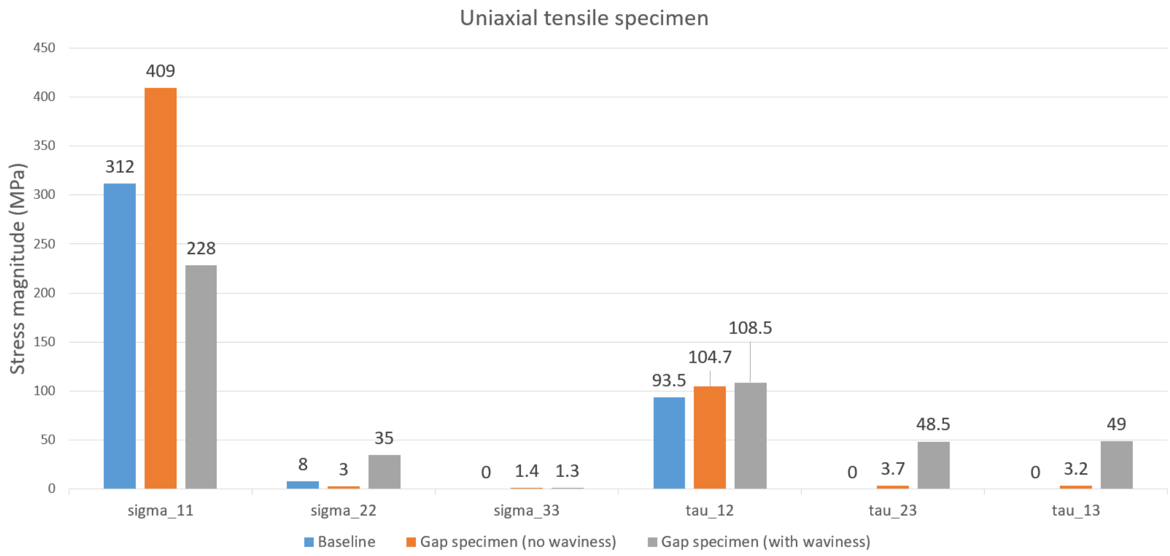

Figure 6.24: Stress components evolution (at the failure location) for the uniaxial tensile specimen and comparison between baseline, and initial and updated gap specimen models

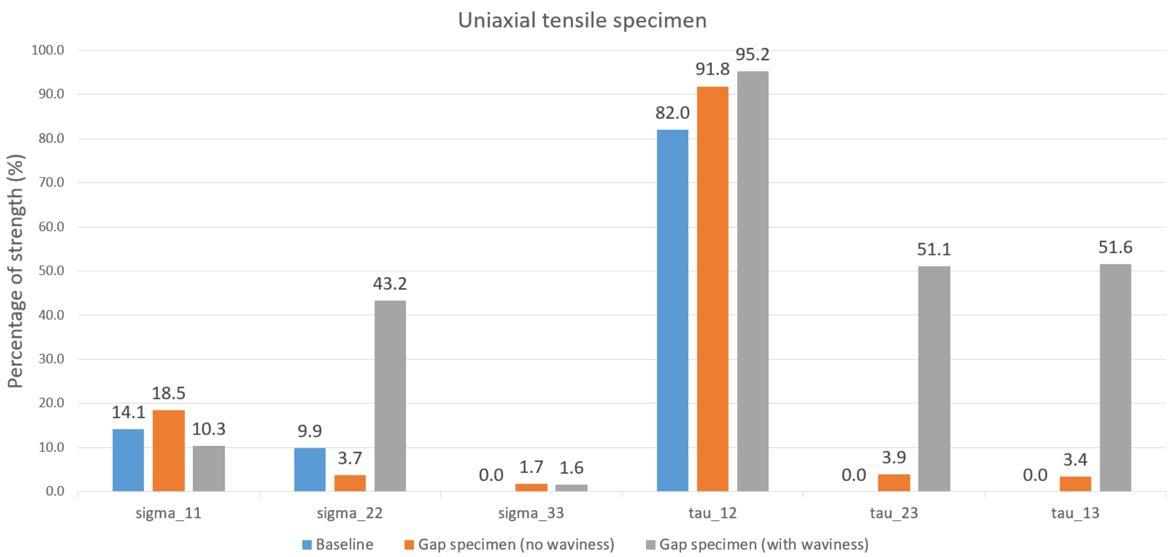

Figure 6.25: Stress components evolution (at the failure location) for the uniaxial tensile specimen and comparison between baseline, and initial and updated gap specimen models (normalized with respect to strength values)

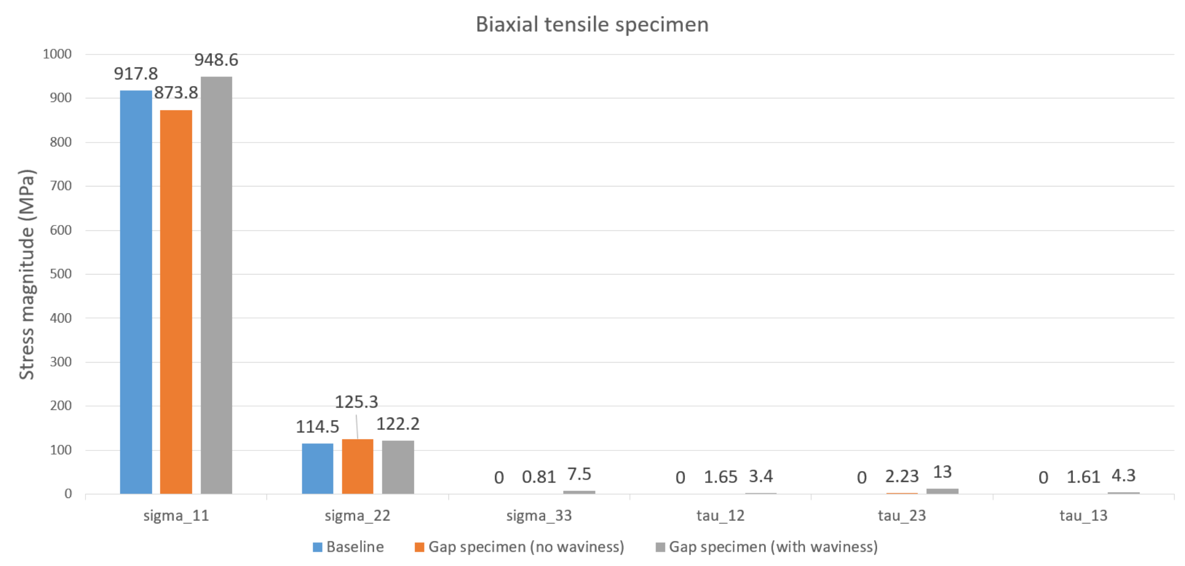

Figure 6.26: Stress components evolution (at the failure location) for the biaxial tensile specimen and comparison between baseline, and initial and updated gap specimen models

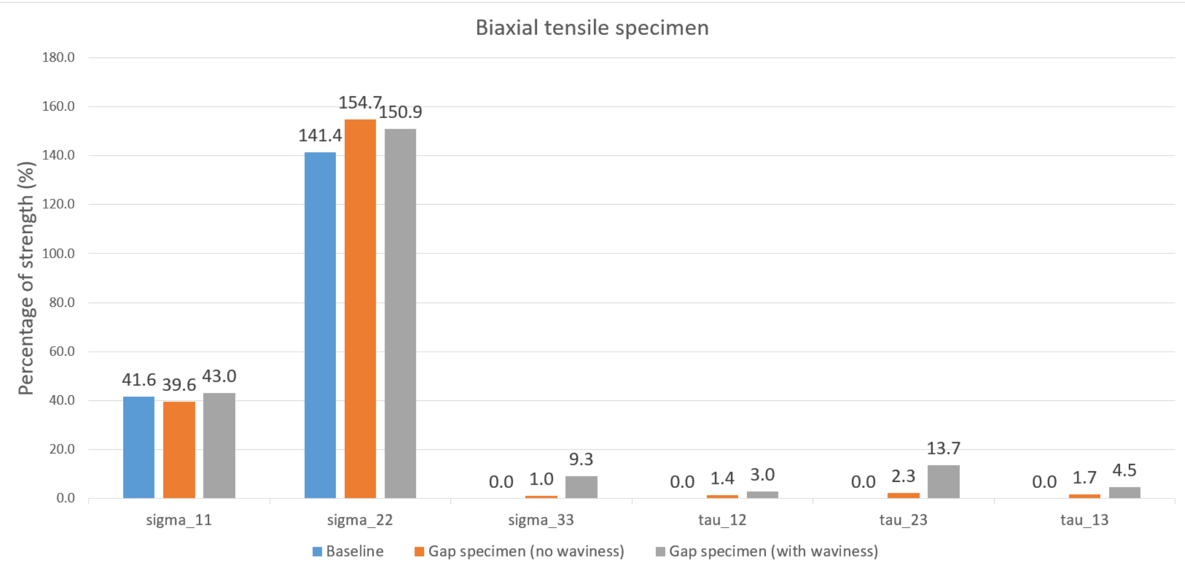

Figure 6.27: Stress components evolution (at the failure location) for the biaxial tensile specimen and comparison between baseline, and initial and updated gap specimen models (normalized with respect to strength values)

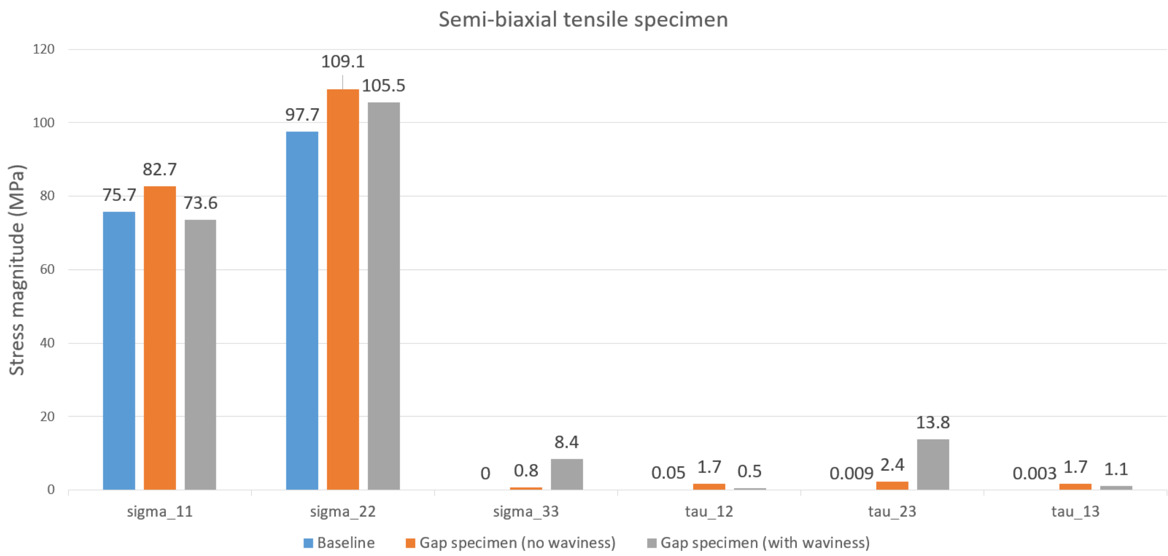

Figure 6.28: Stress components evolution (at the failure location) for the semi-biaxial tensile specimen and comparison between baseline, and initial and updated gap specimen models

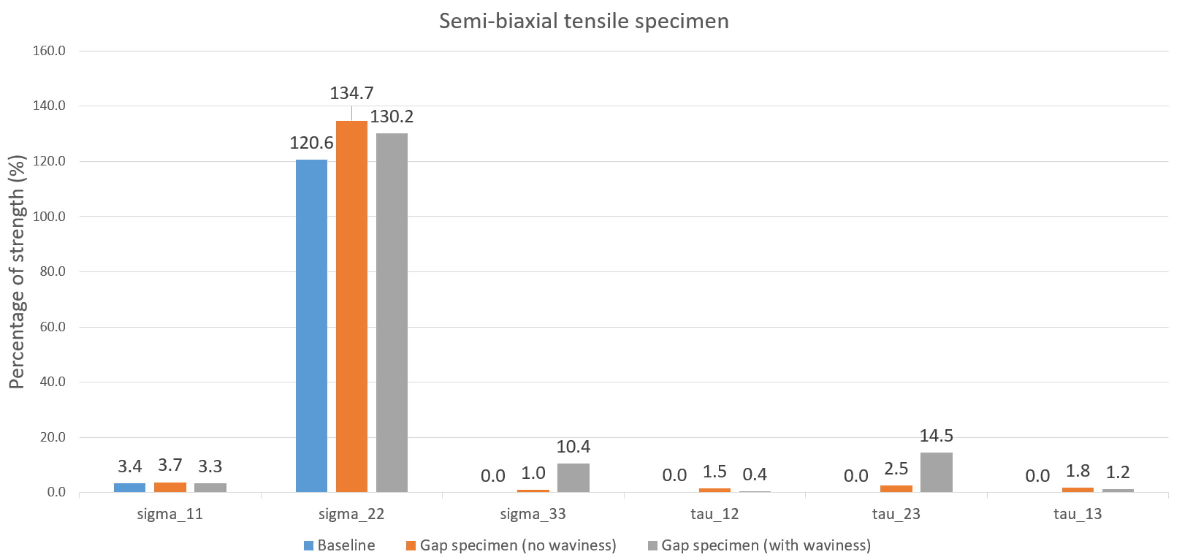

Figure 6.29: Stress components evolution (at the failure location) for the semi-biaxial tensile specimen and comparison between baseline, and initial and updated gap specimen models (normalized with respect to strength values)

7

Conclusions and Recommendations

This chapter summarizes the findings of the research, addressing the main research question, as well as the research subquestions outlined in Chapter 2. It also provides recommendations for future work to build upon the conclusions reached in this study.

7.1. Answering the research questions

7.1.1. Subquestion 1

What is a suitable specimen design, in terms of specimen geometry and layup, gap geometry and size, gap configuration, method of gap introduction, and type of loading, to accurately evaluate the effects of tow-drop gaps in the composite laminate, relevant to pressure vessel applications?

As discussed, the present research focused on designing a specimen representative of the dome area of AFP-manufactured pressure vessels which contains tow-drop gaps. This tensile specimen is eventually (possibly in a future Master's Thesis) planned to be manufactured and mechanically tested. In order to do that, the specimen to be designed has to fulfill certain requirements. The design process concluded that a cruciform-shaped specimen, subjected to biaxial tension (ideally with varying loading ratios), best represents the geometry and loading conditions of the pressure vessel's dome areas, being able to capture a large range of longitudinal-to-hoop stress ratios found in such double-curved surfaces. However, because a biaxial tensile testing machine is currently unavailable at the DASM laboratory, an alternative option was considered; using the same cruciform-shaped specimen in the uniaxial tensile testing machine, pulling the specimen in one axis, while clamping it in the other. This is the so-called ”semi-biaxial” tensile specimen, which might not achieve a pure biaxial loading, but still enables some level of loading in the perpendicular direction through the Poisson effect, making it suitable for initial assessments. Apart from these two, a third option for the specimen geometry was a classic uniaxial tensile specimen, a rectangular plate that could be more easily tested using the laboratory's existing universal testing machine.

The research aimed to compare the failure behaviour and tensile loads of baseline panels (without gaps) to panels with gaps (contained in a single ply - the gap layer) for each specimen category, addressing the main research question (see Chapter 2 and also below). In terms of the specimens' layup, it was decided that a 7-layer laminate would be the best option in order to meet all requirements set in Chapter 3. Fundamental differences in the laminate's ply orientations occurred, since the uniaxial specimen featured 0°, +40° and -40° plies, while the biaxial and semi-biaxial ones only 0 and 90° plies. The respective layups for the uniaxial and (semi)biaxial specimens containing gaps were: [0/+40/-40/GAP LAYER/-40/+40/0] and [0/90/90/GAP LAYER/90/90/0], with the gap layer always replacing a middle 0° ply, making the laminates balanced and symmetric.

An essential part of this subquestion was related to the gap geometry and size, since it was their impact that was desired to be evaluated. After literature review and a few rejected concepts, it was decided that three gaps would be introduced into the gap layer, by means of steering, realigning and dropping sets of 0° tows accordingly (see Figures 4.8 and 4.9). This would create the characteristic triangular shape found in tow-drop gaps in the literature, resembling in a large extent to the tow-drop gaps in the dome areas of pressure vessels. Regarding their size, the gaps' width was one full tow width (6.35 mm or 1/4” for the selected prepreg material) at their base, only reducing moving closer to their tip (as one can imagine based on their geometry). Their final length was nearly the maximum estimated for applications relevant to this thesis - around 72 mm.

The gaps were designed to be introduced to the laminate using the AFP method to ensure they closely represent real-world conditions. The main thesis topic after all is the impact of *AFP-induced tow-drop gaps*, thus a manual introduction of gaps would deviate from the original scope. The gap configuration, including the number and positions of gaps, was chosen arbitrarily. Three gaps were deemed sufficient to observe clear effects, as fewer gaps might not yield accurate conclusions, while more gaps would unnecessarily increase specimen size without providing significant additional insights. The gaps were spaced five full tow widths apart (approximately 32 mm) to prevent stress concentration overlap, allowing the impact of each gap to be observed separately. The same distance was kept between the gaps edges and the laminate edges, at least in the uniaxial tensile specimen, since the design for the biaxial one featured inherently a much larger distance. This would help minimize free-edge effects and focus solely on the impact of the gaps themselves.

All of the above considerations address the first research subquestion, a critical aspect of the thesis, as an appropriate specimen design is essential for accurately evaluating the impact of these manufacturing defects.

7.1.2. Subquestion 2

How does the implementation of the cured geometry of the laminate (including fiber waviness and resin-rich areas) affect the results about tensile strength, as well as the failure modes predicted initially?

The answer to this subquestion came from the analysis presented in Chapter 6. Although several assumptions and simplifications were made, it was eventually concluded that implementing a more accurate representation of the cured geometry of the laminate containing gaps - especially in the form of fiber waviness - further increases the detrimental impact of these gaps on the laminate’s tensile strength, though the extent of this effect remains uncertain. Nonetheless, this consideration brought the analysis closer to estimating the true impact of tow-drop gaps and highlighted the importance of incorporating this aspect into FE analyses of such laminates.

The failure behaviour of models with fiber waviness had minor differences from the ones without it for the (semi)biaxial specimens. These deviations concerned the specific ply that failed first and a slight shift in the failure location from above the gaps’ wider edges to above their centers. A significant difference between the two model types was observed when the failure mode of the uniaxial tensile specimen shifted from tensile fiber failure (in the simple model) to tensile matrix failure (in the updated model containing fiber waviness). This difference may be attributed to the quite small difference in estimated failure modes for this specimen, based on Failure Indexes in the Hashin criterion, making it unclear which mode would occur first. A possible solution to this issue could be to slightly reduce the orientation angle of the off-axis plies, such as changing them from ±40° to ±35° or ±30°. Keeping always in mind that reducing the off-axis ply angle closer to 0° increases the tensile failure load (which must stay well below the laboratory testing machine’s 250 kN capacity), this adjustment would provide a clearer understanding of the specimen’s actual failure mode. This observation happened a bit late in the research and design process, not allowing for a change in the specimen layup due to time constraints.

To conclude the answer to subquestion 2, incorporating fiber waviness into the models resulted in a greater estimated strength reduction compared to simpler models, although the exact extent is unclear. It also slightly influenced predictions of failure behaviour and location, showing that even a simplified approach to modelling fiber undulation can improve analysis accuracy.

7.1.3. Main research question

How do gaps resulting from tow drops during the Automated Fiber Placement (AFP) process, and which are isolated from free-edge effects affect the tensile strength (in terms of First-Ply Failure) of a composite laminate?

In conclusion, the main research question of this thesis can be addressed: the gap specimens discussed in the previous chapters generally showed a reduction in tensile strength compared to baseline panels without gaps. The extent of this reduction is up for debate; simple FE models, not accounting for the actual geometry of the laminate after curing exhibited reductions of 21.6%, 16% and 18.8% for the uniaxial, biaxial and semi-biaxial tensile specimens respectively. However, the updated models of the same specimens, which implemented the cured geometry of the laminates in the form of fiber waviness (even if it was at just a basic level), estimated higher tensile strength knockdowns, at 55%, 21.4% and 27.9%. The out-of-plane stresses, σ_{33}, τ_{23}, and τ_{13}, were identified as the primary contributors to the observed increases. Although initially negligible, these stresses significantly increased after incorporating fiber waviness. This outcome aligns with the nature of fiber waviness (the out-of-plane motion of plies), which induces out-of-plane stress concentrations.

The strength knockdown increases for the (semi-)biaxial cases align with the findings of Falcó et al. (2017) [31], who observed a similar trend in their FE models and experimental results for laminates with tow-drop gaps. Their omission of fiber waviness in simulations likely caused a 10% deviation from experimental data, supporting the validity of the updated biaxial models in this thesis. However, for the uniaxial tensile specimen, the updated model in the present thesis predicts a 55% strength reduction compared to 21.6% from the simpler model, an unreasonably large deviation likely caused by modelling errors or excessive simplifications. A more realistic strength knockdown for the uniaxial case is estimated between 22% and 32%, making a revision of the FE model for accurate predictions necessary.

7.2. Recommendations for future work

Several recommendations can be given for the future, in order to build upon the findings of this thesis and produce more concrete answers regarding the impact of AFP-induced manufacturing defects.

First, it is recommended to manufacture the discussed specimens of this thesis and perform the relevant tensile tests. The priority in manufacturing and testing should focus on the biaxial specimen if the appropriate biaxial testing machine becomes available. However, if this is not the case, the semi-biaxial tensile specimens should be manufactured and tested on the already available equipment. If this is not feasible either, the uniaxial tensile specimen should still be a good alternative. The experimental testing of the specimens will provide critical data on tensile strength and failure behaviour.

Additionally, another set of specimens, separate from those used for tensile tests, should be manufactured. These specimens would be smaller than the previous, essentially only including the gauge area (where the gaps are located) and would be intended for sectioning and optical microscopy. This analysis will estimate the level of fiber waviness in and around gap areas, offering detailed insights into local geometric distortions. Based on these observations, the FE models should be updated for a more realistic representation of fiber waviness. Apart from geometric modifications, the FE models could also be expanded to account for progressive damage analysis, since so far they only estimate the tensile strength of the laminates on a First Ply Failure basis. Comparing the results of these enhanced models with experimental data will help improve the accuracy of predictions related to the impact of the tow-drop gaps on the tensile strength of the laminates.

Moreover, once a high-fidelity FE model incorporating tow-drop gaps is achieved, expanding the scope to include tow-drop overlaps becomes essential. This could involve adding overlaps to a laminate already containing gaps to predict the combined effect of these defects or exclusively focusing on overlaps by replacing all gaps with overlaps and modifying the geometry of the laminate accordingly. The latter approach appears more promising, given the significant uncertainty in the current literature regarding the impact of overlaps. Such studies would provide a clearer understanding of how overlaps influence structural performance.

It was discussed in Chapter 1 that this thesis was carried out in collaboration with Airborne Aerospace, therefore the company's more practical interests should be addressed as well. Since a CFRP pressure vessel was already manufactured by Airborne (at the stage of a demonstrator), it is reasonable that a validation of the models presented in this thesis using the actual manufactured vessel could be achieved. This could be done via physical testing of the demonstrator, with pressure and burst tests providing valuable insights about the vessel's behaviour and ultimate failure strength. Note that a burst test is essentially a pressure test until catastrophic failure of the structure.

Before conducting the relevant mechanical testing, non-destructive testing (NDT) techniques such as Ultrasonic Testing (UT) or X-Ray Computer Tomography (CT) could be used to evaluate the actual percentage of gap in the dome areas of the pressure vessel, as well as the cured geometry of the structure. This information could then be used to refine the FE models presented in this research, or create new, more detailed models. Parametric models could also be generated, allowing for the systematic evaluation of how variations in gap size, distribution, and geometry, but also variations in the vessel's layup could influence the structural performance. Ultimately, the above proposals could lead to the development of standardized guidelines and best practices for designing and manufacturing AFP-produced pressure vessels, while taking into account the presence of AFP-induced manufacturing defects.

Lastly, an additional interesting research possibility stems from the positive impact of polyetherimide (PEI) on the fracture toughness of thermoset based composite structures, as demonstrated by the study of Farooq et al. (2023) [72]. Polyetherimide is an advanced high performance thermoplastic that possesses exceptional thermal and chemical properties, along with high tensile strength [73]. It is available in various forms, especially as a film [74], as a powder [75], and even as a 3D printed part [76]. It can be assumed that if inserted in a composite laminate that contains gaps, PEI can dissolve into the resin that fills the gaps and increase the overall fracture toughness of the laminate, mitigating in this way the negative effects of gaps (Figure 7.1). This is a hypothesis worth investigating, probably in a future thesis. In this scope, three sets of samples could be manufactured and mechanically tested; one without defects, one containing tow-drop gaps (as the ones suggested in this thesis) and a third one containing tow-drop gaps and including PEI. If the hypothesis proves correct, it could lead to the development of a standardized method for mitigating the impact of gaps, providing significant value to the industry, including Airborne.

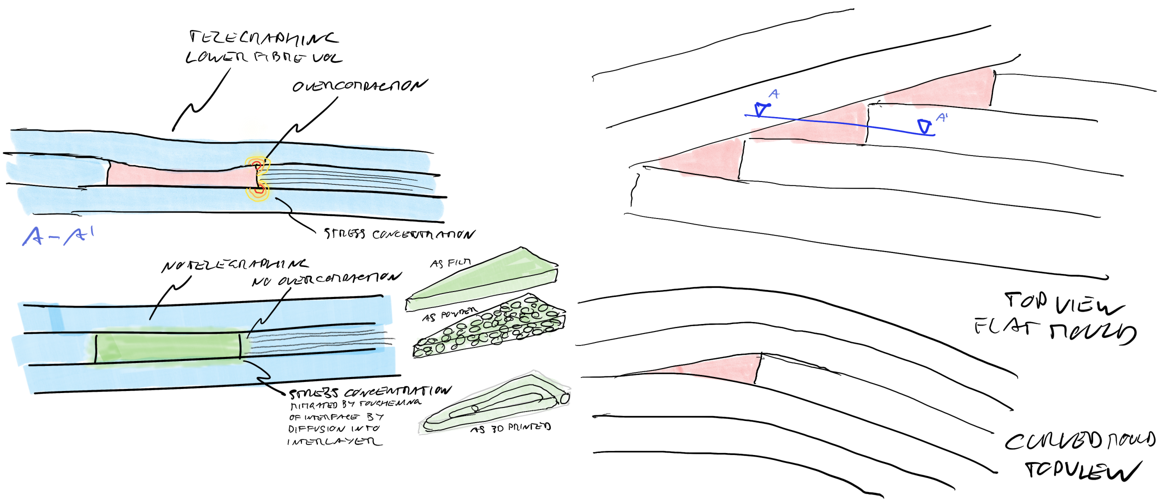

Figure 7.1: Schematic representation of PEI effect on tow-drop gaps [77]

References

[1] Natasha Ramli et al. "Advanced Polymer Composite for Aerospace Engineering Applications". In: *Advanced Composites in Aerospace Engineering Applications*. Ed. by Norkhairunnisa Mazlan, S.M. Sapuan, and R.A. Ilyas. Cham: Springer International Publishing, 2022, pp. 1–21. ISBN: 978-3-030-88191-7 978-3-030-88192-4. DOI: 10.1007/978-3-030-88192-4_1. URL: https://link.springer.com/10.1007/978-3-030-88192-4_1 (visited on 06/10/2024).

[2] Rachid Hsissou et al. "Polymer composite materials: A comprehensive review". In: *Composite Structures* 262 (Apr. 2021), p. 113640. ISSN: 02638223. DOI: 10.1016/j.compstruct.2021.113640. URL: https://linkinghub.elsevier.com/retrieve/pii/S026382232100101X (visited on 06/10/2024).

[3] P.K. Mallick. *Fiber-Reinforced Composites: Materials, Manufacturing, and Design, Third Edition*. 0th ed. CRC Press, Nov. 19, 2007. ISBN: 978-0-429-12206-4. DOI: 10.1201/9781420005981. URL: https://www.taylorfrancis.com/books/9781420005981 (visited on 06/10/2024).

[4] Robert S. Pierce and Brian G. Falzon. "Simulating Resin Infusion through Textile Reinforcement Materials for the Manufacture of Complex Composite Structures". In: *Engineering* 3.5 (Oct. 2017), pp. 596–607. ISSN: 20958099. DOI: 10.1016/J.ENG.2017.04.006. URL: https://linkinghub.elsevier.com/retrieve/pii/S2095809917307117 (visited on 06/11/2024).

[5] Jens Bachmann, Carme Hidalgo, and Stéphanie Bricout. "Environmental analysis of innovative sustainable composites with potential use in aviation sector—A life cycle assessment review". In: *Science China Technological Sciences* 60.9 (Sept. 2017), pp. 1301–1317. ISSN: 1674-7321, 1869-1900. DOI: 10.1007/s11431-016-9094-y. URL: http://link.springer.com/10.1007/s11431-016-9094-y (visited on 06/11/2024).

[6] Ebrahim Oromiehie et al. "Automated fibre placement based composite structures: Review on the defects, impacts and inspections techniques". In: *Composite Structures* 224 (Sept. 2019), p. 110987. ISSN: 02638223. DOI: 10.1016/j.compstruct.2019.110987. URL: https://linkinghub.elsevier.com/retrieve/pii/S0263822319308281 (visited on 05/07/2024).

[7] August T. Noevere and Craig Collier. "Design for Manufacturing Tool for Automated Fiber Placement Structures – Verification and Validation". In: *AIAA Scitech 2020 Forum*. AIAA Scitech 2020 Forum. Orlando, FL: American Institute of Aeronautics and Astronautics, Jan. 6, 2020. ISBN: 978-1-62410-595-1. DOI: 10.2514/6.2020-1477. URL: https://arc.aiaa.org/doi/10.2514/6.2020-1477 (visited on 06/13/2024).

[8] Alex Brasington et al. "Automated fiber placement: A review of history, current technologies, and future paths forward". In: *Composites Part C: Open Access* 6 (Oct. 2021), p. 100182. ISSN: 26666820. DOI: 10.1016/j.jcomc.2021.100182. URL: https://linkinghub.elsevier.com/retrieve/pii/S2666682021000773 (visited on 06/12/2024).

[9] Dirk H.-J.A. Lukaszewicz, Carwyn Ward, and Kevin D. Potter. "The engineering aspects of automated prepreg layup: History, present and future". In: *Composites Part B: Engineering* 43.3 (Apr. 2012), pp. 997–1009. ISSN: 13598368. DOI: 10.1016/j.compositesb.2011.12.003. URL: https://linkinghub.elsevier.com/retrieve/pii/S1359836811005452 (visited on 05/07/2024).

[10] Falk Heinecke and Christian Willberg. "Manufacturing-Induced Imperfections in Composite Parts Manufactured via Automated Fiber Placement". In: *Journal of Composites Science* 3.2 (June 2, 2019), p. 56. ISSN: 2504-477X. DOI: 10.3390/jcs3020056. URL: https://www.mdpi.com/2504-477X/3/2/56 (visited on 05/09/2024).

[11] Mohammad Bahar and Michael Sinapius. "Adaptive Feeding Roller with An Integrated Cutting System for Automated Fiber Placement (AFP)". In: *Journal of Composites Science* 4.3 (July 16, 2020), p. 92. ISSN: 2504-477X. DOI: 10.3390/jcs4030092. URL: https://www.mdpi.com/2504-477X/4/3/92 (visited on 06/12/2024).

[12] Pierre Debout, Hélène Chanal, and Emmanuel Duc. "Tool path smoothing of a redundant machine: Application to Automated Fiber Placement". In: *Computer-Aided Design* 43.2 (Feb. 2011), pp. 122–132. ISSN: 00104485. DOI: 10.1016/j.cad.2010.09.011. URL: https://linkinghub.elsevier.com/retrieve/pii/S0010448510001788 (visited on 06/12/2024).

[13] Duy Cao. *What is Automated Fiber Placement (AFP) in Composites Manufacturing?* Wevolver. June 27, 2022. URL: https://www.wevolver.com/article/what-is-automated-fiber-placement-afp-in-composites-manufacturing (visited on 06/12/2024).

[14] Timothy R. Brooks and Joaquim R.R.A. Martins. "On manufacturing constraints for tow-steered composite design optimization". In: *Composite Structures* 204 (Nov. 2018), pp. 548–559. ISSN: 02638223. DOI: 10.1016/j.compstruct.2018.07.100. URL: https://linkinghub.elsevier.com/retrieve/pii/S0263822318308158 (visited on 05/07/2024).

[15] Guillaume Rousseau et al. "Automated Fiber Placement Path Planning: A state-of-the-art review". In: *Computer-Aided Design and Applications* 16.2 (Aug. 13, 2018), pp. 172–203. ISSN: 16864360. DOI: 10.14733/cadaps.2019.172-203. URL: http://cad-journal.net/files/vol_16/Vol16No2.html (visited on 06/12/2024).

[16] Xiangqian Li, Stephen R. Hallett, and Michael R. Wisnom. "Modelling the effect of gaps and overlaps in automated fibre placement (AFP)-manufactured laminates". In: *Science and Engineering of Composite Materials* 22.2 (Mar. 1, 2015), pp. 115–129. ISSN: 2191-0359, 0792-1233. DOI: 10.1515/secm-2013-0322. URL: https://www.degruyter.com/document/doi/10.1515/secm-2013-0322/html (visited on 05/06/2024).

[17] Ramy Harik et al. "Automated fiber placement defect identity cards: cause, anticipation, existence, significance, and progression". In: SAMPE 18 - Long Beach. Long Beach, CA, Jan. 2018.

[18] Zafer Gurdal, Brian Tatting, and K. Wu. "Tow-Placement Technology and Fabrication Issues for Laminated Composite Structures". In: *46th AIAA/ASME/ASCE/AHS/ASC Structures, Structural Dynamics and Materials Conference*. 46th AIAA/ASME/ASCE/AHS/ASC Structures, Structural Dynamics and Materials Conference. Austin, Texas: American Institute of Aeronautics and Astronautics, Apr. 18, 2005. ISBN: 978-1-62410-065-9. DOI: 10.2514/6.2005-2017. URL: https://arc.aiaa.org/doi/10.2514/6.2005-2017 (visited on 05/15/2024).

[19] Patrick Langley. "Finite Element Modeling of Tow-Placed Variable-Stiffness Composite Laminates". Master's Thesis. Virginia Polytechnic Institute and State University, 1999.

[20] Shouzheng Sun et al. "Defect Characteristics and Online Detection Techniques During Manufacturing of FRPs Using Automated Fiber Placement: A Review". In: *Polymers* 12.6 (June 12, 2020), p. 1337. ISSN: 2073-4360. DOI: 10.3390/polym12061337. URL: https://www.mdpi.com/2073-4360/12/6/1337 (visited on 05/09/2024).

[21] Christos Kassapoglou. *Design and analysis of composite structures: with applications to aerospace structures*. eng. Second ed. Aerospace series. West Sussex, United Kingdom: John Wiley & Sons Inc, 2013. ISBN: 978-1-118-40160-6 978-1-118-53694-0.

[22] Jiefei Gu and Puhui Chen. "Some modifications of Hashin's failure criteria for unidirectional composite materials". In: *Composite Structures* 182 (2017), pp. 143–152. ISSN: 0263-8223. DOI: https://doi.org/10.1016/j.compstruct.2017.09.011. URL: https://www.sciencedirect.com/science/article/pii/S0263822317317543.

[23] A. Riccio et al. "Modelling the damage evolution in notched omega stiffened composite panels under compression". In: *Composites Part B: Engineering* 126 (2017), pp. 60–71. ISSN: 1359-8368. DOI: https://doi.org/10.1016/j.compositesb.2017.05.067. URL: https://www.sciencedirect.com/science/article/pii/S1359836817302822.

[24] Kaven Croft et al. "Experimental study of the effect of automated fiber placement induced defects on performance of composite laminates". In: *Composites Part A: Applied Science and Manufacturing* 42.5 (May 2011), pp. 484–491. ISSN: 1359835X. DOI: 10.1016/j.compositesa.2011.01.007. URL: https://linkinghub.elsevier.com/retrieve/pii/S1359835X11000224 (visited on 05/07/2024).

[25] O. Falcó et al. "Variable-stiffness composite panels: Defect tolerance under in-plane tensile loading". In: *Composites Part A: Applied Science and Manufacturing* 63 (Aug. 2014), pp. 21–31. ISSN: 1359835X. DOI: 10.1016/j.compositesa.2014.03.022. URL: https://linkinghub.elsevier.com/retrieve/pii/S1359835X14001018 (visited on 05/15/2024).

[26] Michael R. Wisnom. "7.4 Size Effects in Composites□". In: *Comprehensive Composite Materials II*. Ed. by Peter W.R. Beaumont and Carl H. Zweben. Oxford: Elsevier, 2018, pp. 56–78. ISBN: 978-0-08-100534-7. DOI: https://doi.org/10.1016/B978-0-12-803581-8.03918-7. URL: https://www.sciencedirect.com/science/article/pii/B9780128035818039187.

[27] Minh Hoang Nguyen et al. "Effect of automated fiber placement (AFP) manufacturing signature on mechanical performance of composite structures". In: *Composite Structures* 228 (Nov. 2019), p. 111335. ISSN: 02638223. DOI: 10.1016/j.compstruct.2019.111335. URL: https://linkinghub.elsevier.com/retrieve/pii/S0263822319317672 (visited on 05/06/2024).

[28] Adriana W. Blom et al. "A Theoretical Model to Study the Influence of Tow-drop Areas on the Stiffness and Strength of Variable-stiffness Laminates". In: *Journal of Composite Materials* 43.5 (Mar. 2009), pp. 403–425. ISSN: 0021-9983, 1530-793X. DOI: 10.1177/0021998308097675. URL: http://journals.sagepub.com/doi/10.1177/0021998308097675 (visited on 05/07/2024).

[29] Carlos G. Davila, Pedro P. Camanho, and Cheryl A. Rose. "Failure Criteria for FRP Laminates". In: *Journal of Composite Materials* 39.4 (2005), pp. 323–345. DOI: 10.1177/0021998305046452. eprint: https://doi.org/10.1177/0021998305046452. URL: https://doi.org/10.1177/0021998305046452.

[30] Silvestre Pinho et al. "Failure Models and Criteria for FRP Under In-Plane or Three-Dimensional Stress States Including Shear Non-Linearity". In: (Mar. 2005).

[31] O. Falcó et al. "Modelling and simulation of tow-drop effects arising from the manufacturing of steered-fibre composites". In: *Composites Part A: Applied Science and Manufacturing* 93 (Feb. 2017), pp. 59–71. ISSN: 1359835X. DOI: 10.1016/j.compositesa.2016.11.015. URL: https://linkinghub.elsevier.com/retrieve/pii/S1359835X16303967 (visited on 05/07/2024).

[32] Wilhelm Woigk et al. "Experimental investigation of the effect of defects in Automated Fibre Placement produced composite laminates". In: *Composite Structures* 201 (Oct. 2018), pp. 1004–1017. ISSN: 02638223. DOI: 10.1016/j.compstruct.2018.06.078. URL: https://linkinghub.elsevier.com/retrieve/pii/S0263822317339946 (visited on 05/09/2024).

[33] Minh Hoang Nguyen, Paul Davidson, and Anthony M. Waas. "Experimental and numerical study on the tensile failure behavior of toughened-interlayer composite laminates with automated fiber placement (AFP) induced gap and overlap defects". In: *International Journal of Material Forming* 14.1 (Jan. 2021), pp. 105–119. ISSN: 1960-6206, 1960-6214. DOI: 10.1007/s12289-020-01581-w. URL: https://link.springer.com/10.1007/s12289-020-01581-w (visited on 05/07/2024).

[34] Roland Lichtinger et al. "Simulation and experimental validation of gaps and bridging in the automated fiber placement process". In: *Science and Engineering of Composite Materials* 22.2 (Mar. 1, 2015), pp. 131–148. ISSN: 2191-0359, 0792-1233. DOI: 10.1515/secm-2013-0158. URL: https://www.degruyter.com/document/doi/10.1515/secm-2013-0158/html (visited on 05/09/2024).

[35] Kazem Fayazbakhsh et al. "Defect layer method to capture effect of gaps and overlaps in variable stiffness laminates made by Automated Fiber Placement". In: *Composite Structures* 97 (Mar. 2013), pp. 245–251. ISSN: 02638223. DOI: 10.1016/j.compstruct.2012.10.031. URL: https://linkinghub.elsevier.com/retrieve/pii/S0263822312005272 (visited on 05/07/2024).

[36] Vibhas Mishra, Daniël M.J. Peeters, and Mostafa M. Abdalla. "Stiffness and buckling analysis of variable stiffness laminates including the effect of automated fibre placement defects". In: *Composite Structures* 226 (Oct. 2019), p. 111233. ISSN: 02638223. DOI: 10.1016/j.compstruct.2019.111233. URL: https://linkinghub.elsevier.com/retrieve/pii/S0263822318345677 (visited on 05/07/2024).

[37] Mahdi Arian Nik et al. "Optimization of variable stiffness composites with embedded defects induced by Automated Fiber Placement". In: *Composite Structures* 107 (Jan. 2014), pp. 160–166. ISSN: 02638223. DOI: 10.1016/j.compstruct.2013.07.059. URL: https://linkinghub.elsevier.com/retrieve/pii/S0263822313003978 (visited on 05/07/2024).

[38] A. Marouene et al. “Effects of gaps and overlaps on the buckling behavior of an optimally designed variable-stiffness composite laminates – A numerical and experimental study”. In: *Composite Structures* 140 (Apr. 2016), pp. 556–566. ISSN: 02638223. DOI: 10.1016/j.compstruct.2016.01.012. URL: https://linkinghub.elsevier.com/retrieve/pii/S0263822316000258 (visited on 05/06/2024).

[39] László Czél. “Enhanced characterization of tow gaps in fiber steered laminates: Advanced specimen design for better representation of defects in structures”. PhD thesis. TU Delft, 2024.

[40] Navid Niknafs Kermani et al. “Gap filling mechanisms during the thin ply Automated Tape Placement process”. In: *Composites Part A: Applied Science and Manufacturing* 147 (Aug. 2021), p. 106454. ISSN: 1359835X. DOI: 10.1016/j.compositesa.2021.106454. URL: https://linkinghub.elsevier.com/retrieve/pii/S1359835X21001767 (visited on 05/20/2024).

[41] D.A. Mccarville. “Intellectual property, patents and innovation in aeronautics”. In: *Innovation in Aeronautics*. Elsevier, 2012, pp. 263–304. ISBN: 978-1-84569-550-7. DOI: 10.1533/9780857096098.3.263. URL: https://linkinghub.elsevier.com/retrieve/pii/B9781845695507500136 (visited on 06/14/2024).

[42] Pavel Simacek et al. “Role of resin percolation in gap filling mechanisms during the thin ply thermosetting automated tape placement process”. In: *Composites Part A: Applied Science and Manufacturing* 152 (Jan. 2022), p. 106677. ISSN: 1359835X. DOI: 10.1016/j.compositesa.2021.106677. URL: https://linkinghub.elsevier.com/retrieve/pii/S1359835X21003948 (visited on 05/20/2024).

[43] H. Zhu et al. “A Progressive FE Failure Model for Laminates under Biaxial Loading”. en. In: *Mechanics of Composite Materials* 56.2 (May 2020), pp. 207–214. ISSN: 0191-5665, 1573-8922. DOI: 10.1007/s11029-020-09873-7. URL: https://link.springer.com/10.1007/s11029-020-09873-7 (visited on 01/15/2025).

[44] M. J. Hinton, P. D. Soden, and A. S. Kaddour. “Strength of composite laminates under biaxial loads”. en. In: *Applied Composite Materials* 3.3 (1996), pp. 151–162. ISSN: 0929-189X, 1573-4897. DOI: 10.1007/BF00135053. URL: http://link.springer.com/10.1007/BF00135053 (visited on 01/15/2025).

[45] J.S. Welsh, J.S. Mayes, and Adam Biskner. “Experimental and numerical failure predictions of biaxially-loaded quasi-isotropic carbon composites”. In: *ICCM International Conferences on Composite Materials* (Jan. 2007).

[46] Ebrahim Oromiehie et al. “Automated manufacture and experimentation of composite overwrapped pressure vessel with embedded optical sensor”. en. In: *International Journal of Hydrogen Energy* 79 (Aug. 2024), pp. 1215–1226. ISSN: 03603199. DOI: 10.1016/j.ijhydene.2024.06.364. URL: https://linkinghub.elsevier.com/retrieve/pii/S036031992402603X (visited on 10/22/2024).

[47] Dennis R. Moss and Michael Basic. “1 - General Topics”. In: *Pressure Vessel Design Manual (Fourth Edition)*. Ed. by Dennis R. Moss and Michael Basic. Fourth Edition. Oxford: Butterworth-Heinemann, 2013, pp. 1–36. ISBN: 978-0-12-387000-1. DOI: https://doi.org/10.1016/B978-0-12-387000-1.00001-2. URL: https://www.sciencedirect.com/science/article/pii/B9780123870001000012.

[48] Kristaq Hazizi and Mohammad Ghaleeh. “Design and Analysis of a Typical Vertical Pressure Vessel Using ASME Code and FEA Technique”. In: *Designs* 7.3 (2023). ISSN: 2411-9660. DOI: 10.3390/designs7030078. URL: https://www.mdpi.com/2411-9660/7/3/78.

[49] Sotiris Koussios. “Design of cylindrical composite pressure vessels: Integral optimisation”. In: *ICCM International Conferences on Composite Materials* (Jan. 2009).

[50] Kumar Mukesh. “Stress Analysis of Pressure Vessels”. In: *International Journal of Advance Research and Innovative Ideas in Education* 3.3 (2017). ISSN: 2395-4396.

[51] Junxian Chen, Jianhai Zhang, and Hongwei Zhao. “Designing a Cruciform Specimen via Topology and Shape Optimisations under Equal Biaxial Tension Using Elastic Simulations”. In: *Materials* 15.14 (2022). ISSN: 1996-1944. DOI: 10.3390/ma15145001. URL: https://www.mdpi.com/1996-1944/15/14/5001.

[52] International Organization for Standardization. "Determination of tensile properties - Part 5: Test conditions for unidirectional fibre-reinforced plastic composites". In: *ISO 527-5:1997* (1997). URL: https://www.iso.org/standard/80370.html.

[53] Laurence W. McKeen. "Chapter 1 - Introduction to Plastics and Elastomers". In: *The Effect of Creep and Other Time Related Factors on Plastics and Elastomers (Second Edition)*. Ed. by Laurence W. McKeen. Second Edition. Plastics Design Library. Boston: William Andrew Publishing, 2009, pp. 1–31. ISBN: 978-0-8155-1585-2. DOI: https://doi.org/10.1016/B978-0-8155-1585-2.50003-0. URL: https://www.sciencedirect.com/science/article/pii/B9780815515852500030.

[54] STEPLAB. *PLANAR BIAXIAL CRUCIFORM SYSTEMS*. URL: https://step-lab.com/multi-actuator-systems/planar-cruciform-biaxial-systems/.

[55] Hexcel. "HexPly® 8552 Epoxy matrix (180°C/356°F curing matrix) Product Datasheet". In: *HexPly® 8552 Epoxy matrix (180°C/356°F curing matrix) Product Datasheet* (2024).

[56] Laminated Plastics. "Technical Data Sheet FR-4". In: ().

[57] Hwai-Chung Wu and Christopher D. Eamon. "3 - Composite mechanics". In: *Strengthening of Concrete Structures using Fiber Reinforced Polymers (FRP)*. Ed. by Hwai-Chung Wu and Christopher D. Eamon. Woodhead Publishing, 2017, pp. 19–34. ISBN: 978-0-08-100636-8. DOI: https://doi.org/10.1016/B978-0-08-100636-8.00003-X. URL: https://www.sciencedirect.com/science/article/pii/B978008100636800003X.

[58] M. Acin. *Stress singularities, stress concentrations and mesh convergence*. Feb. 2015. URL: http://www.acin.net/2015/06/02/stress-singularities-stress-concentrations-and-mesh-convergence/.

[59] Melanie Herman et al. "Evaluation of advanced approaches based on Continuum Damage Mechanics for composite failure analysis: status and way forward". In: (Nov. 2022).

[60] Renato S.M. Almeida et al. "Identifying damage mechanisms of composites by acoustic emission and supervised machine learning". In: *Materials & Design* 227 (2023), p. 111745. ISSN: 0264-1275. DOI: https://doi.org/10.1016/j.matdes.2023.111745. URL: https://www.sciencedirect.com/science/article/pii/S0264127523001600.

[61] *Acoustic Emission Testing: A COMPLETE Guide*. URL: https://www.aendt.com/blog/acoustic-emission-testing.html.

[62] Michael Scheerer et al. "Damage Detection and Identification in Composites by Acoustic Emission, Ultrasonic Inspection and Computer Tomography". In: Jan. 2023, pp. 883–891. ISBN: 978-3-031-07321-2. DOI: 10.1007/978-3-031-07322-9_89.

[63] Markus Sause. "Identification of failure mechanisms in fiber reinforced composites by acoustic emission analysis". In: June 2013. ISBN: 978-1-138-00086-5. DOI: 10.1201/b16387-52.

[64] Michal Šofer et al. "Damage Analysis of Composite CFRP Tubes Using Acoustic Emission Monitoring and Pattern Recognition Approach". In: *Materials* 14.4 (2021). ISSN: 1996-1944. DOI: 10.3390/ma14040786. URL: https://www.mdpi.com/1996-1944/14/4/786.

[65] *Acoustic Emission Testing: Reliable Structural Defect Detection*. URL: https://www.acuren.com/inspection/advanced-nde-ndt/acoustic-emission-testing/.

[66] Walter Nsengiyumva et al. "Advances, limitations and prospects of nondestructive testing and evaluation of thick composites and sandwich structures: A state-of-the-art review". In: *Composite Structures* 256 (2021), p. 112951. ISSN: 0263-8223. DOI: https://doi.org/10.1016/j.compstruct.2020.112951. URL: https://www.sciencedirect.com/science/article/pii/S0263822320328774.

[67] Senseven Marketing Team. *Senseven Blog*. July 2023. URL: https://blog.senseven.ai/understanding-active-ultrasound-vs.-acoustic-emission-exploring-nondestructive-testing-methods.

[68] Kyungil Kong et al. "Progress and Trends in Damage Detection Methods, Maintenance, and Data-driven Monitoring of Wind Turbine Blades – A Review". In: *Renewable Energy Focus* 44 (2023), pp. 390–412. ISSN: 1755-0084. DOI: https://doi.org/10.1016/j.ref.2022.08.005. URL: https://www.sciencedirect.com/science/article/pii/S1755008422000606.

[69] Bing Pan. “Digital image correlation for surface deformation measurement: historical developments, recent advances and future goals”. In: *Measurement Science and Technology* 29.8 (June 2018), p. 082001. DOI: 10.1088/1361-6501/aac55b. URL: https://dx.doi.org/10.1088/1361-6501/aac55b.

[70] John Holmes et al. “Digital image and volume correlation for deformation and damage characterisation of fibre-reinforced composites: A review”. In: *Composite Structures* 315 (2023), p. 116994. ISSN: 0263-8223. DOI: https://doi.org/10.1016/j.compstruct.2023.116994. URL: https://www.sciencedirect.com/science/article/pii/S0263822323003380.

[71] *A practical guide to DIC.* URL: https://digitalimagecorrelation.org/.

[72] Ujala Farooq et al. “Synergistic Toughening of Epoxy through Layered Poly(ether imide) with Dual-Scale Morphologies”. In: *ACS Applied Materials & Interfaces* (Nov. 2, 2023), acsami.3c10096. ISSN: 1944-8244, 1944-8252. DOI: 10.1021/acsami.3c10096. URL: https://pubs.acs.org/doi/10.1021/acsami.3c10096 (visited on 06/15/2024).

[73] Soo-Jin Park and Min-Kang Seo. “Element and Processing”. In: *Interface Science and Technology*. Vol. 18. Elsevier, 2011, pp. 431–499. ISBN: 978-0-12-375049-5. DOI: 10.1016/B978-0-12-375049-5.00006-2. URL: https://linkinghub.elsevier.com/retrieve/pii/B9780123750495000062 (visited on 06/15/2024).

[74] *Polyetherimide film - 7 reasons to use it*. URL: https://www.mueller-ahlhorn.com/en/polyetherimide-film-7-reasons-for-use/.

[75] Inc. PolyClean Technologies. *Polyetherimide Powder*. URL: https://www.polycleantech.com/polyetherimide-powder/.

[76] Aysha M. *All You Need to Know About ULTEM/PEI for 3D Printing*. July 12, 2023. URL: https://www.3dnatives.com/en/ultem-030820204/#!.

[77] Clemens Dransfeld. *Schematic Representation of PEI effect on tow-drop gaps*.